

ulm university universität
uulm

Growth and Characterization of Diamond δ-Doped Layers for FET Applications

Dissertation

zur Erlangung des akademischen Grades eines

Doktor-Ingenieurs
(Dr.-Ing.)

der Fakultät für Ingenieurwissenschaften
und Informatik der Universität Ulm

von

M.Sc. HAYSSAM EL-HAJJ
AUS SAIDA

Gutachter: Prof. Dr.-Ing. E. Kohn
Prof. Dr. P. Unger

Amtierender Dekan: Prof. Dr.-Ing. Michael Weber

Ulm, 31. März 2009

Contents

Contents i

List of Figures v

List of Tables xi

1 Summary 1

2 Introduction 5

3 Properties of Diamond 9

3.1 Crystal structure 9

3.2 Band Structure 10

3.3 Electrical Properties of Diamond 11

3.4 Diamond as a Semiconductor 11

4 Concepts and Principles of Diamond Growth 15

4.1 High Temperature High Pressure Growth (HTHP) 16

4.2 Chemical Vapor Deposition (CVD) 16

4.2.1 Hot Filament CVD (HFCVD) 18

4.2.2 Microwave Plasma CVD (MWPCVD) 19

4.3 Principles of diamond CVD growth 19

4.4 Substrates 22

4.4.1 Single crystalline CVD diamond on HTHP stones 22

5 Bulk Doping of Diamond **25**

5.1 N-Type Doping 27

5.1.1 Nitrogen 27

5.1.2 Phosphorous 29

5.2 P-Type Diamond 30

5.2.1 Hydrogen terminated diamond surface 30

5.2.2 Bulk Doping with Boron 31

6 Diamond δ -Doping **33**

6.1 Electrochemical profiling of boron-delta-doped layers 35

6.2 Requirements and conditions 38

6.3 Growth Procedure 39

6.4 Conclusion on growth 42

7 Characterization of Boron δ-Doped Layers for Electronics **43**

7.1 Photoluminescence 43

7.2 Sheet Resistance 44

7.3 Capacitance Voltage Measurement 45

7.4 Scanning Tunneling Microscopy (STM) 47

7.5 Buffer layer preparation and characterization: Atomic Force Microscopy . . 48

7.6 Secondary Ion Mass Spectrometry (SIMS) 52

7.7 Elastic Recoil Detection (ERD) 53

8 FET concepts based on Boron δ-Doping **57**

8.1 MESFET Characteristics and Structure 57

8.2 P-I-P FET 59

8.3 MESFET and MOSFET Structures applied to Diamond 61

8.4 δ Channel FET 62

8.5 Ion Sensitive FET on Diamond 64

9 Technology and Fabrication Process **69**

9.1 Technological Steps 69

9.1.1 Ohmic contact Technology 70

9.1.2 Gate contact technology 73

9.1.3 Gate recess 73

9.1.4 Mesa etching 74

9.1.5 Recess etching and overgrowth 74

9.2 Single delta MISFET 75

9.3 Double delta layer transistors 79

9.4 Double delta FETs with dielectric layer prior to metalization 80

9.5 ISFET on Single crystal Diamond 82

10 Results **85**

10.1 Double delta transistors 85

10.2 Single delta MISFET 86

10.3 Single Crystal ISFET results 94

10.4 P-I-P Transistor Results 97

11 Conclusion and outlook **101**

A ISFET on NCD using Delta Doping **103**

A.1 Nano Crystalline HFCVD diamond films on 4 inch Silicon wafers 103

A.2 $ISFET$ on Nanocrystalline Diamond 105

A.2.1 Delta doped Nanodiamond 105

A.2.2 Nanodiamond ISFET fabrication 106

A.3 Nano Crystalline ISFET Results 108

A.4 Conclusion for the ISFET 111

B Transmission Electron Microscopy Study **113**

B.0.1 Sample Preparation 113

B.0.2 TEM Study 114

C Technological Processes **121**

C.1 Samples Cleaning Process 121

C.2 Growth Parameters 121

C.3 Dry Etching Process 122

C.4 Optical Lithography Process 122

C.5 E-Beam Lithography Process 123

C.6 Oxygen Termination of the diamond surface 123

C.7 Rapid Thermal Annealing of the Ohmic contacts 124

C.8 Mobility Measurement 124

D List of Symbols **127**

E Bibliography **131**

List of Figures

2.1 Power and frequency capabilities of different semiconductors. 6

3.1 Face-centered cubic lattice of diamond with the lattice constant $a = 3.566$Å 9
3.2 The band structure of diamond after [1]. 10

4.1 The carbon phase diagram. After [2] 15
4.2 A schematic diagram of the HTHP cell. after [3] 16
4.3 Raman spectra of 4 different intrinsic CVD layers showing the typical 1332 cm^{-1} peak with a width of 2 cm^{-1} 18
4.4 Schematics of the processes occurring during diamond CVD growth. 20
4.5 Schematic of the role of atomic hydrogen in the diamond CVD growth. . . 20
4.6 HTHP stones with a diamond film epitaxially grown on top. The substrate on the bottom right corner has FETs fabricated on it. 23

5.1 Schematic doping configuration of phosphorous, nitrogen and boron doping in diamond. 26
5.2 Cathodoluminescence spectra of 5 nitrogen doped thick layers with different nitrogen to methane concentrations. (measured by G. Prince, Semiconductor Physics Department, Ulm University.) 29
5.3 Hydrogen induced $p-$type channel. The origin of the acceptors is still unclear [4]. 31

6.1 Simplified schematic of the MWPCVD machine used in the $\delta-$doping process. To be noticed is the solid boron source introduced in the plasma ball. . 34
6.2 Linear cyclic voltametry scan of boron delta-doped layer on the surface of (100)-oriented diamond substrate in 0.1 MH_2SO_4 electrolyte. The scan rate was 50 mV/s, as shown later on in Figure 8.9 a). 36
6.3 The acceptor profile of a single boron delta-doped layer extracted from capacitance-voltage characteristics of the diamond-electrolyte junction in 0.1 MH_2SO_4 at 1.0 kHz oscillation frequency. The dashed curve shows the Gaussian profile calculated for the Debye length, corresponding to the peak concentration of 10^{21} $1/cm^3$ electrolyte. 37

6.4 A depth profile of a delta doped layer showing the doping profile along with the actual carrier profile. 39

6.5 Typical epitaxial cycle of the growth used for the fabrication of a double delta transistor design. 40

7.1 $4\ PL$ spectra of the delta layers showing a week boron related peak. (measured by G. Prince, Semiconductor Physics Department, Ulm University) . 44

7.2 A typical TLM measurement of a single delta layer. 45

7.3 A typical window of a cyclic voltametry measurement on single crystal diamond, showing a $3\,V$ water dissociation window. (Measured by A. Denisenko). 46

7.4 Free carrier profiling $C-V$ measurement showing the independence of the measurement on the applied frequency. (Measured by A. Denisenko). . . . 46

7.5 Debye tails plotted along a $C-V$ measurement of a delta layer, matching very well to each other. 47

7.6 STM scan of $10 \times 10\,nm^2$ area of a boron doped delta layer, where no boron clusters could be identified. 48

7.7 AFM scan of a polished substrate without any CVD growth. Roughness $RMS = 1.9\,nm$ and peak to peak $8\,nm$ 49

7.8 AFM scan of a substrate without any CVD growth, polished using the new polishing technique. Roughness $RMS = 1.5\,nm$ and peak to peak $4\,nm$. 49

7.9 AFM scan of a substrate with a $100\,nm$ CVD intrinsic layer on top of it; polished using the old polishing technique. $RMS = 3\,nm$ and peak to peak $11\,nm$ 50

7.10 AFM scans after each growth hour at very slow growth rate, showing the improvement in the surface roughness. 51

7.11 AFM scan of a stack of 4 delta layers grown on top of each other. $RMS = 0.3\,nm$ and peak to peak is $\approx 1\,nm$. 51

7.12 AFM image of the epitaxially grown surface of diamond: a) the surface of the intrinsic buffer layer of $200\,nm$ thickness grown on the polished surface of the diamond substrate; b) the surface of the stack of the delta-doped spikes on top of the intrinsic layer. 52

7.13 Example of a SIMS profile of the delta layers. Concentrations higher than $10^{20}\,cm^{-3}$ were reached with a FWHM of about $5\,nm$. 53

7.14 ERD profile of a typical single boron delta-doped profile on diamond. The dashed vertical line showed the approximate starting depth of the nominally undoped layer grown on top of the delta-doped spike. 54

7.15 ERD profile of a multiple stack of boron delta-doped profiles grown in one growing process with various durations of the doping pulse. 55

7.16 The FWHM of the doping spikes in Figure 7.15 versus the duration of the doping pulse. The doping pulse was counted starting from the injection of CH_4/H_2 gas mixture into the reaction chamber up to plasma switch-off. . 56

8.1 Cross section of a MESFET structure device. 57

8.2 Cross section of a P-I-P transistor device. 59

8.3 Cross section of a P-I-P transistor device. 60

8.4 Current drop in $\%$ versus the etching depth d beyond the delta layer thickness, for a gate length of $0.2\,\mu m$.[5] 60

8.5 Effect of the over etching depth d on the output characteristic of a simulated P-I-P device.[5] 61

8.6 Different concepts of transistors realized so far on diamond. These concepts are limited to unipolar devices, with no hetero-junction p/n FETs. 62

8.7 Cross section of the two most promising device concepts relying on the delta doped channel, namely a) MISFET concept and b) MESFET concept . 63

8.8 Schematic doping profile for the fabrication of a double delta FET device.[6] 64

8.9 a) Schematic cross section of the ion sensitive FET with boron doped channel including the equivalent circuit of the diamond electrolyte interface, and b) the layout of a single micro ISFET fabricated on single crystal diamond substrate. 66

9.1 Transistor fabrication mask with circular gates. 69

9.2 Microscopic images of some circular shaped transistors during different processing stages. 70

9.3 New improved mask with linear gate structures encountering for the surface polishing lines. 71

9.4 Sample of the normal $3.6 \times 3.6\,mm^2$ size divided into four fields, adding a degree of freedom into the fabrication cycle. 71

9.5 Fabrication step sequence for the example of a P-I-P transistor device. . . . 72

9.6 The high temperature metal sequence used in the fabrication of the ohmic contacts. 72

9.7 Cross section design of a single delta MESFET with gate recess and field plate. 73

9.8 Calibration measurement showing the diamond etching rate as a function of the structure width. RF power is $25\,W$ on a 6 inch electrode. 74

9.9 processing flow chart for the single delta FET device. 75

9.10 Simplified cross section of the MIS device geometry with single delta layer. 76

9.11 AFM image of the diamond epitaxial layer after the growth of $250\,nm$ of the intrinsic buffer, the boron delta-doped channel and the diamond cap layer of $25\,nm$ thickness. The RMS smoothness value of the surface was $0.2\,nm$ while the peak to peak value was less than $1\,nm$ 78

9.12 (a) A schematic cross-section of a single MISFET device structure showing the etched mesa, ohmic contacts and the gate recess with $Al-$oxide insulating layer. (b) a micrograph of the device. 79

9.13 A typical TLM measurement in the recess structure for the evaluation of the sheet resistance and the contact resistance. 80

9.14 Schematic of a sample's cross section with metal free overgrowth capability. 81

9.15 SEM pictures of FETs and etched markers for alignment of all the processing steps. 82

10.1 DC characteristic after a further etching cycle for the gate recess was performed. 85

10.2 Results of the $S-$ parameter measurement of the double delta transistor along with the extracted f_T and the chosen bias point.(Measured by U. Spitzberg) 86

10.3 Example of an output characteristic of a single delta channel $MISFET$ showing no saturation behavior with channel current modulation at $150\,^{\circ}C$. 86

10.4 comparison between the output characteristic of a single delta MISFET device at room temperature (bottom) and at $100\,^{\circ}C$ (top) displayed in the same current and voltage scale. 87

10.5 DC output characteristic of the simplified MIS single delta transistor. . . . 88

10.6 (a) Schematic cross-section of the diode structure and (b) the extracted carrier profile of the boron-doped layer from the $C-V$ measurements at a frequency of $0.5\,MHz$. The solid line shows the theoretical Gaussian profile using the Debye length corresponding to the maximum carrier concentration 89

10.7 TLM measurement of the channel sheet resistance and the ohmic contact resistances of the boron delta-doped channel with the etched ohmic contacts. 90

10.8 Arrhenius plot of the conductivity of the boron delta-doped profile. 91

10.9 DC output characteristics of a single MISFET structure with the gate length of $0.8\,\mu m$. The measurements are at room temperature 91

10.10(a) The schematic cross-section of a MISFET and the equivalent circuit showing the parasitic elements (b) transfer characteristics of the device in Figure 10.9 at V_{DS} of $-15\,V$. The corresponding fitting curves for the extrinsic V_{GS} and intrinsic U_{GSint} gate biases are shown by the solid curves. . 93

10.11Small signal characteristics of a MISFET device with the gate length $L_g = 4\,\mu m$. The bias point of the RF measurements was the drain bias of $-25\,V$ and the gate bias of $-5\,V$ (Measured by U. Spitzberg and N. Alomary.) . . 94

10.12$a)$ The output and $b)$ the transfer characteristics of a micro-$ISFET$ with boron-doped channel and a gate length of $20\,\mu m$. The dashed arrow shows the conductivity in air. [7] 95

10.13Sequence of pH tests with the ISFET structure in $pH = 1$ and $pH = 13$ electrolytes. the fabrication process and passivation is according to section 8.5 96

10.14$a)$ Cyclic voltammetry and $b)$ capacitance voltage plot of diamond electrode with the boron delta doped channel in $0.1\,MH_2SO_4$ solution. The voltammogram was recorded after several complete cycles in the electrolyte. The arrow in $b)$ indicates the projected flat band potential V_{FB} of $8.8\,V$. 97

10.15Cross section of a P-I-P transistor device, already discussed in chapter 9.4, with $150\,nm$ channel length. Thickness $Al_2O_3 = 20\,nm$ and recess depth is $5\,nm$ 98

10.16DC characteristics of the P-I-P transistor with the delta layers. 98

10.17Slope of 2 in a semi-logarithmic scale of the $P-I-P$ output characteristic proving that the measured current might be indeed an injection current. . . 99

10.18RF measurement of a P-I-P transistor showing an f_T of $70\,MHz$. (Measured by U. Spitzberg and A. Kaiser) 100

10.19Extracted equivalent circuit from the measured S parameters. 100

A.1 H concentration in Hot Filament CVD.After [8]. 104

A.2 Photograph of fabricated ISFET 106

A.3 Cross section Sketch of the ISFET 107

A.4 Cyclic voltammetry of the $ISFET01221$ 108

A.5 Output characteristic of $ISFET01221$ 109

A.6 Transfer characteristic of $ISFET01221$ with multiple measurements for reproducibility purposes. 109

A.7 Stability over cycles of $ISFET01221$ 110

B.1 Sample after steps 4 and 5 113

B.2 Lamellae at step 7 (side view and top view) 114

B.3 Two lamellae attached to the grid (left), view of lamellae after step 9 in secondary and back scattered electrons. 114

B.4 Lamellae made for CTEM.(Graph taken by Dr. Andrey Chuvilin) 115

B.5 Near surface region.(Graph taken by Dr. Andrey Chuvilin) 116

B.6 The same sample after Ar ion "cleaning". (Graph taken by Dr. Andrey Chuvilin) 117

B.7 Near surface region in $STEM$. (Graph taken by Dr. Andrey Chuvilin) . . . 117

B.8 $EELS$ spectrum of the subsurface region.(spectrum analyzed by Dr. Andrey Chuvilin) 118

B.9 High resolution image of the surface.(Graph taken by Dr. Andrey Chuvilin) 118

B.10 EELS spectrum of the subsurface region.(Graph taken by Dr. Andrey Chuvilin)119

B.11 B $EELS$ map of near surface region. Bright spots in the up-left corner correspond to the protection layer.(Graph taken by Dr. Andrey Chuvilin) . . 119

C.1 PCB design suitable for the mobility measurement using the Hall and Van der Pauw technique. 125

C.2 A complete fabrication cycle of a double delta FET device. 126

List of Tables

3.1 Basic physical constants of diamond compared to other semiconductors . . 11

3.2 Electronic and thermal properties of diamond in comparison with other semiconductors 12

3.3 Figures of merit for diamond compared with GaN and $SiC(4H)$. 13

4.1 Diamond classification based on impurity concentration. After [9] 23

6.1 Preparation steps proceeding the growth of the delta layer. 41

6.2 Summary parameters for the growth process of the delta layer. 42

C.1 Procedure for samples cleaning before any other technological step. 121

C.2 Growth procedure for MPCVD samples used in the fabrication of surface channel $FETs$ 122

C.3 Plasma Dry Etching Process used for MESA etching as well as for recess etching. 122

C.4 Optical lithography process for MESA etching. 122

C.5 Optical lithography process for Lift off process of the ohmic contacts. . . . 123

C.6 E-Beam lithography process for recess etching. 123

C.7 E-Beam lithography process for gate lift off. 123

C.8 Oxygen Plasma Termination of the diamond surface, μ etch machine. . . . 124

C.9 Wet chemical Oxygen Termination of the diamond surface. 124

C.10 Rapid Thermal Annealing of the Ohmic contacts. 124

Chapter 1

Summary

During the last two decades, there has been a tremendous increase in demand for electronics in almost every domain of our daily life. Soon enough, the already existing Si technology could not anymore meet the very strict requirements of electronic applications demanding, for example, high power levels and working at high temperature and high frequencies. Hence, there was the urgent need to step up into a new generation of semiconductor technology relying mainly on wide band-gap materials. To meet these purposes, diamond is one of the most suitable wide band-gap material due to its outstanding figures of merit as well as its electrical, thermal and mechanical properties. Two main obstacles preventing the fast improvement of diamond devices are the lack of shallow dopants and the difficulty in the growth of large area single crystal diamond substrates. Hence, diamond electronic devices are still in the proof of concept phase, awaiting serious "'Brake-through"' results. However, in the past few years, a respectable variety of passive and active devices has been developed, simulated, fabricated and analyzed. These state-of-the-art results include, for example, hydrogen-induced channel FET's showing cut-off frequencies f_T of $45\,GHz$ and f_{max} higher than $120\,GHz$, with saturated output power of more than $2\,W/mm$ at $1\,GHz$. Serious drawbacks of such hydrogen-induced channel MESFET's however is the channel thermal and chemical instability to surface conditions as well as the restriction to planar device configurations. And this is exactly where the δ-channel FET devices come into play, offering solutions addressing the stability problems using an alternative δ-doping technique. As will be shown later in this work, state of the art results have been achieved with such δ-doped channel devices, including more than $30\,mA/mm$ DC current densities and cut-off frequencies higher than $1\,GHz$. These state-of-the-art results have developed out of a collaboration project between $ElementSix$ [1] and the Ulm University, with focus on the following:

- Identification of detailed design issues and key parameters for the device specifications.
- Design of a suitable processing scheme and the associated mask set, which takes into account all the characterization and measurement methods (Hall, TLM, Schottky diodes, $\Pi-$geometry and $T-$geometry...) as well as the geometrical scaling parameters (length and gate width....)

[1] $ElementSixLtd$ ($E6$, King's Ride Park, Ascot, United Kingdom) is a global leader and innovator in the development and manufacturing of advanced materials such as synthetic diamond and cubic boron nitride.

- Proof of the ability of a uniform and homogeneous controlled boron delta doped diamond growth process with:
  - Single delta doped layers
  - multilayer doped diamond structures
- Development and implementation of a contact technology for:
  - low resistive ohmic contacts ($< 10\,m\Omega.cm^2$)
  - Schottky contacts of high robustness with high breakdown voltage.
- Design of a technological process suitable for wafer-scale processing.
- Development of the technological building blocks for MESFET and P-I-P configuration
- Integration of the building blocks into a fully working FET structure, MESFET, MISFET and P-I-P
- Demonstration of a fully operational device with DC and RF characterization
- Benchmarking for a target of $10\,W$ at $X-$band against alternative technologies.

The final target of this investigation has been to develop a diamond transistor device (either MESFET or MISFET) relying on the delta doping as a channel active area, which is able to show high source-drain current in the mA/mm level and high speed performance of f_t in the low GHz regime, operating at room temperature. This transistor must have the ability to show full modulation capability, such as the saturation of the source drain current as well as full pinch-off behavior.

The concept of a diamond FET structure based on boron doping, and especially delta doped channel has been investigated technologically. The aim had been to develop a technological process, which enables the fabrication of thigh power transistors for application in the microwave regime.

Based on previous work at Ulm, a basic platform was established, allowing the characterization of the diamond material in a first step. This included the characterization on intrinsic, $n-$doped (nitrogen) and $p-$doped (boron) diamond material using photoluminescence measurements, AFM for surface morphology, XPS, and other methods.

Following this step, a very precise growth technique was developed, allowing the growth of very thin ($1 - 2\,nm$) and highly boron doped ($10^{20}\,cm^{-3}$ to $10^{21}\,cm^{-3}$) layers, which are referred to as "delta doped layers" and which are the key aspect in this work.

These delta doped layers were also strongly investigated, since they have served later as the channel for the FET devices. The investigation of these delta layers included electrical measurements (sheet resistance, activation energy, capacitance-voltage, mobility) as well as physical/chemical measurements including Elastic Recoil Detection (ERD), Secondary Ion Mass Spectroscopy (SIMS), Transmission Electron Microscopy (TEM), Atomic Force Microscopy (AFM) and Scanning Tunneling Microscopy (STM), which gave us a better understanding for the properties of these layers.

Finally, the knowledge gained from these investigations allowed to develop a technological processing routine for the fabrication of several types of FET device structures. The main concepts investigated were P-I-P FET devices and single delta channel and the double delta channel MESFET and MOSFET configurations.

Even though the processing windows for fully functional devices was found extremely narrow, it had been possible to demonstrate the first fully operational MOSFET device based on the delta channel concept at room temperature and in the low GHz range. DC current densities of more than $30\,mA/mm$ and cut off frequencies in the range of $1\,GHz$ have been obtained.

Chapter 2

Introduction

Life in the third millennium is infiltrated with ever advanced semiconductor devices, from household instruments to industrial machines, not to forget communication in all of its ways. The rapidly growing demand for microelectronic components is not only quantitative, but more qualitative. Nowadays, applications requiring high power and high temperature management are becoming more demanding since the traditional semiconductors used in these applications, like Si, Ge and GaAs, have reached their theoretical limit. These materials, in special cases, can no more meet the requirements of modern applications, which includes thermally and mechanically stressed devices (e.g. sensors employed in harsh conditions), and the need of compact design (like in the case of phase array radars) that have excellent heat handling and dissipating capabilities. Hence wide band gap semiconductors like SiC, GaN and diamond have been proposed as the future semiconductors due to their excellent electrical properties (larger band gap, higher mobilities, higher breakdown voltages, etc.), and their thermal and mechanical stability, which as a result offer the best conditions for ISFET devices. Diamond is an allotrope of carbon which shares the fourth group of the periodic table along with Si and Ge. But despite the wide range of extraordinary properties of diamond its use has been limited mainly due to its rarity and cost. The variety of diamond applications have emerged due to the recent progress in diamond growth and synthesis. Many industrial sectors, ranging from cutting tools to electronics, have taken advantage from the continuous improvement of High Temperature High Pressure and CVD diamond substrates. Especially mechanical properties, such as extreme hardness and a low friction coefficient combined with chemical inertness predetermine diamond as a material for protective coatings for cutting and grilling tools. Its optical transparency from the infrared to the ultraviolet region can be used for optical windows [10]; the fact that Diamond has the highest thermal conductivity of all materials makes it an ideal heat-sink and its excellent radiation hardness is used in radiation detectors [11, 12]. Although Diamond is successfully applied in mechanical, thermal and optical applications, the exploitation of its unique electronic properties (large band gap, high carrier mobilities, high breakdown field, etc.) has not yet been achieved.

Unfortunately, diamond is lacking the proper driving force in terms of material development. Despite the properties of diamond that makes it compete with other wide band gap semiconductors, the balance is currently tipped in favor of SiC and GaN materials due to doping challenges and wafer size limitation of diamond substrates. The area in which dia-

mond research is expanding now includes a wide range of MEMS applications [13], such as micro actuators and switches [14, 15], micro membrane pumps [16] and ink jets for microfluidic systems [17] thanks to its mechanical stability and chemical inertness. Moreover, since diamond is a bio-compatible material, the recent boom in biomedicine has opened new opportunities for its application in the health care sector [18, 19, 20]. The optimum benefit from diamond properties would be in the field of electrochemistry, as well as in high power, high frequency applications. At the moment, vacuum tubes serve as the solution for broadcasting, communication satellites and radars which require high RF output power densities (kilowatts of power in the GHz frequency range). The problem of vacuum tubes is the low efficiency which leads to high energy losses and increased requirements for heat dissipation. The use of diamond FETs would minimize these problems to the extreme. Diamond possesses the highest thermal conductivity among all materials of $22\,W/cmK$, so heat can be be spread easily and rapidly. Moreover, diamond FETs are expected to operate at very high voltages due to large band gap of $5.45\,eV$ [21]. The high carrier mobilities of $4500\,cm^2/Vs$ for electrons and $3800\,cm^2/Vs$ for holes [22], and saturation velocity of approximately $1.10^7\,cm/s$ for both electrons and holes enable diamond FETs operation in high-frequency range.The suitability of diamond for such applications may be described by the Johnson figure of merit which is used to theoretically assess high-frequency high-power capabilities of semiconductors. For diamond this figure is many times better than any other semiconductor [23] as can be seen in Figure 2.1, which shows the dominance of diamond as the ultimate semiconductor for power and high frequency operations compared to other semiconductors.

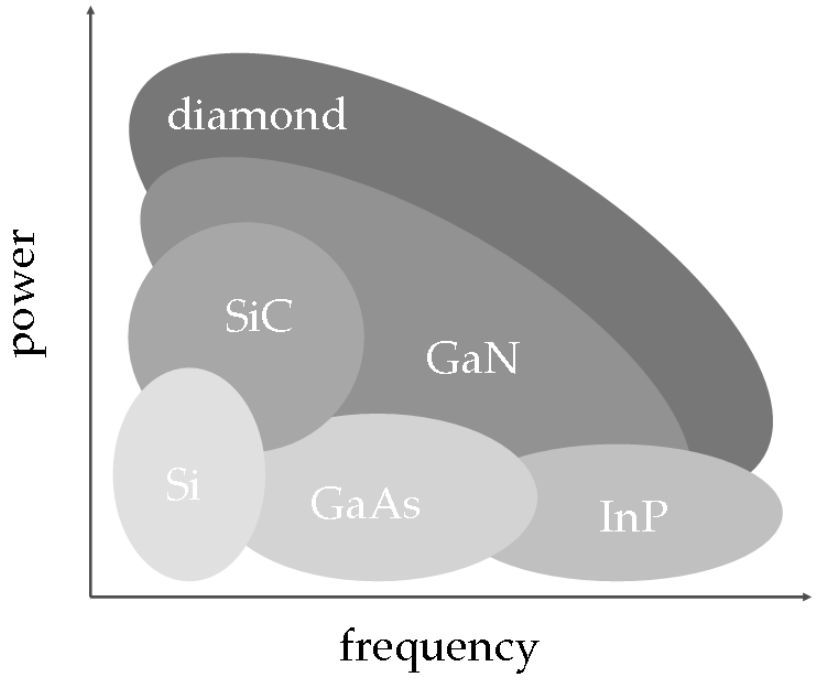


Fig. 2.1: Power and frequency capabilities of different semiconductors.

As mentioned earlier, the first limitation and central issue of diamond is the doping. So far an effective doping of p-type only has been achieved through the use of Boron. Boron in turn is a deep acceptor but its activation energy is decreased by increasing the concentration. The activation energy becomes negligible at concentrations above $10^{20}\,cm^{-3}$, but the mobility becomes low. The n-type doping by nitrogen or phosphorous is not effective enough to produce high electron densities at R.T., thus this type of doping is not suitable for high performance devices.

The second limitation is the diamond chip size. Till date, electronic devices have been realized mainly on HTHP single crystals with $\approx 4 \times 4\,mm^2$ limited size. Homoepitaxial electronics diamond layers can grow on these stones by microwave plasma CVD. Although heteroepitaxial growth of diamond on foreign substrates in polycrystalline layers are well suited for MEMS applications such as RF switches [24] this is not the case for high performance electronics. Recently, heteroepitaxial growth on Iridium has been achieved [25], producing a single crystalline quasi-substrate used for fabrication of FET devices [25]. This result marks an encouraging starting point and offers a new potential for the integration of active and passive devices into high power MMICs.

Taking these two limitations into account, this work emphasizes first of all on the high potential and possibility of Diamond electronic devices. It is organized as follows:

- The structure and properties of diamond as a physical element are discussed in chapter 3, showing the theoretical potential of diamond, along with the most important figures of merit in comparison with other wide band semiconductors.
- The growth of diamond is discussed in chapter 4, showing the different mechanisms involved together with different growth techniques.
- In chapter 5, doping in general is presented and discussed, showing the different possibilities of $n-$ and $p-$ doping, as well as giving a short introduction to the hydrogen induced conductivity in diamond.
- Chapter 6 explains the delta doping principle, its ideal properties, its target window in FET application, going through the technical problems and limits of boron monolayer-like planar doping.
- The characterization of the growth technique, which was described in chapter 6, will be discussed in more details in chapter 7. This chapter constitutes the fundament of the work to follow, since it represents the suitability of the delta doped layer approach which will be used later in the fabrication of field effect transistors.
- In chapter 8, the basic concepts of transistor processing on diamond will be shown and compared with transistors on other materials. Here, the already successful but unstable transistor on hydrogen terminated diamond will be briefly shown, and the discussion will provide the motivation to pursue the delta doped FET as the most promising device on diamond.
- The fabrication and technical details are shown in chapter 9, presenting fabrication details which led to fully operating devices. Here, many fabrications steps, techniques, recipes and tricks are presented in details.

- Chapter 10 summarizes the results concerning previously fabricated devices, showing the AC and small signal measurements of different structures of delta doped FETs.
- and chapter 11 will summarize and conclude this work.

Chapter 3

Properties of Diamond

Beside the other carbon structures like Graphite, Fullerene and nano-tubes, diamond is a unique structure that exhibits many extra-ordinary physical properties. It is the hardest known material with the highest thermal conductivity and highest elastic modulus. Diamond is also optically transparent, chemically inert, and biocompatible.

3.1 Crystal structure

Diamond is a thermodynamically metastable phase of carbon, while graphite is the stable phase. The carbon atom has six electrons with the following configuration: $1S^2 - 2S^2 - 2P^2$. Two of those electrons are located near the atom nucleus and do not participate in chemical bonding. The other four uppermost electrons constitute the valence electrons and participate in chemical bonding.

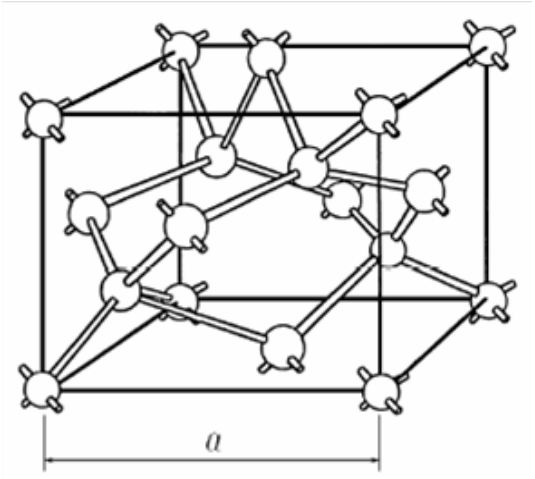


Fig. 3.1: Face-centered cubic lattice of diamond with the lattice constant $a = 3.566$Å

In diamond the valence electrons are spread between one S and three P orbitals forming SP^3 hybridization. Carbon atoms are then covalently bonded by σ-bond; 1.54 Angstroms

in length and with an angle of $109°$, forming a tetrahedral structure. The resulting crystal structure in Figure 3.1 can be described as two face-centered cubic (fcc) lattices shifted along the diagonal of the unit cell by one quarter of the length of the diagonal, and has two atoms per primitive unit cell [26]. The lattice constant a is 3.566 Angstroms [27]. The extraordinary properties of diamond are a result of this tightly packed structure and the high symmetry of the lattice, along with the strong $\sigma-$ bond.
In graphite the carbon atoms possess SP^2 hybridization. Each carbon atom is covalently bonded with the four neighboring atoms through three strong $\sigma-$ bond and one weak $\pi-$ bond. The electrons which are $\sigma-$ bonded do not belong anymore to single graphite atoms. In this case, these electrons are referred to as dislocated electrons, vertically bonding the graphite comb rings weakly between each other [28]. The stronger bonds that diamond crystal possesses, and its tight tetrahedral structure and high symmetry are the key reasons for the unique properties of diamond, over the other carbon structures.

3.2 Band Structure

Undoped diamond is an insulator with a large band gap of $5.45\,eV$ at Room Temperature [1]. The band structure of diamond as shown in Figure 3.1 is relatively simple, compared to other materials. The valence band maximum is in the $\Gamma-$ point ($\kappa = 0$) and the conduction band minimum can be found at approximately $80\,\%$ of the $X-$ point in the $< 100 >$ direction.

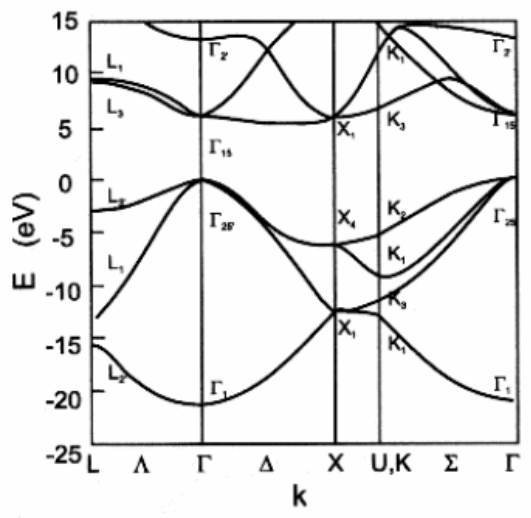


Fig. 3.2: The band structure of diamond after [1].

Just as in the case of Si, the valence band in the $\Gamma-$ point degenerates with two different valence band curvatures, resulting in two different effective masses for the holes. So we will have "heavy holes" with mass $m_{hh} = 0.57\,m_0$, and "light holes" with mass

$m_{lh} = 0.32\, m_0$. A third band, called the split-off band is only $0.006\, eV$ below the first two bands. This amount of energy is much smaller than the thermal energy at Room Temperature ($0.026\, eV$), so the holes in this band contribute in conduction even at low temperatures [29]. Electrons in diamond have two different electron masses; longitudinal mass $m_{le} = 1.4\, m_0$ and transversal mass $m_{te} = 0.36\, m_0$ [30]. The same also holds for the various holes.

3.3 Electrical Properties of Diamond

In comparison to other semiconductors, diamond ideally exhibits unique electrical properties. Diamond has a large band gap of $5.45\, eV$, high carrier mobilities of $4500\, cm^2/Vs$ for electrons and $3800\, cm^2/Vs$ for holes, high saturation velocities of $1.6 \times 10^7\, cm/s$ for electrons and $1.1 \times 10^7\, cm/s$ for holes [22], high breakdown electric field of $10\, MV/cm$ [21] and low dielectric constant of 5.7 . Another very important property of diamond is the thermal conductivity at Room Temperature ($22\, W/mmK$) which is the highest among all other materials [23].

3.4 Diamond as a Semiconductor

The excellent qualities of diamond can be better appreciated when compared to other relevant semiconductors. Table 3.1 and Table 3.2 summarize the physical and electrical diamond properties compared to other competing wide band gap semiconductors like GaN and SiC (4H), in addition to common semiconductors like Si and GaAs.

Tab. 3.1: Basic physical constants of diamond compared to other semiconductors

Property at R.T	Diamond	GaN	$SiC(4H)$	Si	$GaAs$
Band gap (eV)	5.54	3.44	3.27	1.12	1.42
Type of band gap	Indirect	Direct	Indirect	Indirect	Direct
Lattice constant (nm)	0.356	a = 0.319 $c = 0.519$	a = 0.308 $c = 1.005$	0.543	0.565
Density (g/cm^3)	3.515	6.15	3.216	2.321	5.32

To evaluate the potential stand point of diamond as a semiconductor, a look at figures of merit is very useful. Here, we will look at the Johnson figure of merit (JFM), the Keyes figure of merit (KFM) and the Baliga figure of merit (BFM). The mathematical expressions of those figures are listed in the equations 3.1, 3.2 and 3.3.

Tab. 3.2: Electronic and thermal properties of diamond in comparison with other semiconductors

Property at R.T.	Diamond	GaN	$SiC(4H)$
Relative dielectric constant ϵ_r	5.7	9.0	9.7
Breakdown electric field ($10^6\, V/cm$)	10	3	3
Mobility for Electrons μ_n (cm^2/Vs)	4500	1200	1600
Mobility for holes μ_p (cm^2/Vs)	3800	30	1140
Electron's saturation velocity v_{sat} ($10^7\, cm^2/Vs$)	1.6	2.5	2
Hole's saturation velocity v_{sat} ($10^7\, cm^2/Vs$)	1.1	2	0.3
Thermal conductivity λ (W/cmK)	22	1.3	4.9
Specific heat capacity C_P ($J/molK$)	6.2	32.7	-

$$JFM = \left(\frac{E_{br} \cdot v_{sat}}{2 \cdot \pi}\right)^2 \tag{3.1}$$

The JFM describes the high speed power handling capability of diamond, which is a very interesting figure of merit for diamond since it is focused on power electronics at high frequencies [31]. As can be seen from equation 3.1, this figure of merit depends on the quadratic product of the breakdown field and the saturation velocity. The breakdown field is the maximum voltage that can be applied and the saturation velocity represents the maximum current.

$$KFM = \lambda \cdot \sqrt{\frac{c \cdot v_{sat}}{4 \cdot \pi \cdot \epsilon_r}} \tag{3.2}$$

The KFM is used to estimate the switching speed and the thermal dissipation capabilities of transistors [32]. This figure of merit evaluates the applicability of different semiconductors for digital circuits with high integration density, where the main problem is the heat dissipation. The thermal dissipation is considered in the thermal conductivity (λ). The ratio between the saturation speed and the dielectric constant is a measure of the switching speed of the device and the dielectric losses in the material.

$$BFM = \epsilon_r . \mu . E_G^3 \tag{3.3}$$

One last further aspect which should be also taken into account when dealing with high power devices is the power loss, which is described by the Baliga Figure of Merit, as shown in Equation 3.3.

Table 3.3 compares the figures of merit mentioned above for diamond, GaN and SiC (4H). The figures were calculated with the help of tables 3.1 and 3.2.

Tab. 3.3: Figures of merit for diamond compared with GaN and $SiC(4H)$.

Figure of Merits at R.T.	Diamond	GaN	$SiC(4H)$
$(JFM)_n$	4.75	0.30	1
$(JFM)_p$	3.94	-	0.39
$(KFM)_n$	7.11	1.78	1
$(KFM)_p$	3.36	-	-
$(BFM)_n$	7.43	1.34	1
$(BFM)_p$	6.08	-	0.14

It is worth to mention that the above comparison is not totally fair, since all the GaN based devices rely on heterojunctions, which provide better mobilities and a higher N_S than bulk GaN. Unfortunately, heterojunctions in diamond are still not implemented for the time being.

Chapter 4

Concepts and Principles of Diamond Growth

Many attempts have been made in the last two centuries to grow artificial diamond. However, there was great difficulty in achieving this goal due to the fact that graphite is the thermodynamically stable form of carbon at room temperature and pressure. But since graphite and diamond are separated by a large activation energy; diamond, once formed, can not spontaneously convert to the more stable graphite phase. Thus, diamond is a metastable phase of carbon, i.e. kinetically but not thermodynamically stable.

The Carbon phase diagram shown in Figure 4.1 highlights two possibilities of realizing synthetic diamond, the HTHP process and the CVD process. The main features of both processes will be discussed below.

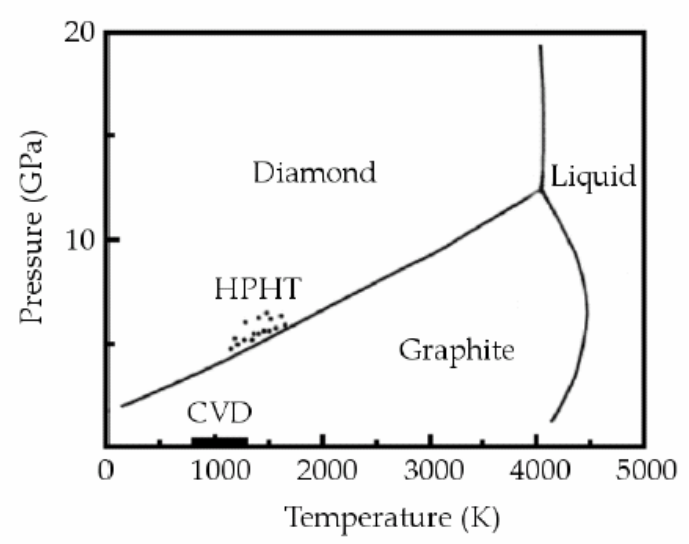


Fig. 4.1: The carbon phase diagram. After [2]

4.1 High Temperature High Pressure Growth (HTHP)

This process has been widely used for decades to fabricate artificial diamond and was the first method employed to fabricate industrial diamond like for cutting tools [33]. In this process, carbon is heated and compressed to reach the thermodynamically stable region. This is done in the presence of a molten catalytic metal with high solubility of carbon like Nickel, Iron, Cobalt or a mix of those metals. The catalyst molt can also contain metals like Ti or Cu in order to control the pureness of the diamond phase. The required pressure for this process is in the range of $5.5\,GPa$ and the temperatures are in the range of $1750°\,K$. During the process, a temperature gradient is formed in the molt. Diamond grows on a seed which is located at the cold side of this thermal gradient. A schematic display of this process along with HTHP cell is shown in figure 4.2.

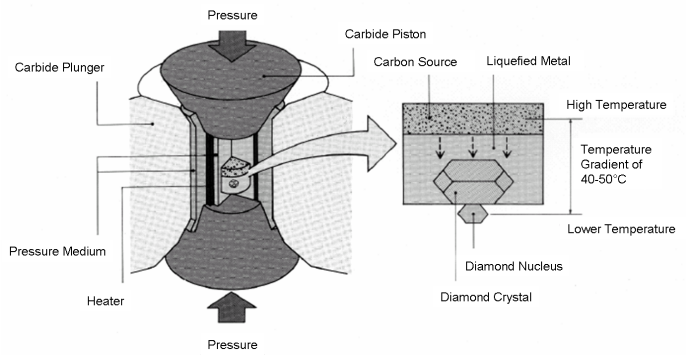


Fig. 4.2: A schematic diagram of the HTHP cell. after [3]

The disadvantage of the HTHP method is the small size of the crystal (few millimeters big) which presents a big limitation to the usage of such crystals in electronic applications.

The CVD process has an advantage in terms of energy consumption and can produce high quality diamond crystals to be used in electronic applications. This process can be divided into two techniques of main interest for semiconductor applications: the microwave plasma CVD (MWPCVD) and hot filament CVD (HFCVD).

4.2 Chemical Vapor Deposition (CVD)

The other possibility is diamond growth in the metastable area where both carbon phases are created, thus it is necessary to completely reduce the graphite phase during growth. This can be achieved using the chemical vapor deposition process (CVD) [34], where diamond is grown from a gas phase at much lower pressure and temperature than the HTHP process, thus the CVD process has a big advantage in terms of energy consumption and can produce high quality diamond films to be used in electronic applications.

The first successful attempt to grow low pressure diamond from the gas phase was achieved by W. G. Evershole in 1962 [35]. Here, a diamond substrate was subjected to hydrocarbon

and hydrogen gas alternatively at elevated temperatures. This resulted in graphite and diamond subsequently on the substrate but the graphite layer was always etched away by the following cycle of hydrogen gas leaving the diamond phase intact. The disadvantage of this process was the slow growth rate. Only the understanding of the role of atomic hydrogen allowed a controlled growth process [36]. Another important aspect was the possibility to grow diamond on other substrates different than diamond [37].

In general, the CVD process involves a chemical reaction in the gas phase above the substrate surface, which causes the deposition of carbon on the substrate surface [38]. The important reaction that allows this deposition with a controlled growth of the diamond film is as follows:

$$CH_4 + H_2 + Heat \Leftrightarrow Diamond + 2H_2 \tag{4.1}$$

The activation of the gas containing carbon and H_2 splitting into $2H$ can be achieved by thermal means (Hot Filament $CVD - HFCVD$) [39] or by electrical discharge (Microwave Plasma $CVD - MWPCVD$) [40].

In this work, the growth of the intrinsic diamond buffer layers starts with the cleaning of the samples as will be shown later. After cleaning, the substrates were transported using only ceramic tweezers (and no metallic ones) in order to avoid any metal re-contamination. Then, the growth process started with a 20 to $30\,min$ hydrogen plasma treatment of the surface for smoothing the polishing lines on the surface. AFM scans were usually taken before and after treatment and the results were compared. A typical improvement value of the surface roughness ranged from $1.5\,nm$ RMS to approximately $1.0\,nm$ RMS across an area of $10 \times 10\,\mu m^2$, as will be shown later in Chapter 7.

The apparatus used in this work is a modified $ASTEX$ 1500 $MPCVD$ reactor capable of $1500\,W$ microwave power and operating at $2.45\,GHz$. Many special changes have been made to this machine in order to meet the needs of our process. They were:

- A turbo pump capable of reaching a base starting pressure of $10^{-8}\,Torr$ was added.
- A magnetic transporter capable of inserting the solid boron source for doping inside the plasma without interrupting the vacuum was installed.
- A mass spectrometer for gas analysis during growth was added.

The generated plasma ball has a contact area with the sample holder of $\approx 1\,cm^2$, restricting the number of grown samples to only 1 per growth cycle to keep the growth homogeneous.

One of the most serious problems of the intrinsic growth process is the background concentration of boron in the chamber, as well as the N_2 and O_2 concentration for the growth rate control. Despite all efforts to minimize this boron contamination by pre-treatments (burn-out in oxygen etc.), the value of the residual boron concentration could not be suppressed below $2 \times 10^{17}\,cm^3$. Since only one apparatus was available for this investigation, the intrinsic layer thicknesses had to be chosen carefully not to generate parasitic parallel

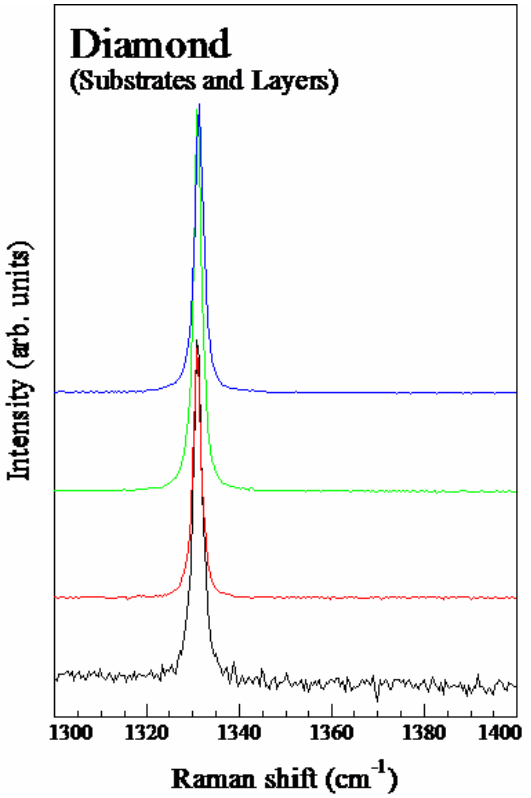


Fig. 4.3: Raman spectra of 4 different intrinsic CVD layers showing the typical $1332\,cm^{-1}$ peak with a width of $2\,cm^{-1}$

conduction paths (for example the dose of boron in the buffer should always be depleted by the nitrogen level in the Ib substrate).

Figure 4.3 shows four Raman spectra of $2\,\mu m$ thick CVD intrinsic buffers. The width of the typical diamond SP^3 peak at $1332\,cm^{-1}$ is in the range of $2\,cm^{-1}$. Also, no trace of any luminescence emerging from any SP^2 bonds was detected.

4.2.1 Hot Filament CVD (HFCVD)

The HFCVD process depends on electrically heated tungsten filaments to provide the activation of the carbon containing gas. Here the hydrogen and carbon sources (mostly Methane) are heated via the filaments up to $2500^\circ\,K$. The pressure range for deposition is in the interval of $1\,kPa$ to $10\,kPa$.

This method has a wide range of applications and is relatively cheap and simple, and produces large size films with good quality polycrystalline diamond on foreign substrates. Diamond films with a surface area of $0.5\,m^2$ could be grown [41]. However, this method suffers from two main disadvantages. The reaction of the hot filaments with gases and carbon atoms

reduces their lifetime and thus increases the deposition time. Moreover, the contamination of the diamond film with the filament material is unavoidable, producing diamond films acceptable for mechanical applications but not quit suitable for electronic applications.

4.2.2 Microwave Plasma CVD (MWPCVD)

In MWPCVD the growth is activated via an electrical discharge by coupling the microwave power into the deposition chamber via a quartz window. The chamber design assures that only one microwave mode is sustained in the chamber. After plasma ignition, microwave power is coupled in the gas phase electrons, which in turn transfer their energy to the gas through collisions. The heat of collision dissociates the gas molecules into reactive species and formation of active species, and finally the deposition of diamond onto the substrate.

Compared to HFCVD, MWPCVD can produce diamond films of higher quality. Growth rates up to nearly $10\,\mu m/hour$ have been achieved [42]. The gas pressure in the growth chamber is in the range of $0.1\,kPa$ to atmospheric pressure, but usually a pressure in the range of $1.5\,kPa$ to $15\,kPa$ is used. Although the MWPCVD uses smaller substrate sizes (depending on the plasma ball size), still it is the better choice for electronic applications.

In the CVD chamber, H_2, CH_4, O_2 and N_2 are used as process gases. A boron rod is mechanically introduced into the plasma as a $P-$type doping source. To allow sharp boron doped profiles, the movement of the rod is adjusted in a way that it can be introduced very fast into and out of the plasma. This system is used for the growth of both doped and intrinsic diamond layers. Due to the boron memory effect, the chamber is contaminated with boron even during the growth of intrinsic diamond. The background concentration of boron in the chamber is therefor in the range of $2.10^{17}\,cm^{-3}$. This concentration does not have noticeable effect on the FETs with hydrogen induced surface channel but can form a parallel conductive channel that causes buffer leakage [43] when the background concentration is too high. However this background concentration can present a serious problem for Schottky diodes, where high breakdown voltages are required. The problem of chamber contamination by boron can be solved by prior diamond overgrowth of the chamber walls or by mechanical cleaning of the system.

4.3 Principles of diamond CVD growth

Figure 4.4 illustrates the chemical and physical processes which occur during diamond CVD growth. The process gases (H_2 with approximately $1\,\%CH_4$) mix before diffusing toward the substrate. On the rout of diffusion, the molecules of these different species are cracked into reactive radicals and atoms ($CH_4 \Leftrightarrow CH_x \Leftrightarrow C$) creating electrons and ions, and heating up the system. Those reactive species continue to mix beyond the activation energy and undergo a complex set of chemical reactions until they reach the substrate surface. At the surface, the species can be adsorbed and react with the surface, desorb back into the gas phase or diffuse laterally on the surface until an appropriate reaction site is found.

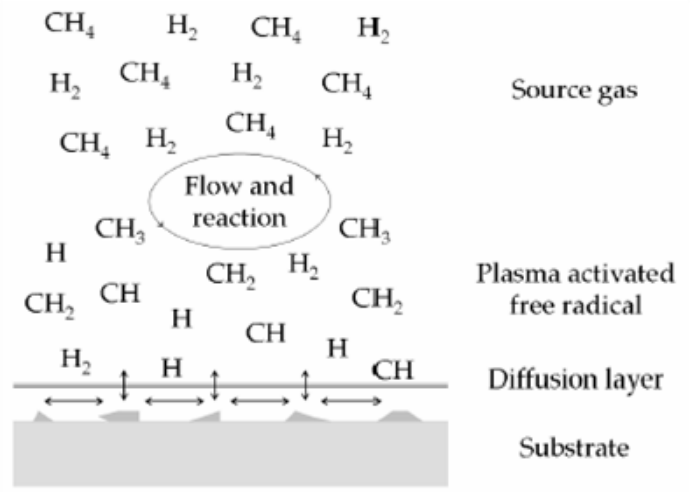


Fig. 4.4: Schematics of the processes occurring during diamond CVD growth.

The important role of atomic hydrogen in the CVD diamond growth can be explained with the model presented by T.R. Anthony in [44]. Here, hydrogen performs several functions that are necessary for diamond growth. Figure 4.4 describes those functions.

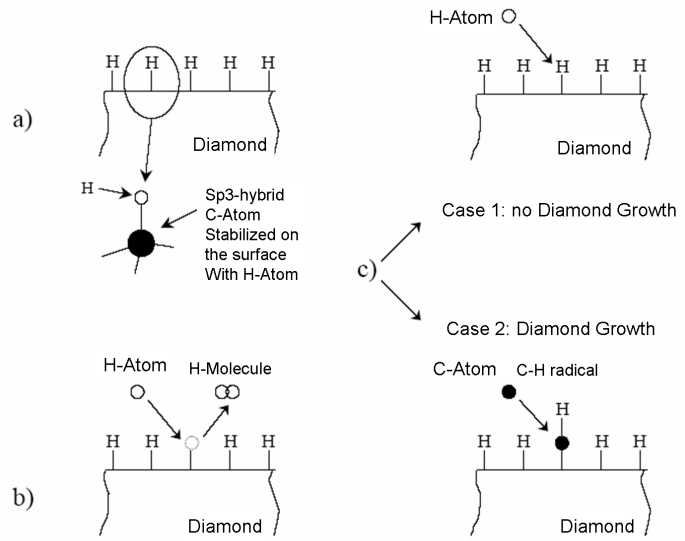


Fig. 4.5: Schematic of the role of atomic hydrogen in the diamond CVD growth.

The first function of atomic hydrogen is the stabilization of the diamond surface (Figure 4.5 a) which is a prerequisite of diamond growth. Each carbon atom of the free diamond surface has two or three non saturated valences (two on (100) oriented surfaces, three on (111) oriented surfaces). A surface reconstruction minimizes the surface energy through reciprocal binding of the free surface dangling bonds. Atomic hydrogen prevents the occurrence

of this reaction by bonding to the dangling bonds, and a hydrogen terminated surface is generated and the sp^3 hybridization of the carbon atoms is preserved.

On a hydrogen terminated surface, the diamond growth can be continued by adding carbon radicals. The $C-H$ bond has energy of $3.82\,eV$ which is stronger than the $C-C$ bond with $2.58\,eV$. To enable the continued growth of the diamond crystal, hydrogen should be abstracted from the surface. In this exothermic reaction, a hydrogen atom in the gas phase binds with another hydrogen atom at the surface forming a neutral hydrogen molecule (Figure 4.5 b). This reaction is exo-therm, since the $H-H$ bond energy ($4.25\,eV$) is stronger than the $C-H$ bond. The free site on the surface can be filled again by a carbon atom or a hydrocarbon radical. The latter case constitutes a $C-C$ bonding (Figure 4.5 c) and diamond can continue to grow. A higher hydrogen concentration presents a higher likelihood that a $C-C$ binding occurs. In fact, the diamond growth is more probable by linking radical hydrocarbon atoms rather than carbon atoms [45]. Atomic hydrogen etches both the diamond surface and the emerging graphite clusters, but the etch rate of diamond under CVD conditions is significantly lower than the etch rate of graphite under the same conditions and significantly lower than the growth rate of diamond. This results in a strong etch of the graphite clusters while maintaining the diamond growth.

Although diamond growth strongly depends on the hydrogen concentration in the gas phase, the dependence of growth rate on the carbon gas supply is astonishingly small. Thus diamond can be grown with a variety of carbon gases like CH_4, C_2H_2, CO and others. Often, the simplest of most hydrocarbons, methane (CH_4) is used. Methane can be utilized for growth regardless of the oxygen or hydrogen concentration in it. This independence is not achieved if CO is used.

The results of diamond deposition from the gas phase from different research groups and the dependency on the gas constituents was summarized by Bachmann in 1991 in the so called Bachmann diagram [46]. This diagram represents a ternary $C/H/O$ phase diagram where the borders of diamond growth for various gas constituents are highlighted. In this work methane was used for CVD epitaxy. The growth rate in the CVD process was determined by the gas, gas flow and the growth temperature on the substrate surface. These parameters affect not only the growth rate but also the morphology of the diamond films. The main parameter of the growth rate is the methane concentration. The growth rate increases substantially by increasing the methane concentration. However the diamond quality is also reduced with increasing methane concentration, through the sp^3/sp^2 ratio. On the other hand, the quality of diamond growth is improved with increasing gas fluxes, as could be shown in [47]. The influence of the layer thickness on the growth rate is neglected in this work since thick diamond substrates ($d > 100\,\mu m$) were employed.

The influence of temperature on the growth rate is discussed in [48]. These results suggest that the modification of the growth rate can be described by a larger thermal desorption of hydrogen from the diamond surface at higher temperature.

The morphology and defect density produced epitaxially in the diamond film depends heavily on the above mentioned growth conditions. High quality diamond films are produced

with extremely low growth rate, as was shown in [49]. The layers with the lowest defect density were produced at moderate temperatures and low methane concentrations, both in this work and in [49]. The growth conditions allow a so called step-flow growth mode in which the diamond layer continues to grow at the edge of an atomic monolayer step. Also, the crystal orientation has an influence on the defect density and morphology of the growing diamond layers. So far, the highest quality diamond films were produced on a (100) oriented crystals [49]. The quality of diamond films grown on (110) or (111) oriented substrates is significantly lower than that grown on (100) orientation. The (111) layers contain a high concentration of defects where the tetrahedral diamond structure is interrupted [21].

Another important parameter that affects the coating quality is the addition and the introduction of dopants during epitaxy. The addition of both boron and nitrogen leads to a degradation of the coating quality in mechanical applications. High concentration inclusion of boron causes tension in the diamond lattice, thus a much larger roughness of the layers. The degradation of the layer quality and the increased defect density in doped diamond films was also observed in [49].

4.4 Substrates

The choice of a suitable substrate is essential for the quality and properties of the diamond film. To obtain high performance electronic device structures, the substrate in analogue circuits need to combine an active transistor structure with a passive network. Both FETs and GHz waveguides have been demonstrated using diamond, thus diamond with its high thermal conductivity is an ideal candidate for high power MMICs if wafer-scale single crystal substrates could be developed. An approach to achieve this is the growth of MPCVD layers on (100) oriented HTHP chips. Such layers can be separated from their substrates and have yielded record hole and electron mobilities [22]. With a high lateral growth rate the chip size can be expanded from a $4x4\,mm$ seed to approximately $1\,cm^2$. Another promising approach is the heteroepitaxial growth of diamond on iridium [50], which in turn can be deposited onto $SrTiO_3$ [51, 52, 53], MgO [54, 55, 56, 57], sapphire [56] or CaF/Si [58] substrates. Nevertheless, until date, no atomically flat surfaces have been demonstrated on such substrates yet.

4.4.1 Single crystalline CVD diamond on HTHP stones

The electrical and optical properties of diamond substrates are determined by the boron and the nitrogen content. In particular, the difference in color is an important criterion in diamond classification as a precious stone. This classification was also conserved for synthetic diamond, where the color depends on the presence and concentration of boron or nitrogen. Table 4.1 gives an overview of the diamond classification. In this work type Ib HTHP stones were used as a substrate for homoepitaxial diamond growth, where the FETs and diodes are usually fabricated on top of an epitaxial buffer. Figure 4.6 shows an image of these substrates.

Tab. 4.1: Diamond classification based on impurity concentration. After [9]

Type	Color	Impurity	Position in the crystal	Concentration	Specific resistance
Ia	Bright yellow	Nitrogen	Substitution or platelet	$> 100\,ppm$	$> 10^{16}$
Ib	Yellow	Nitrogen	Substitution	$1\,ppm - 100\,ppm$	$> 10^{16}$
IIa	Transparent	Nitrogen	Substitution	$< 1\,ppm$	$> 10^{16}$
IIb	Blue	Boron	Substitution	$> 1\,ppm$	< 10

Up to now, a vast majority of state-of-art electronic devices was obtained on HTHP stones. Although, they will not allow wafer scale device manufacturing, these stones are still an attractive way to demonstrate discrete high performance diamond devices.

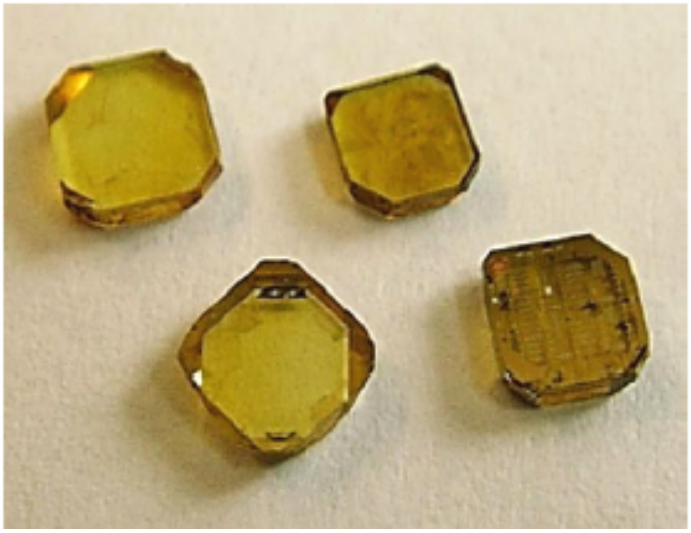


Fig. 4.6: HTHP stones with a diamond film epitaxially grown on top. The substrate on the bottom right corner has FETs fabricated on it.

Chapter 5

Bulk Doping of Diamond

The physical properties of diamond were presented in the previous chapter and predict a very promising future for diamond as a material for electronic devices. Pure diamond has a bandgap of $5.45\,eV$ and therefor is an insulator with a high specific resistance of more than $10^{16}\,\Omega cm$ [21]. Therefore there is a strong need to search for suitable dopants. The semi conducting properties of natural diamond were already discovered in 1952 [59]. The investigation proved that boron was responsible for the semiconductor behavior. This result also shows that for diamond (a group IV material like Si) group III elements can act as acceptors and group V elements as donors. It was further reported that diamond layers with elements from other groups of the periodic table had also semi conducting properties [60, 61]. However, the incorporation and the effect of these elements are still not clear yet.

But still, diamond doping with shallow donors and acceptors probably presents the biggest obstacle in diamond electronics due to the small size of the lattice, in which dopants are difficult to incorporate, leading to a distortion of the diamond lattice. The solution of this problem resides in introducing impurities with small atom size that can occupy an interstitial site, or the introduction of atoms comparable to carbon that can be incorporated in substitutional sites, thus minimizing the strain in the crystal. Moreover, the impurities should have an energy level close to the conduction band minimum for $n-$type or valence band maximum for $p-$type doping.

As already mentioned, the size limitation of the dopant atoms limits the choice to light atoms only, and the large bandgap and tight crystal structure of diamond makes doping of diamond even harder. The most suitable candidates for diamond doping are nitrogen and phosphorus for $n-$type doping, and boron for $p-$type doping. All three dopants are deep and none of them is fully activated at room temperature. The activation energy of N, P and B are $1.7\,eV$, $0,6\,eV$ and $0.37\,eV$ respectively (Figure 5.1). The activation energy of boron can be neglected at higher concentrations above $10^{20}\,cm^{-3}$, but at high concentration the carrier mobility degrades due to miniband conduction and high lattice stress. Growth experiments with carbon C_{13} were conducted in order to reduce the stress, but the influence was hardly noticeable with a slight improvement in mobility from ≈ 30 into $\approx 38\,cm^2/Vs$ both at concentrations of $6 \times 10^{19}\,cm^{-3}$.

Since no effective donor for diamond is known, the development of diamond electronics is focused on unipolar P-type devices such as $FETs$ and Schottky diodes.

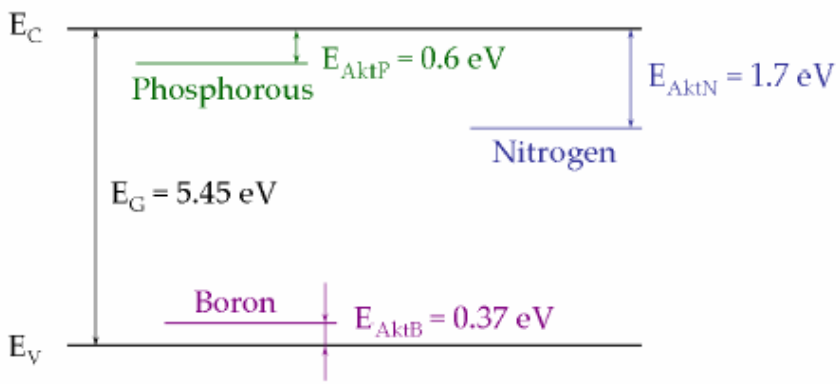


Fig. 5.1: Schematic doping configuration of phosphorous, nitrogen and boron doping in diamond.

The introduction of dopants can be achieved via several methods. A widely used method in the case of silicon is ion implantation of both $n-$type and $p-$type doping, but this technique is very complicated due to the metastable nature of diamond as shown in [62], where the bombardment converted the part of high concentration into graphite, leaving only the tail with $N_A < 10^{18}\,cm^{-3}$. Nevertheless, the first successful attempts to dope diamond, were realized by this method [63, 64]. The first diamond electronic devices were achieved by this method [63].

In addition, the hydrogen terminated diamond surface induces a $p-$type channel close to the surface. This $2DHG$-like channel is generated without external doping. In this method the origin of the acceptors in the channel is still under discussion. Oxygen terminated diamond on the other hand results in a highly insulating surface. On the other hand, $p-$type channels can be also created by boron $\delta-$ doping.

The most effective method for diamond doping is the in-situ doping during the epitaxial CVD growth. The effectiveness of this method is reflected in several aspects. For the most common dopant, boron, the doping concentration can be varied from $10^{16}\,cm^{-3}$ until to about $10^{21}\,cm^{-3}$. In addition, this method, compared to the ion implantation method, produces doped layers with significantly lower defect densities at higher concentration. Nevertheless, the growth of defect-free layers with higher concentration ($N > 10^{20}\,cm^{-3}$) is difficult due to the lattice distortion.

This doping method allowed the realization of devices using the delta profile technique, as well as n-doping by phosphorus. The dopant in this method (e.g. boron) can be introduced as a gas [65], liquid [66] or in the solid state [67, 68]. So, depending on the doping source, there are several possibilities to produce boron doped layers. The most widely used method is doping by adding Diboran (B_2H_6) [65]. An alternative doping gas is Trimethylborade ($B(CH_3)_3$ or TMB), which is not toxic as the case is with Diboran [69]. Another method is the insertion of solid boron into the CVD plasma, which has been adapted in this work. This approach is achieved by the insertion of one or more boron rods [68]. With these

possibilities of doping, highly doped layers can be produced, with a concentration up to $N_A > 10^{20}\,cm^{-3}$ [68] with low compensation levels. Using this method, Boron is etched from the rod by the hydrogen radicals and BH_x- complexes are produced which will transport the boron to the diamond surface, where the BH_x will be decomposed and the boron will be incorporated into the diamond surface.

5.1 N-Type Doping

The interest in $n-$type doped diamond has increased in the past years. Such $n-$doped layers may be used in bipolar devices, LEDs, cold cathode electron emitters, etc. As discussed earlier, the two promising candidates are phosphorus and nitrogen, where both have deep donor levels in diamond [70]. The shallower sulfur can be also used [71] but there are no reports so far about $n-$type conductivity of sulfur doped diamond [72]. It is very hard to incorporate impurities into single crystal diamond but it has been found that ultra nano crystalline diamond (UNCD) can be doped with nitrogen without noticeable activation energy [73]. But, it could also be that the grain boundaries are widened and the conduction is only graphitic. Unfortunately, UNCD is not suitable for high performance electronic applications but it still can find its use in biomedical [74] or high temperature applications [75].

5.1.1 Nitrogen

The thermal activation (ionization) is described by the following equation:

$$n = N_D \left(1 - \frac{1}{1 + \frac{exp\left(\frac{E_D - E_F}{KT}\right)}{g_d}} \right) \tag{5.1}$$

where g_d is the degeneracy of the conduction band. Since the conduction band has one minimum and each state in the minimum has two different electron spins, then g_d equals to 2. In the bandgap of diamond, nitrogen can occupy different electrically active states with different activation energy levels, depending on its incorporation in the diamond lattice. At high concentration, the occupied sites in natural diamond are called $A-$sites and are an Aglomerate, in which two nitrogen atoms reside in two neighboring lattice sites. Substitutional nitrogen also exists and represents the usual form with which nitrogen is incorporated into the diamond crystal during CVD growth [76]. Type Ib diamond, can be doped with substitutional nitrogen in concentrations of about $10^{18}\,cm^{-3}$ but with no reduction of the activation energy with increased concentration. The activation energy of substitutional nitrogen is about $1.7\,eV$ below the conduction band [77]. This high activation energy causes an insulating behavior of nitrogen doped diamond at room temperature and possesses the electrical property of a lossy dielectric. The analysis of the conductivity in nitrogen doped layers [78] proved that defects play the main conduction role in those layers.

Nevertheless, it has been reported that nitrogen increases the diamond growth rate [79] and enhances field emission [80] and despite its relatively deep level, it can compensate the acceptor states existing in a $p-$type doped layers as in surface channels generated by H-termination [81, 82].

UNCD is composed of diamond crystallites $2 - 10\,nm$ in diameter with a large number of grain boundaries. These grain boundaries are composed mainly of disordered carbon with mixture of sp^2 and sp^3 bonds. Nitrogen is incorporated in the grain boundaries and new electronic states are created in the diamond band gap [83]. Nitrogen as a substitutional donor is not required in this case. Increasing the concentration of nitrogen in the grain boundary makes the semi-metallic behavior of diamond more noticeable. Moreover, the increment of the grain size with incorporating more nitrogen creates additional conduction pathways [84]. Incorporated nitrogen induces shallow donor levels, where the density of these shallow donors increases with increasing concentration of nitrogen. MPCVD films in argon rich plasma with $10\,\%$ nitrogen exhibit a shallow peak level with an activation energy of $0.05\,eV$ [85]. The grain boundaries are again responsible for the high conduction, which are the highest $n-$type conductivity reported so far. This material has been used in combination with boron doped diamond to fabricated high temperature, stable, $pn-$junctions [75, 86].

Practically, for this study, nitrogen $N-$doping is of interest only as a cap layer above an active channel delta profile, usually under the gate contact, resulting in a lossy dielectric $P - N$ junction. Nitrogen itself has a solubility limit in diamond of around $10^{18}\,cm^{-3}$. Thus, its incorporation is self limited below a level where miniband formation would occur. The growth rates with nitrogen are usually very high and can reach up to three times the intrinsic growth rate.

To find out, whether nitrogen was incorporated into the CVD layers (and if yes, how much), cathodoluminescence measurements with an acceleration voltage of $5\,kV$ were performed by the Semiconductor Physics Group (Prof. Sauer) at Ulm University on 5 samples grown with different nitrogen concentrations in methane (Figure 5.2). The temperature of the measurement was $\approx 8^{\circ}\,K$.

All four samples were grown at the same temperature of $700^{\circ}\,C$, pressure of $30\,Torr$ and microwave power of $750\,W$, with:

- sample 1 has been grown with a nitrogen to methane ratio of $8/1$,
- sample 4 with $4/1$,
- sample 2 with $2/1$
- sample 3 with $1/1$.
- sample B without nitrogen.

The spectra of all samples show characteristic lines related to nitrogen at $2.463\,eV$ and $2.156\,eV$. They are not due to pure nitrogen incorporated into the diamond matrix but are rather created from different complexes, where nitrogen plays a role. This fact shows, that

nitrogen was indeed incorporated into the samples, but the electrical active deep donor part could not be determined quantitatively.

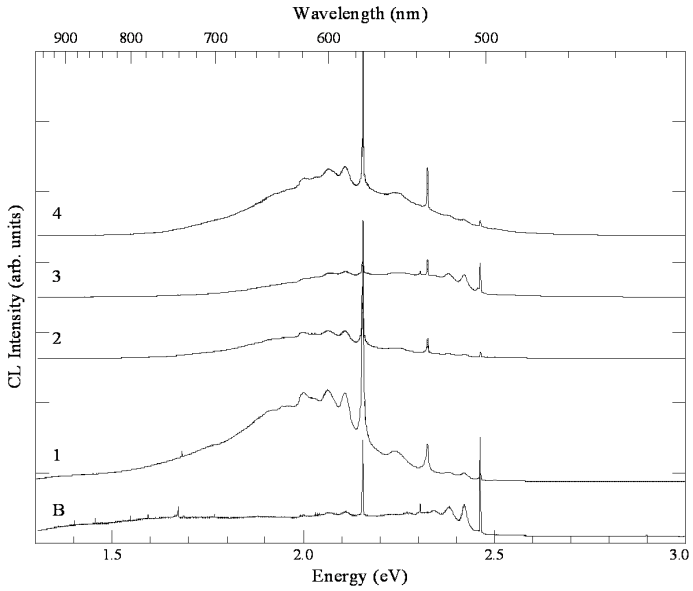


Fig. 5.2: Cathodoluminescence spectra of 5 nitrogen doped thick layers with different nitrogen to methane concentrations. (measured by G. Prince, Semiconductor Physics Department, Ulm University.)

The ratio between the intensities of the two lines, namely at $2.463\,eV$ and $2.156\,eV$ were compared to a reference sample B, without nitrogen. From this comparison, it was possible to determine a trend that allowed to check in which of the grown layers the nitrogen concentration was higher.

From the calculated intensity ratios, sample 1 seems to have the highest concentration of nitrogen. Second is sample 4, third is sample number 2 and the lowest concentration of nitrogen is in layer 3. This comparison of the different ratios is valid because in reference to sample B, the line at $2.463\,eV$ is the strongest, while for the nitrogen grown layers the center at $2.156\,eV$ dominates.

This result is in good agreement with the growth conditions:

Although the tendency of nitrogen incorporation during growth is not likely to be linear with the concentration in the gas phase, the tendency of higher incorporation with higher nitrogen gas is clearly observed.

5.1.2 Phosphorous

Phosphorus is a shallow dopant compared to nitrogen with an energy level of almost $0.58\,eV$ below the conduction band minimum [87]. The solubility of phosphorus in diamond com-

plicates its incorporation into the diamond lattice, preventing it from being the most suitable $n-$type dopant of diamond.

Phosphorus can be relatively well incorporated into (111) oriented diamond using phosphine (PH_3) as a dopant gas source [88, 89, 90] which is, like Diboran, a toxic substance. The disadvantage here is the difficulty of polishing the (111) oriented surface, where the substrate is extremely limited in size and very expensive. Recently, phosphorus could be incorporated successfully into (001) oriented diamond films [87, 91]. The electrical properties, such as mobility and sheet resistance, are comparable to values reported for (111) orientation, but they are still significantly lower than that of boron doped diamond films.

5.2 P-Type Diamond

P-type diamond can be realized by either, doping with boron, or, by the influence of hydrogen termination. Because of those two available conductivity mechanisms, there are basically two approaches to manufacture diamond based FETs. The first approach relies on a hydrogen termination induced channel. The other relies on a boron delta doped channel.

5.2.1 Hydrogen terminated diamond surface

A diamond layer with a hydrogen terminated surface induces a $p-$type conductive channel with high carrier density [92, 93] and vanishing activation energy of the charge carriers [94]. These channels are induced underneath the surface without the addition of dopants and are created by the plasma hydrogen treatment, especially during growth process [95]. Accordingly, these channels are used to develop FETs with full activation energy at room temperature. The conductive channel itself seems to include an extension of few atomic layers only. The reason for the induction of this surface conductive channel with low activation energy and high carrier concentration is still not fully understood. Due to the low density of diamond surface states [96] the Schottky contact barrier height on the H-terminated diamond depends strongly on the metal work function [92, 97].

Within the Schottky limit (density of surface states is negligible) [98], the Schottky barrier height Φ_B is determined by the difference in the metal work function and the electron affinity of the semiconductor.

$$\Phi_B = E_G + \chi - \Phi_M \tag{5.2}$$

So, different metals need to be used to fabricate Ohmic and Schottky contacts on hydrogen terminated surface. On the other hand, oxygen termination of diamond surface completely suppresses the conductive channel and the surface is highly insulating. This allows the production of diamond simple logic circuits, as was demonstrated in [99]. These properties of the diamond surface were also used for fabrication of MESFETs [100, 101, 102, 103,

104, 105, 106], MISFETs [107, 108, 109, 110] and FET structures in contact with liquids [111, 112, 113].

The origin of the H-induced channel is still under discussion, but there are two models that attempt to explain the effect:

1. A model for shallow acceptors due to incorporation of hydrogen in a sub-surface region of $H-$terminated diamond. This assumption was based on the observation of noticeable diffusion of hydrogen into the diamond near-surface region after hydrogen plasma treatment [4, 93]. This model is accompanied with a strong dependence of the surface conductivity on the chemical environment and atmospheric conditions.
2. The second model associates the acceptors to surface adsorbates with sufficiently large electron affinity so that the holes can be induced in the valence band of diamond via charge transfer [114, 115]. The first implication of this model is that the $p-$type channel is located directly at the diamond surface [116]. But this conclusion contradicts with the ability to realize Schottky diodes with various metals since such a configuration will lead to a strong tunneling current between the H-terminated diamond and the metal contact, regardless of the metal work function difference.

Thus, it was proposed that the hydrogen induced channel is separated from the diamond surface by few nanometer thick dielectric layer as depicted in Figure 5.3.This layer allows the complete depletion of the hydrogen induced channel by a Schottky contact, but prevents the tunneling through the barrier at forward biases.

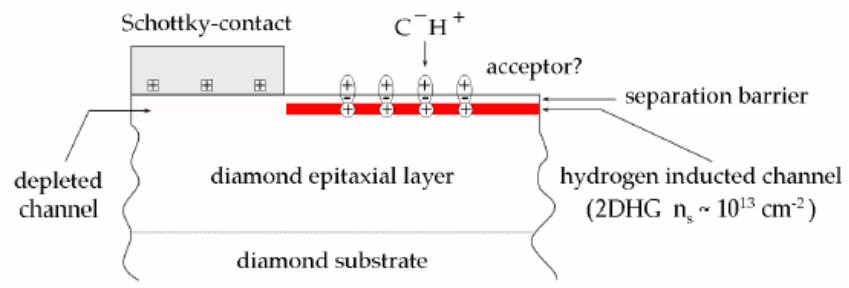


Fig. 5.3: Hydrogen induced $p-$type channel. The origin of the acceptors is still unclear [4].

5.2.2 Bulk Doping with Boron

Boron is the only technically used acceptor in diamond doping. The activation energy of boron is $0.37\,eV$ which results in a partial activation at room temperature. If the doping level of boron is high enough, a miniband will form and start to overlap with the valence band thus lowering the activation energy and enabling tunneling contacts.

Boron is the only acceptor in the case of uncompensated boron doping, without donor like defects or other unwanted donors ($e.g.$ nitrogen). Under the assumption $n_i << N_A, N_D$,

the uncompensated case for diamond doping can be achieved in a wide range of temperatures. Therefore, $p = N_A^-$, or:

$$p = N_A^- = N_A \left(\frac{1}{1 + g_a exp\left(\frac{E_A - E_F}{KT}\right)} \right) \tag{5.3}$$

Here E_A is the activation energy of the acceptor, N_A is the acceptor concentration and N_A^- is the density of ionized acceptors that makes conduction in the valence band. The degeneracy factor in Equation 5.3 $g_a \equiv 1/g_d$ indicates how many times each state of the valence band can be filled. After Collins [117], $g = 4$ should be used for diamond since the valence band maximum has a two fold degeneracy. Taking also the influence of split-off bands into account, particularly, if the thermal energies are well above $6\,meV$, one may consider $g_a = 6$. In the case, where only a part of the traps is ionized, the holes concentration and Fermi level in uncompensated boron doped diamond can be written as [118]:

$$P = \sqrt{\frac{N_V N_A}{g_a}}.exp\left(-\frac{E_A}{2KT}\right) \tag{5.4}$$

$$E_F = \frac{E_A + E_V}{2} - \frac{KT}{2} ln\left(\frac{N_A}{g_a N_V}\right) \tag{5.5}$$

Equation 5.5 shows that the concentration of holes lies at half of the activation energy of the impurity. It depends linearly on the temperature (neglecting the temperature dependence of N_V). In reality, uncompensated boron doped diamond is difficult to realize because defects in diamond act in general electronically as deep donor traps that also compensate p-doping. But diamond layers with very low compensation levels ($0.4\,\%$) can be produced for (100) oriented crystals, with very slow growth rates, or with Step-flow growth [119].

The compensation level for boron is the ratio of a residual donor concentration and the boron acceptors concentration: $K = N_D/N_A$. Usually, a partially compensated film has an effective doping of $N_A - N_D$.

In the case of a partial ionization of the acceptor level like in the case of boron, the concentration of holes is:

$$P = \frac{(N_A - N_D)N_V}{g_a N_D} exp\left(-\frac{E_A}{KT}\right), \tag{5.6}$$

where both N_A and N_D are deep acceptors and donors respectively.

Chapter 6

Diamond δ -Doping

Even though diamond has extraordinary electronic properties, devices still suffer from lack of shallow donor and acceptor doping [120, 121, 6]. Boron can only be fully activated at high concentration above $10^{20}\,cm^{-3}$. However the maximum sheet charge density in the FET channel, which can be adjusted before electrical breakdown of diamond occurs, is about $4 \times 10^{13}\,cm^{-3}$ [6]. This constraint caused the development of the concept of delta-doping. Ideally, the delta profile is composed of a monolayer of boron acceptors embedded into the diamond matrix, in addition, free carrier diffusion into the adjacent undoped areas causes high carrier mobility due to reduced scattering at the ionized acceptors [22]. But the high peak concentration may lead to high intrinsic stress, defect formation, acceptor passivation and compensation. In 1995 the first delta doping profiles in diamond were accomplished [122], their advantage and characteristics have been discussed in the literature by a number of authors since then [6, 123, 124, 125]. Because of their potential high carrier mobility in comparison to uniformly highly doped layers, stacks of delta-profiles have been investigated too [6, 126]. This concept has for instance been applied in the design of vertical diode structures for the backside contact, also reducing the stress, generated by the high boron concentration, with the substrate and top layer. While nm-steep profiles were mentioned in 1997 [68], it had been difficult to correlate the chemical/physical profiles with the electrical free carrier profiles. As the chemical/physical methods were in general destructive like SIMS [127] or elastic recoil detection (ERD) [128], a correlation on the identical sample was impossible. On the other hand, the electrical analysis had mostly been performed by Hall and van der Pauw measurements, limited to the analysis of the sheet charge without depth resolution due to the lack of Schottky barrier profiling or a uniform etching technology (of the Hall and van der Pauw patterns) with a resolution of well below $1\,nm/step$. Steep delta-profiles are essential, because high carrier mobilities in the channel require a steepness smaller than the Debye length

$$L_D = (\epsilon kT/q^2 N_A)^{1/2} \tag{6.1}$$

where N_A is peak doping concentration. For a concentration of $10^{20}\,cm^{-3}$, the value of L_D is only $0.3\,nm$. This work successfully diagnosed a correlation of the chemical profiles with their free hole carrier profile by electrochemical characterization of the diamond-electrolyte interface, as will be explained in more details in Chapter 6.1.

In a similar approach as described in [68], the δ-doped layers here was deposited from a solid boron source (boron rod, in Figure 6.1) onto an undoped diamond buffer. This delta growth step consists of a specific sequence of gas flow pulses controlled and timed by mass flow controllers and computerized valves and monitored by a quadrupole mass spectrometer. This phase was characterized by growth interrupts as well as the rapid insertion of the boron rod into the plasma for a short period of time, as will be discussed in details in section 6.3. At this stage the insertion of the boron rod was still controlled manually. The delta profile had been overgrown by a nominally undoped cap layer in all cases.

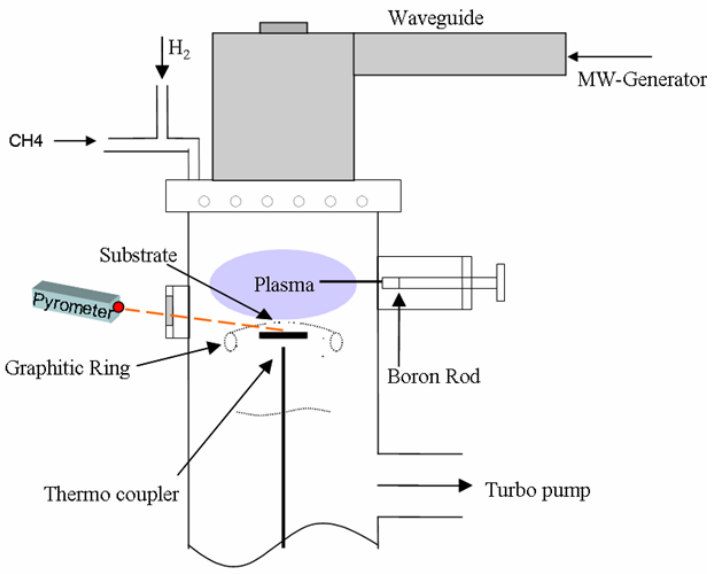


Fig. 6.1: Simplified schematic of the MWPCVD machine used in the $\delta-$doping process. To be noticed is the solid boron source introduced in the plasma ball.

The formation of the surface morphology with following growth steps was monitored by AFM for the case of single delta profiles and delta profile stacks. The initial smoothness of the buffer layer surface of $0.3\,nm$ could be maintained on a $10 \times 10\,\mu m^2$ surface area (see Figure 7.12) even after growth of a stack of 4 delta profiles with a total thickness of $25\,nm$ (see Figure 7.15). This result indicates that the growth process is $2-$dimensional not initiating $3D-$growth. Furthermore, it can be stated that the thin boron doped layer is free of boron clusters, which would cause $3D-$growth of the following layer. Cluster formation can be attributed to several sources. First of all, it may be the solid boron source, which is inserted into the plasma and where clusters may then be sputtered off from the surface of the rod. Secondly, clusters could be expected, when the precursor molecules are insufficiently cracked at the surface but still stick. Finally, cluster formation can occur when the concentration is in the $10^{21}\,1/cm^3$ range, where the critical thickness for stress relaxation is approached or the solubility limit is reached.

As discussed above, Schottky barrier diodes cannot be used to profile free carrier delta profiles, because tunneling between the metal and the highly doped delta peak causes high leakage. An alternative would be capacitance-voltage $(C-V)$ measurements of the delta-doped diamond substrate in direct contact with an electrolyte solution. In this method, the depletion layer capacitance needs to be extracted from the impedance characteristics of the diamond-electrolyte interface [129]. For the case of a chemically inert surface, neither etching nor surface corrosion will occur. This non-destructive technique has already been applied to homogeneously highly boron-doped diamond electrodes [129, 130]. In this study, the extracted carrier profiles had been correlated with the boron doping concentration measured by Hall-effect.

6.1 Electrochemical profiling of boron-delta-doped layers

The carrier profile in a single delta-doped layer was assessed from the impedance characteristics of the delta-doped electrode structure in aqueous solution. The delta-doped electrode structure was grown according to the growth parameters as for the profile shown in Figure 7.14. The opening in adhesive Teflon foil defined the electrode area in contact with the electrolyte, which measured $1\,mm$ in diameter. All electrochemical experiments were performed in a standard three-electrode glass cell in $0.1\,MH_2SO_4$. A $PARSTAT2273$ potentiostat (Princeton Applied Research) was utilized for the cyclic voltametry and the electrochemical impedance measurements. The impedance characteristics were recorded in the frequency range from $0.1\,Hz$ to $10\,kHz$ and fitted using $ZSimWin$ software. All measurements were conducted in a grounded Faraday cage with the solution de-aerated by bubbling with nitrogen gas. The surface of the electrode sample was subjected to wet chemical oxidation in $H_2SO_4 : H_2O_2\ (2:1)$ electrolyte before the electrochemical tests. The fact that $O-$termination induces a high density of carbon-oxygen functional groups on the diamond surface is well documented [131]. The $O-$related surface groups are mainly responsible for the pH sensitivity of the junction surface potential [7] and for the electrical double layer formed on the $O-$terminated surface in the electrolyte [129, 132]. Figure 6.2 shows two $RC-$elements in series, which may represent the equivalent circuit of the diamond-electrolyte interface, as a first-order approximation. One of them describes the depletion layer in the boron-doped diamond layer (C_{SC}, R_{SC}), while the other $RC-$element is related to the electrical double layer (C_{dl}, R_{dl}) in the solution. However, this circuit could be applied only for semiconductor electrodes showing no electrochemical activity in electrolytes without redox pairs and polarized in the potential range between the hydrogen- and oxygen-evolution reactions [130].

Thus, as indicated above, the electrochemical activity of the delta-doped electrode and the potential window were examined by cyclic voltametry in $0.1\,MH_2SO_4$ (Figure 6.2). Inside the potential window, no traces of adsorption reactions were found. There was a negligibly small activity of the surface, as indicated by the background current, which was about $0.2\,\mu A/cm^2$. The potential window of water electrolysis was about $3\,V$ measured in the μA current range. As the AFM scan in Figure 7.12 depicts, the low activity and the large

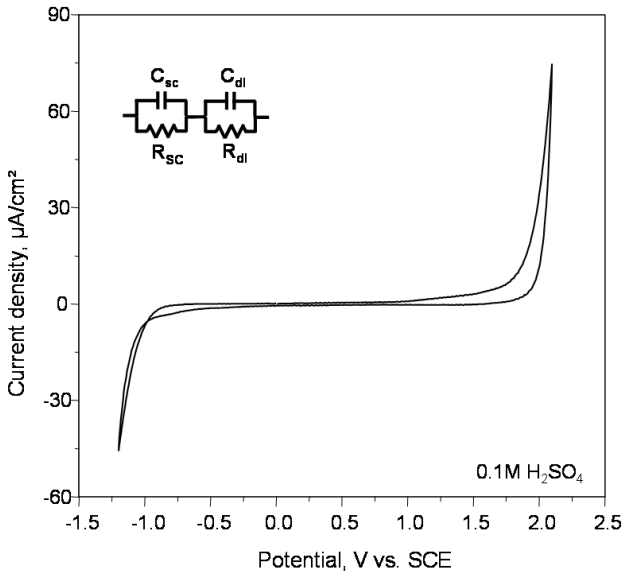


Fig. 6.2: Linear cyclic voltametry scan of boron delta-doped layer on the surface of (100)-oriented diamond substrate in $0.1\,MH_2SO_4$ electrolyte. The scan rate was $50\,mV/s$, as shown later on in Figure 8.9 a).

potential window resulted from the high quality of the grown surface [133]. The diamond-electrolyte interface can indeed be described by two $RC-$elements in series. One capacitance of the circuit insert in Figure 6.2 was in the range of 2 to $4\,\mu F/cm^2$ and was strongly bias-dependent. The second capacitance was nearly constant and could be prescribed to the electrical double layer. Its value was estimated to about $10\,\mu F/cm^2$, which was very close to the value of the double-layer capacitance extracted from the analysis of redox reactions on homogeneously-doped and $O-$terminated diamond electrodes [129] [132]. The high inertness of the electrode surface was furthermore confirmed by the resistances R_{SC} and R_{dl} which were above $1\,Mohm \times cm^2$, shown in Figure 6.2 insert. During the calculation of the semiconductor doping profile, the double layer capacitance of $10\,\mu F/cm^2$ was taken into account. Figure 6.3 illustrates the carrier profile evaluated from the corresponding $C-V$ plot.

Two independent $C-V$ measurements were performed at $0.6\,kHz$ and $1.0\,kHz$ frequencies. Both measurements yield an almost identical profile, indeed indicating a valid correction by a constant double layer capacitance. Figure 6.3 shows that the value of the maximum free carrier concentration was about $1 \times 10^{21}\,1/cm^3$, which approximates the peak concentration of the chemical boron concentration extracted by ERD in Figure 7.14. This high value also implies, that boron is indeed incorporated on lattice site at this high concentration and activated. The total charge density in the profile was about $4 \times 10^{13}\,1/cm^2$ and is again comparable to the ones extracted from the ERD profiles of similar samples, which indicates a low degree of defect compensation, clustering or hydrogen passivation as well.

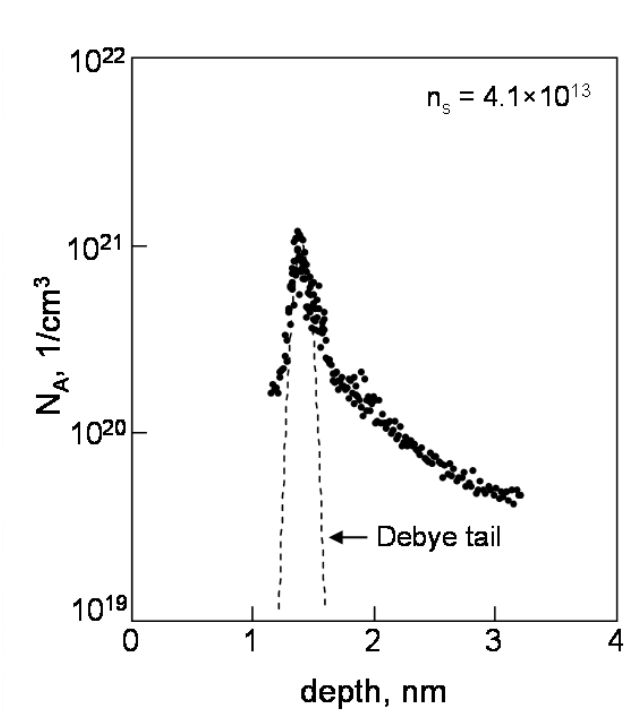


Fig. 6.3: The acceptor profile of a single boron delta-doped layer extracted from capacitance-voltage characteristics of the diamond-electrolyte junction in $0.1\,MH_2SO_4$ at $1.0\,kHz$ oscillation frequency. The dashed curve shows the Gaussian profile calculated for the Debye length, corresponding to the peak concentration of $10^{21}\,1/cm^3$ electrolyte.

In theory, the resolution of the free carrier profile is limited by the Debye-tail as mentioned above. Figure 6.3 presents the tail for a Gaussian profile according to:

$$y(x) = A.exp\left[-(x - x_0)^2/\sigma^2\right] \tag{6.2}$$

where x_0 is the mean value (in this case $1.3\,nm$), σ is the standard deviation (in this case $0.1\,nm$), resulting in a Debye length with a peak concentration A of $10^{21}\,1/cm^3$. As can be seen, the profile coincides the peak of the theoretical profile. This result suggests that the chemical profile at concentrations above $5 \times 10^{20}\,1/cm^3$ may still be steeper. However, at concentrations below $10^{20}\,1/cm^3$, a noticeable tail in depth was observed, which was not present in the ERD profiles in Figure 7.14. This issue is still being investigated.

Because the chemical/physical profiling methods used in the past had been in general destructive, a correlation with a free carrier profile on the identical sample was impossible. The electrical analysis on the other hand had mostly been performed by Hall and van der Pauw measurements. However, these measurements are limited to the analysis of the sheet

charge without depth resolution due to the lack of Schottky barrier profiling or a uniform etching technology (of the Hall and van der Pauw patterns) with a resolution of well below $1\,nm/step$. Therefore the question of doping activation at degenerately high concentrations remained unanswered. But now the $C-V$ profiling in electrolyte allows to determine the surface near part of delta-profiles with sub-nm resolution. Moreover, the technique is non-destructive. In other words, ERD profiles can now be compared with free carrier profiles, which can then be used in the optimization of FET structures as well. Both the ERD and SIMS analysis had indicated the chemical incorporation of boron with high peak concentration. Nevertheless, an investigation into electrical activation, $H-$passivation or acceptor passivation by $B-$dimer formation could not be performed without electrochemical profiling. The ERD analysis had also denoted that carrier profiles close to the Debye-limit should be measured, if full activation is reached. Electrochemical profiling did indeed reveal high active peak carrier concentrations close to $10^{20}\,1/cm^3$ and steep gradients in the order of the Debye tail. At the same time, the electrochemical profiling could be employed as a tool to optimize such profiles for use in FET structures as well. The first example had been an ISFET operating in the linear regime, for application under highly corrosive conditions [134].

6.2 Requirements and conditions

The diamond FET structure with full activation of an extrinsically doped channel at room temperature has a quasi two dimensional boron doped channel layer, where the doping ideally is a single monolayer with a concentration exceeding $10^{20}\,cm^{-3}$ and above this concentration, the boron acceptors are fully activated, which may provide the desired sheet carrier concentration of $n_s \approx 2\times10^{13}\,cm^{-2}$ in the channel (see chapter 7), limited by the breakdown strength of diamond. Basically, the performance of the device will be very similar to that of a MISFET or HEMT.

In effect, the thickness of the delta channel can reach up to several nanometers. Figure 6.4 displays a sketch of a delta doping profile and the Debye tail of free carriers diffusing out to both sides. The mobility of carrier scattering directly increases when the density of scattering centers i.e. the doping impurities will be low (approx. $10\,cm^2/Vs$ in the case of uniform doping of $5\times10^{20}\,cm^{-3}$). The mobility of carriers outside the doping spike will increase with distance depending on the scattering distances. Far from the spike they will reach the mobility of the intrinsic material which may be as high as $3800\,cm^2/Vs$, depending on the substrate and buffer layer material used. An effective mobility of approx. $200\,cm^2/Vs$ can be expected if all scattering mechanisms and reasonable scattering rates are taken into account [6]. (Figure 6.3)

In order to ensure a high effective carrier mobility, the delta profile should thus have tails steeper than the Debye tail and the intrinsic diamond material surrounding the delta layer should have a very low dislocation, defect and trap density. Furthermore, the ionic radius of boron is essentially larger than that of carbon, inducing mismatch and stress at high concentrations, which should however not cause the formation of dislocations and clustering.

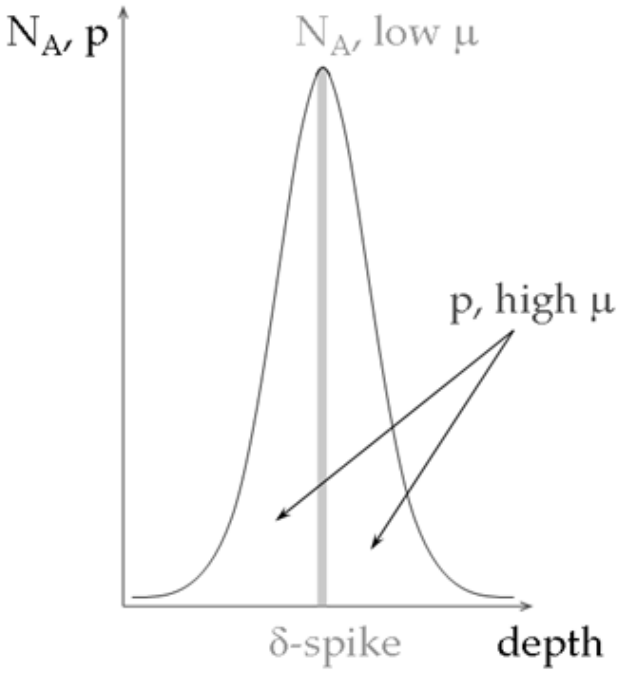


Fig. 6.4: A depth profile of a delta doped layer showing the doping profile along with the actual carrier profile.

When the carriers in the device are operated in saturation they will experience a high lateral field in the gate/drain drift region and will reach saturated velocity. Here they will move with high kinetic energy and their path will be basically two dimensional. Because of this high kinetic energy, phonon scattering will dominate and the saturated velocity will depend only marginally on the doping concentration. As a result, high mobility is important for two factors: it reduces the source series resistance and it allows velocity saturation to dominate already at moderate gate lengths.

6.3 Growth Procedure

At the moment, the group in Ulm seems to be the only diamond group, which has reported the use of a solid source of Boron for delta doping. Conventional procedures use gas sources like diborane (highly toxic) or trimethylborate. The filling and emptying of the chamber with the doping gas however, introduces time constants, during which growth has to be interrupted strictly. This was the main reason for the idea of introducing a solid Boron rod inside the plasma ball for a short period of time only, where the boron wire could be etched and BH_x-species released to the plasma, which are then split and boron is incorporated into the growth surface. This method is fast and prevents the time delay problem of a gas source supply. But still, the issue of background contamination with Boron during intrinsic

growth before and after the spike remains. However, growth interrupts are feasible and not detrimental to the surface smoothness.

The Scheme in Figure 6.5 illustrates how this problem affects the growth cycle used in the fabrication of the double delta design for the transistor.

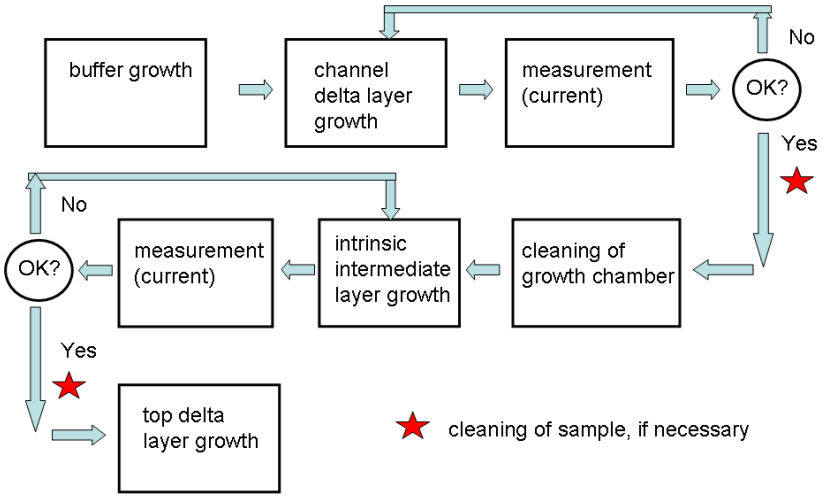


Fig. 6.5: Typical epitaxial cycle of the growth used for the fabrication of a double delta transistor design.

It is of extreme importance, that the intrinsic layer in between the upper contact layer and the lower delta channel is as clean as possible, since it is the same layer onto which the Schottky contact metalization of the gate is applied later. This fact calls for a growth interruption and a cleaning of the chamber before the separation layer is grown. This rather time consuming approach, could be improved by switching between two growth chambers.

The challenge concerning the delta layer growth had been to obtain a peak concentration between $1 \times 10^{20}\, cm^{-3}$ and approx. $5 \times 10^{20}\, cm^{-3}$. Otherwise the sheet charge density would have easily exceeded $3 \times 10^{13}\, cm^{-2}$ as needed for pinch off before breakdown occurs. In the past, steep delta profiles had been realized, which have however rarely allowed full pinch-off of the FET. It was especially noticed that there was no self-limitation in boron incorporation as expected from a solubility limit. One important parameter responsible for boron inclusion in the diamond crystal is the growth rate. By reducing the methane concentration at this step, we have been able to decrease the growth rate and reduce the boron incorporation at the same time, while keeping the thickness of the delta layer constant, and thus bringing the sheet charge density into the window needed for FET channels. Of course the contact layer could be realized with a higher sheet charge density.

Other experiments to bring the sheet charge density into the window have been:

1. to shorten the time of the boron rod inside the plasma,
2. to grow the delta layer after the boron rod is already removed.

These procedures are very demanding because they require stringent conditions for the timing of the process. As the boron background inside the chamber decreases very fast after the rod is taken out. Both approaches are not considered to be $100\,\%$ reproducable. Thus, determining the optimum timing has been quite challenging.

Apart from this issue, this delta growth step had been automated as much as possible. As shown earlier in this chapter, the integration of steps is realized by a specific sequence of gas flow pulses controlled and timed by mass flow controllers and computerized valves and monitored by a quadrupole mass spectrometer. $100-$oriented, polished HTHP single crystal type Ib substrates with a surface roughness less than $2\,nm$ (rms) were typically used (Table 6.1) The epitaxy on these substrates was performed in the modified and experimental Astex 1500 MPCVD apparatus mentioned earlier in Figure 6.1. Prior to epitaxy, a pre-growth H-plasma surface treatment has been applied, resulting in a surface roughness of $\approx 0.6\,nm$ (rms). For the details of the H-treatment parameters, please refer to Appendix A. Next, a $200\,nm$ thick nominally undoped buffer layer with a residual boron concentration in the range of $5 \times 10^{17}\,cm^{-2}$ was grown at a very low growth rate of $75\,nm/hour$, decreasing the surface roughness further down to $\approx 0.3\,nm$.(Table 6.1)

Tab. 6.1: Preparation steps proceeding the growth of the delta layer.

Step name	Time	Hydrogen H_2	Methane CH_4	Boron Rod
Cleaning Process	(Appendix A)			
AFM characterization	$\approx 2\,nm$ rms			
Hydrogen smoothening	$25\,min$	+	-	-
AFM characterisation	$\approx 0.6\,nm$ rms			
Intrinsic buffer growth	$2.5\,hours$	$200\,SCCM$	$0.3\,SCCM$	-
AFM characterization	$\approx 0.3\,nm$ rms			

The overall growth parameters of the intrinsic buffer were:

- pressure = $2\,kPa$,
- temperature = $750°C$,
- RF power = $750\,W$
- hydrogen flow of $200\,sccm$
- various methane concentrations.

Onto this buffer, the δ-doped layer is than deposited from the solid boron source by moving the boron rod inside the plasma ball. In some cases, the delta profile had been overgrown by a nominally undoped cap layer (Table 6.2). It is noteworthy, that when the boron rod was inserted inside the plasma, it was impossible to identify any differences in the gas consistency by the attached high resolution mass spectrometer.

Tab. 6.2: Summary parameters for the growth process of the delta layer.

Step	Time	Hydrogen H_2	Methane CH_4	Boron Rod
1	$2\,min$	+	-	-
2	$3\,Sec$	+	-	+
3	$3\,Sec$	+	$7\,SCCM$ for $24\,Sec$	+
4	Plasma off, pump out chamber			
5	$90\,Sec$	+	-	-
6	Plasma off, pump out chamber			
7	$45\,Sec$	+	$3\,SCCM$	-

6.4 Conclusion on growth

A large part of this work was dedicated to investigate the following issues concerning the delta layer growth:

- Boron profiles and free carriers profiles
- Activation energy and maximum Boron concentration
- Surface smoothness
- Growth mechanism: is Boron incorporated or is it substitutional or compensated and not active?
- Carrier mobilities
- Are there any Boron clusters incorporated during growth?

In the following chapter, we will try to answer all these questions by results obtained from a number of electrical and physical/chemical measurements and from simulation.

Chapter 7

Characterization of Boron δ-Doped Layers for Electronics

This chapter addresses the characterization methods and measurement techniques, which were utilized for the delta layer profiles. The measurements are divided into electrical characterization and chemical/physical characterization as follows:

Electrical measurements include:

- Photoluminescence
- Sheet resistance
- Capacitance-Voltage Measurement

Physical/chemical measurements include:

- Scanning Tunneling Microscopy STM)
- Atomic Force Microscopy (AFM)
- Secondary Ion Mass Spectrometry (SIMS)
- Elastic Recoil Detection (ERD)

7.1 Photoluminescence

As a first step, photoluminescence characterization was conducted on the delta doped layers, in a trial to identify the boron incorporation. Figure 7.1 shows four photoluminescence spectra of the thin delta layers which were observed as a first characterization effort. A weak signal correlated to boron was detected although there was a high penetration depth of the photoluminescence signal, which can reach a minimum of approx $70\,nm$ at low energy illumination, and very small thickness of the boron layer, compared to the penetration depth.Thus, this can not be related to any "quality" features of the profile, like introduced defect levels.

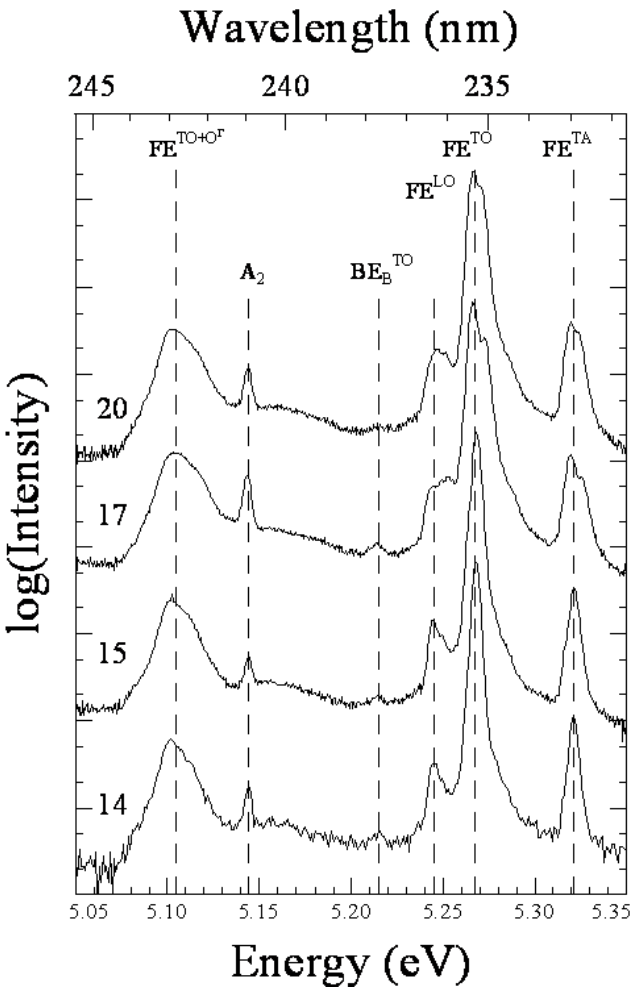


Fig. 7.1: 4 PL spectra of the delta layers showing a week boron related peak. (measured by G. Prince, Semiconductor Physics Department, Ulm University)

7.2 Sheet Resistance

Sheet resistance values on single delta profiles were extracted from TLM measurements. Ohmic contacts were either evaporated (Ni) or ion beam deposited ($W : Si$), as shown later in Chapter 8. TLM measurements were performed on test structures with 5 different channel lengths and values of the sheet resistances and the contact resistances were deduced. As an example, Figure 7.2 depicts the corresponding TLM measurement of a single delta layer. It is apparent that the specific contact resistance was in the range of $10^{-3}\,\Omega cm^2$. The sheet resistance was in the range of $2\,K\Omega_S$ and the transfer length amounted to $L_T = 2\,\mu m$.

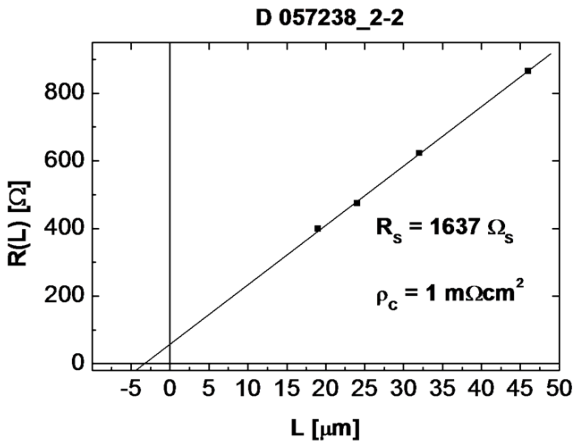


Fig. 7.2: A typical TLM measurement of a single delta layer.

7.3 Capacitance Voltage Measurement

It was very difficult to perform capacitance voltage scans on these delta profiles using metal Schottky gates, if the profile is not within the window needed for FET performance. But profiling with a liquid gate contact is possible, as discussed previously in chapter 6.1 since tunneling is suppressed by the junction to the liquid. However, the potential window for profiling is only approx. $3\,V$, which is the electrochemical potential window of a quasi-metallic diamond electrode.

This method was applied to the sharp delta profiles. A typical water dissociation window of $3\,V$ in diamond, measured on the surface of a delta profile with oxygen termination, is demonstrated in Figure 7.3.

While the current above $+2\,V$ in the anodic region (right hand side) corresponds to the oxygen evolution, the current below $-1\,V$ (referenced against SCE) in the cathodic region (left hand side) corresponds to the hydrogen evolution in water. The background current in the window stays in the nA-regime, which indicates also that the surface of the diamond film had a very low defect concentration. Usually, surface defects (or surface states) react with the solution via redox potentials and cause high background current levels, whereas the low background current allows a rather precise determination of the interface capacitance and therefore carrier profile.

The $C-V$ measurement within the dissociation window is displayed in Figure 7.4, which shows the carrier profile taken at two different frequencies. Two identical profiles strongly indicate that the equivalent circuit, used to extract the space charge layer capacitance in the diamond material, is correct and parasitics have also been taken into account correctly. (chapter 6.1)

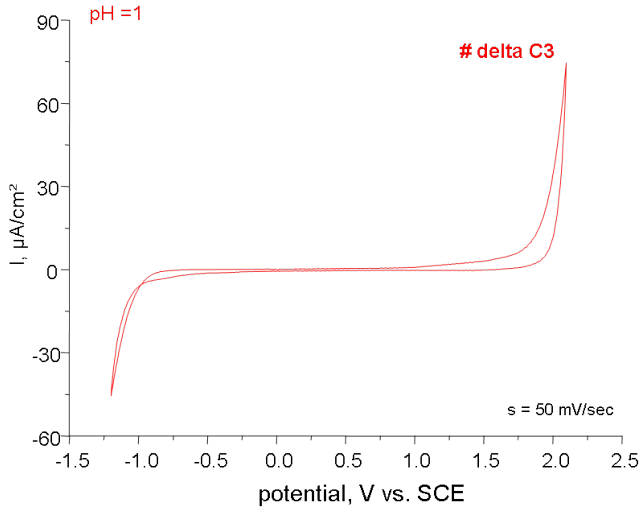


Fig. 7.3: A typical window of a cyclic voltametry measurement on single crystal diamond, showing a $3\,V$ water dissociation window. (Measured by A. Denisenko).

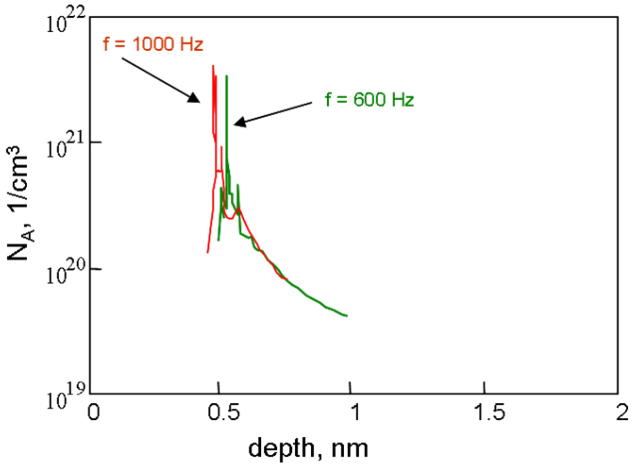


Fig. 7.4: Free carrier profiling $C-V$ measurement showing the independence of the measurement on the applied frequency. (Measured by A. Denisenko).

The free carrier profile possesses a high concentration reaching up to $10^{21}\,cm^{-3}$ along with a very sharp doping profile. It may then be compared with the physical/chemical profile obtained by ERD (see below), which attests that high boron concentration can be activated. It is astonishing that no deactivation limit below approx.$5 \times 10^{21}\,cm^{-3}$ can be recognized, since the analysis of thick quasi-metallic layers grown for super conducting experiments show B_2-formation and boron deactivation above $5 \times 10^{19}\,cm^{-3}$ [135]. When examining the ERD profiles discussed later, most of the chemically incorporated boron seems to be electrically active indeed.

In some special cases, a $C-V$ profile in air could also be taken with Schottky contacts, which were integrated in the transistor processing mask set. Such a $C-V$ profile with a peak concentration of $5 \times 10^{20}\, cm^{-3}$ is shown in Figure 7.5. Again the Debye tails are included for comparison.

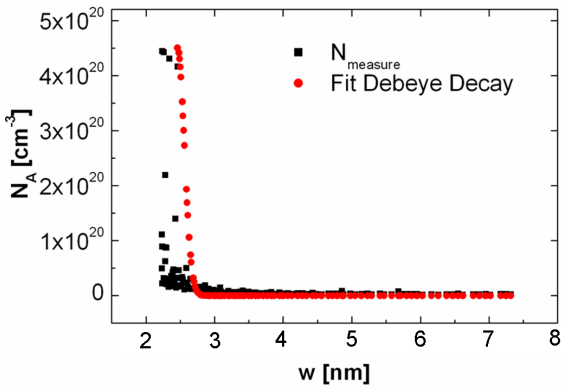


Fig. 7.5: Debye tails plotted along a $C-V$ measurement of a delta layer, matching very well to each other.

This measurement is the result of a delta layer located at $2\,nm$ below the surface, assuming $\epsilon_{diamond} = 5.7$. The measured profile is noisy but sharp. The Debye length indicated is $L_D = 0.143\,nm$.

7.4 Scanning Tunneling Microscopy (STM)

The way boron is incorporated in the diamond crystal is a crucial issue. B may be detached from the rod in the plasma by chemical reaction and kinetic bombardment. It is expected that $B - H_x$ radicals are created in the gas phase and adsorbed on the diamond surface. Either they can be split into atomic radicals and incorporated into the diamond lattice or they may combine to clusters and become overgrown as such when the methane is inserted into the growth chamber. Thirdly, it is even possible that boron is sputtered in clusters from the rod, while the clusters have no time to dissociate before they adsorb on the diamond surface, with the effect of buried clusters again.

Figure 7.6 describes how this problem was investigated: Scanning Tunneling Microscopy was conducted on the boron doped delta layers on a $10 \times 10\,nm^2$ area, to check the possibility of higher tunneling currents resulting from boron clusters. The buffer on this sample was grown under the same conditions as in table C.2 for smooth intrinsic diamond growth. On top of it, one delta layer was deposited following the recipe in chapter 5. The surface

of the buffer before and after the delta growth was unchanged. No irregularities pointing toward boron clusters on the diamond surface were identified, even though the resolution of the STM scan is at the atomic level. The Z range of this scan was $20\,A^{\circ}$ and the Z_{RMS} was $3.2\,A^{\circ}$. Other experiments concerning this issue will be shown in the next section.

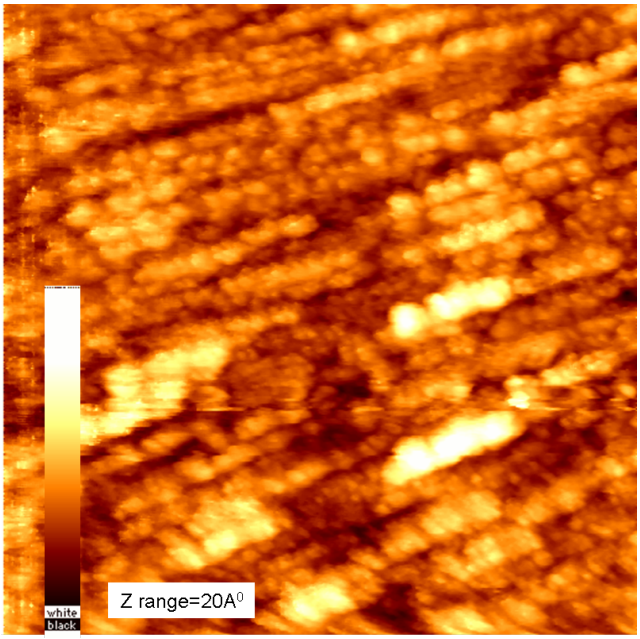


Fig. 7.6: STM scan of $10 \times 10\,nm^2$ area of a boron doped delta layer, where no boron clusters could be identified.

7.5 Buffer layer preparation and characterization: Atomic Force Microscopy

Before the beginning of the fabrication process, and after the cleaning of the samples, all substrates were characterized by AFM scans. It was noticed that there was a large difference in the surface morphology comparing the polished substrates without any growth, the CVD grown buffers and the delta profiles grown. This section will discuss these results in more details.

Figure 7.7 shows an AFM scan of a polished substrate without any CVD intrinsic buffer layer. Polishing stripes are very clearly seen and the RMS roughness value of this substrate is $\approx 1.9\,nm$, and the peak to peak roughness is about $8\,nm$.

On the other hand, Figure 7.8 illustrates an AFM image of another substrate polished with a new polishing technique (commercially available from $E6$). The difference between the old polishing and the new polishing technique was not revealed. But, this new technique showed a smoother surface with a peak to peak roughness of only $4\,nm$ and an RMS value

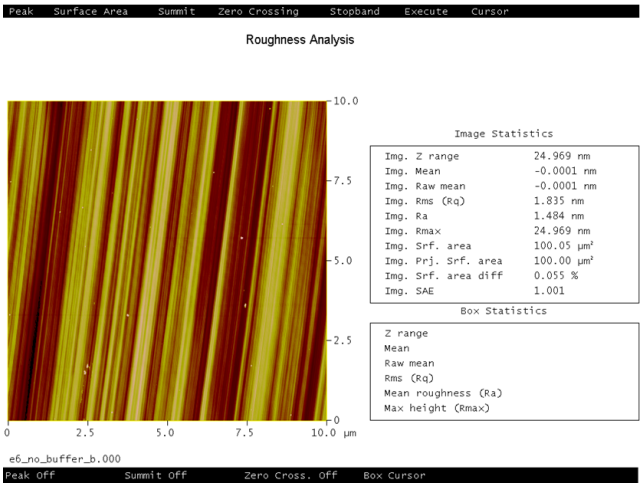


Fig. 7.7: AFM scan of a polished substrate without any CVD growth. Roughness $RMS = 1.9\,nm$ and peak to peak $8\,nm$

of $1.5\,nm$. The surface finishing difference between the two techniques is very obvious: While the old technique gave less but very deep polishing grooves (higher peak to peak roughness values), the new technique shows more grooves but they are very shallow now. This explains why the new polishing technique shows much lower peak to peak values but only a small improvement in the RMS roughness value. But still, these layer did not have the optimum surface for FET application.

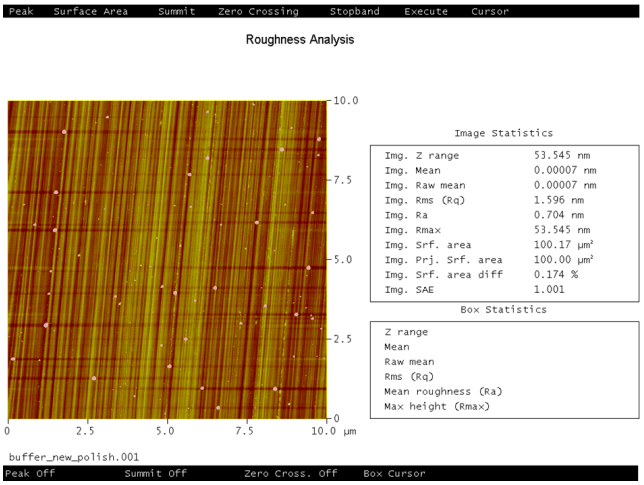


Fig. 7.8: AFM scan of a substrate without any CVD growth, polished using the new polishing technique. Roughness $RMS = 1.5\,nm$ and peak to peak $4\,nm$

In general, the CVD growth, if optimized with respect to the growth rate and gas concentrations, can improve the surface smoothness of the substrates. Figure 7.9 shows an AFM scan of a $100\,nm$ intrinsic CVD layer grown on top of a substrate polished with the old

technique. The difference between the overgrown substrate and the virgin substrates is very clear in terms of surface morphology. The overgrown substrate shows a granular surface on top of the polishing lines, increasing both the RMS value to $3\,nm$ and the peak to peak value to $11\,nm$. This granular surface is a typical consequence of a fast growth rate, which induces $3-$dimensional growth behavior. Obviously, the growth of a $1.0\,nm$ thin delta layer on top of such a surface will not be continuous along the surface. It will show discontinuities, which will be reflected as very low mobility and an overall low sheet charge density in the active layer. Doping tails will overlap with surface steps, resulting in an increased overall thermal activation energy of the sheet charge density.

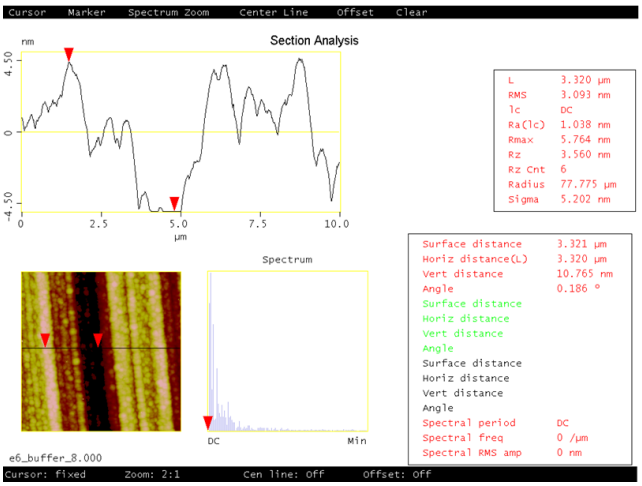


Fig. 7.9: AFM scan of a substrate with a $100\,nm$ CVD intrinsic layer on top of it; polished using the old polishing technique. $RMS = 3\,nm$ and peak to peak $11\,nm$

A number of investigations have been undertaken in order to improve the surface roughness before growth of the delta layer. One important parameter for improving the surface roughness is the growth rate. As already mentioned, very slow growth rates in the order of $75\,nm/min$ were typically used in order to grow a very smooth buffer layer underneath the delta. Figure 7.10 shows the effect of such a small growth rate on the surface smoothness. No granular surface was observed anymore. The figure illustrates a growth process undertaken in steps with growth interrupts. The growth was interrupted after 1 hour of growth and AFM scans were registered, which show in fact an improvement of the surface roughness after each growth step. It may be speculated that in the case of a slow growth rate the hydrogen radicals are able to etch SP^2 bonds at defects, higher growth steps and contours and to grow very $2-$dimensional in one planar direction, similar to step flow growth.

Figure 7.11 shows an AFM scan of a stack of 4 consecutive delta layers separated with nominally $6\,nm$ intrinsic spacer layers. The AFM scan shows a very smooth surface RMS roughness value of $0.3\,nm$ and a peak to peak separation of less than $1.0\,nm$. This result shows that the delta growth itself does not degrade the surface quality of the substrate, despite the large stress introduced with each boron doping spike. It also shows that in spite of the stacking of 4 delta profiles on top of each other, no $3D$-clusters of boron were

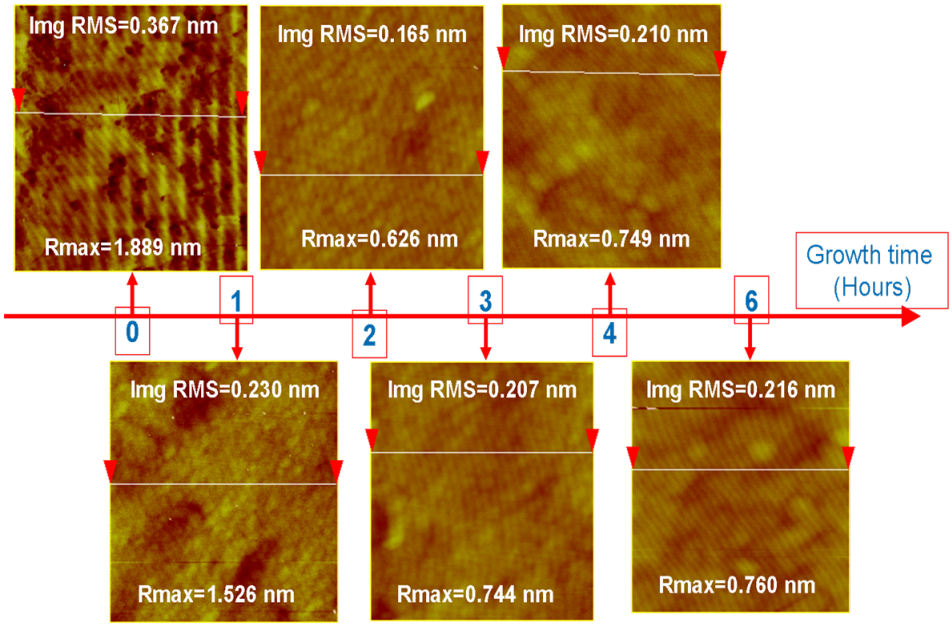


Fig. 7.10: AFM scans after each growth hour at very slow growth rate, showing the improvement in the surface roughness.

noticed in the surface roughness. This conclusion assumes that any boron clustering buried underneath surface would result in three dimensional growth and hence would have to be detected by AFM.

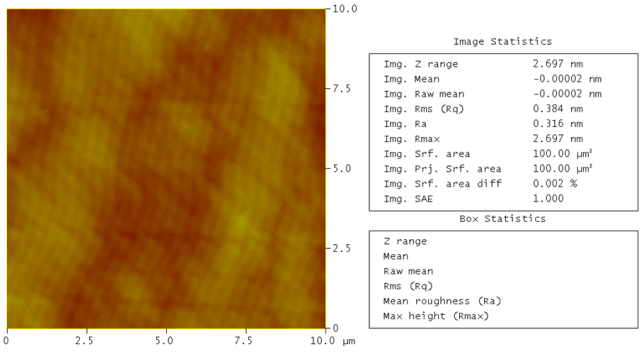


Fig. 7.11: AFM scan of a stack of 4 delta layers grown on top of each other. $RMS = 0.3\,nm$ and peak to peak is $\approx 1\,nm$.

For the device fabrication process mentioned later in Chapter 8, $100-$oriented, polished $HTHP$ single crystal type $1b$ substrates with a surface roughness less than $2\,nm\ rms$ were employed, as shown in Figure 7.12. A pre-growth $H-$plasma surface treatment had been applied, resulting in a surface roughness of $0.6\,nm\ (rms)$. A $200\,nm$ thick nominally

undoped buffer layer with a residual boron concentration in the range of $5 \times 10^{17}\ 1/cm^2$ was grown at a very low growth rate of $75\,nm/hour$, decreasing the surface roughness further down to $0.3\,nm$.

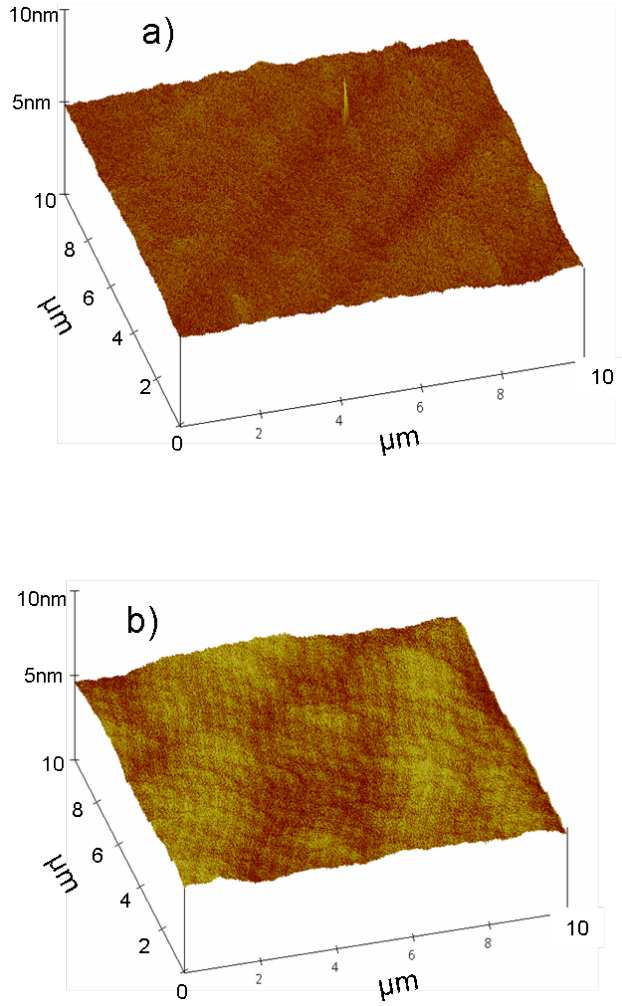


Fig. 7.12: AFM image of the epitaxially grown surface of diamond: $a)$ the surface of the intrinsic buffer layer of $200\,nm$ thickness grown on the polished surface of the diamond substrate; $b)$ the surface of the stack of the delta-doped spikes on top of the intrinsic layer.

7.6 Secondary Ion Mass Spectrometry (SIMS)

The $E6$ partners mainly applied high resolution SIMS to the profiling of the boron delta layers. A large amount of measurements were made in order to compare the layers grown

by E6 and the layers grown in Ulm, the latter employing a solid boron doping source as described above and E6 using doping from the gas phase. A SIMS profile of a layer is shown in Figure 7.13. Two facts had to be taken into account simultaneously: for calibration purposes, the SIMS setup needed at least $50\,nm$ of intrinsic diamond on the surface. This is the reason why the delta layer had been buried $100\,nm$ underneath the surface. On the other hand, the resolution of the SIMS starts to suffer more and more with increasing depth.

Although the resolution stretches across 4 orders of magnitude in concentration, the resolution in depth is unfortunately not in the $1\,nm$ scale. Even at a carrier concentration of $10^{18}\,cm^{-3}$, the limit, where boron is activated in the low percentage range of the width is above $20\,nm$, which is neither confirmed by $C-V$ profiling, nor supported by ERD. It had been clear after a short while, that the resolution of the SIMS profiling technique reached its limit, when the delta profiles approached the window for FET performance. SIMS was however accurate enough for growth rate calibration with thicknesses of more than $100\,nm$. This is why the focus changed to Elastic Recoil Detection (ERD) as alternative using the accelerator of the University of Munich (as described below).

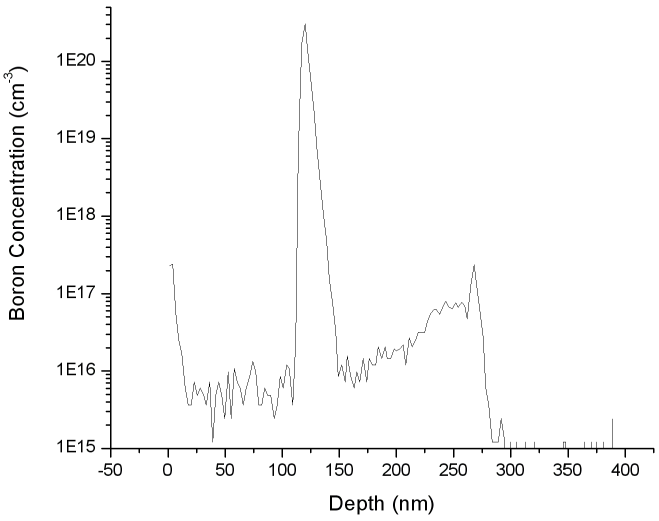


Fig. 7.13: Example of a SIMS profile of the delta layers. Concentrations higher than $10^{20}\,cm^{-3}$ were reached with a FWHM of about $5\,nm$.

7.7 Elastic Recoil Detection (ERD)

The chemical analysis of boron profiles in this investigation was performed with the high resolution Elastic Recoil Detection (ERD) setup at the Munich tandem accelerator [128].

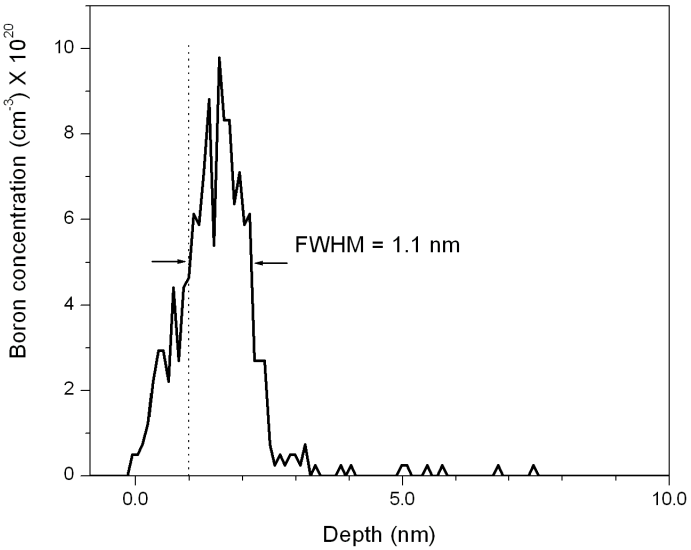


Fig. 7.14: ERD profile of a typical single boron delta-doped profile on diamond. The dashed vertical line showed the approximate starting depth of the nominally undoped layer grown on top of the delta-doped spike.

Elastic Recoil Detection proved to be the more accurate and precise measurement technique that allows physical doping profiling of the δ layers, at the price of being a destructive method.
ERD utilizes Rutherford back scattering of an energetic heavy ion beam on lighter target atoms. During an elastic scattering process the heavy ions transfer part of their energy to the target element. The particles are scattered under a forward scattering angle and identified by their nuclear charge or mass. The initial depth of the counted atom can be calculated from the energy signal. The calculation of the depth profile only requires the scattering cross sections and the energy loss of the ions and scattered atoms. The $Q3D$ magnetic spectrograph at the Munich tandem accelerator with an energy resolution of $\Delta E/E = 7 * 10^{-4}$ showed a depth resolution well below $1\,nm$ for the experiment. Figure 7.14 depicts the profile of a single delta profile with the FWHM of $1.1\,nm$. It shows a delta profile grown onto an undoped buffer followed by a $1.0\,nm$ undoped cap layer. The $1.1\,nm$ FWHM broadness corresponds to about 3 atomic layers of diamond at a lattice constant of $0.35\,nm$. The spike contains a peak concentration of $9 \times 10^{20}\,1/cm^3$. $SIMS$ analysis of similar doping profiles had resulted in similar values [127]. The total sheet concentration within the spike was $7 \times 10^{13}\,1/cm^2$. The gradient toward the buffer follows a slope of $\approx 0.9\,nm/dec$, which is still larger than the Debye-length L_D, which is about $0.1\,nm$ for $N_A = 9 \times 10^{20}\,1/cm^3$. The gradient toward the surface is $\approx 1.2\,nm/dec$, indicating incorporation of boron into the cap layer as well. The step sequence during the growth process proceeded

as follows: First, the boron rod was inserted into a hydrogen plasma for 2 seconds with no methane content, followed by a growth step of 3 sec with a dilute H_2/CH_4 pulse. After this, the plasma was switched off and the gas mixture evacuated. Finally the growth chamber was filled again with the CH_4/H_2 gas mixture to grow a nominally undoped cap layer of $1\,nm$ on top. In Figure 7.14 the approximate location of the cap layer is marked by the vertical dashed line. Despite the growth interrupt, the memory effect in the boron incorporation is still visible.

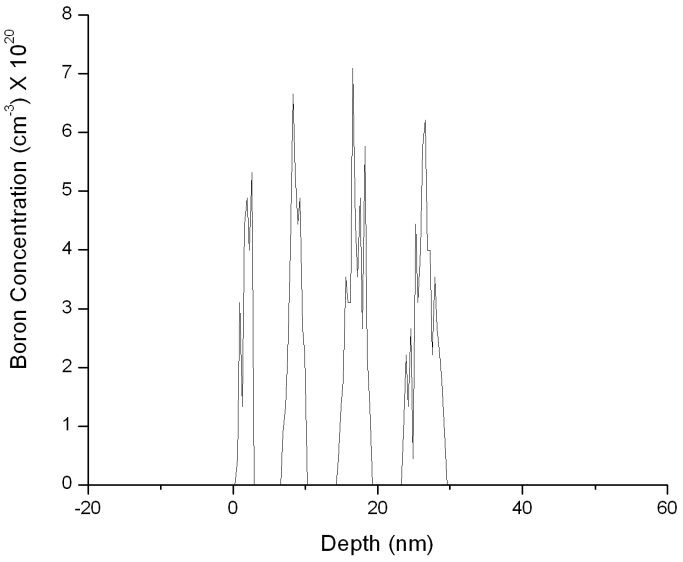


Fig. 7.15: ERD profile of a multiple stack of boron delta-doped profiles grown in one growing process with various durations of the doping pulse.

Figure 7.15 displays a stack of 4 profiles with a FWHM ranging from $1.1\,nm$ to $2.5\,nm$ grown in a similar way as described above, thus also using growth interrupts. In this case the peaks were separated by intermediate undoped spacer layers of $7\,nm$. The peak concentration was in all cases between $5\times10^{20}\,1/cm^3$ and $7\times10^{20}\,1/cm^3$. Varied in this sequence was the length of the H_2/CH_4 growth pulse between $3\,sec$ and $6\,sec$. The $FWHM$ width of the profiles directly reflect this fact. Figure 7.16 shows the ERD profile of a succession of delta layers intentionally modulated by the gas pulsing time $(3-6\,sec)$ from surface to bottom, the top layer being the thinnest and the bottom the thickest. (Measured by A. Bergmaier)[1]
Hence, the ERD analytical technique enabled an establishment of a reproducible growth technique of delta profiles with $nm-$resolution. However, the method is destructive.

[1] Institut f. Angewandte Physik und Messtechnik, Universitaet der Bundeswehr, Muenchen

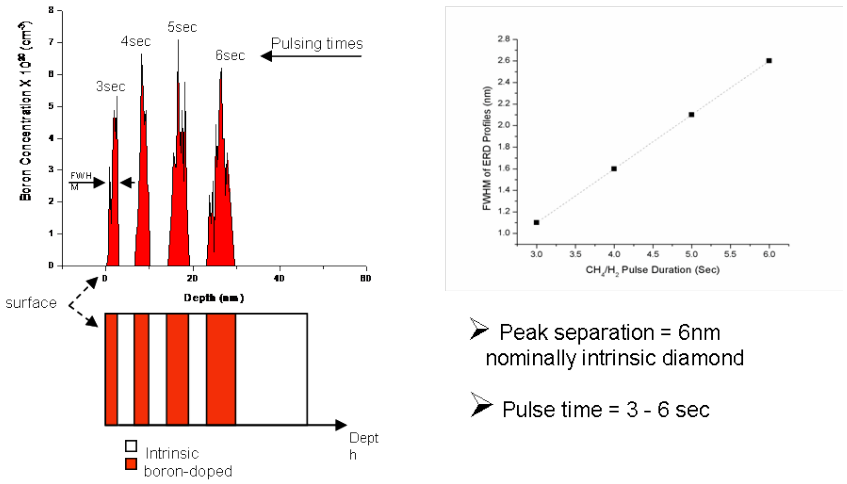


Fig. 7.16: The FWHM of the doping spikes in Figure 7.15 versus the duration of the doping pulse. The doping pulse was counted starting from the injection of CH_4/H_2 gas mixture into the reaction chamber up to plasma switch-off.

Such layers were used in the merged diode structures (Chapter 9) implementing this kind of δ / intrinsic succession, while the thickness of the intrinsic layers is kept below the tunneling thickness of $10\,nm$.

Chapter 8

FET concepts based on Boron δ-Doping

The following sections will summarize shortly the basic concepts and characteristics of MESFETs.

8.1 MESFET Characteristics and Structure

In the MESFET structure shown in figure 8.1, the substrate is nominally intrinsic and semi-insulating in order to lower the parasitic capacitances.

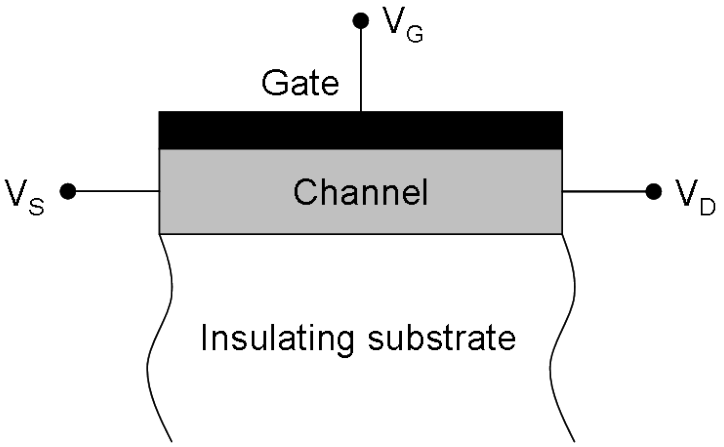


Fig. 8.1: Cross section of a MESFET structure device.

Due to its high carrier mobility, both p-channel and n-channel MESFET are suitable for high frequency applications. As a trade of between speed, short channel effects, and parasitics, the aspect ration of channel length to channel depth L/a is kept around 4.

The mode of operation of a delta doped MESFET is very similar to the one of a HEMT. They both modulate the gate-channel capacitance, which can be easily calculated by differentiating the charge in the two dimensional electron gas with respect to V_G:

$$C_0 = qW_G L_G \frac{dn_s}{dV_G} = \epsilon \frac{W_G L_G}{d_i} \tag{8.1}$$

For the case of constant mobility where $\mu = const$, the current-voltage behavior can be described by:

$$I_D = \beta \left[(V_{GS} - V_{th}) V_{DS} - \frac{V_{DS}^2}{2} \right] \tag{8.2}$$

where β is the transconductance parameter related to the device geometry, given by:

$$\beta = \frac{\epsilon \mu_n W_G}{d_i L_G} \tag{8.3}$$

For drain source voltages which are very small ($V_{DS} << 2(V_{GS} - V_{th})$), the drain current in the linear regime can than be approximated by:

$$I_D \approx \beta V_{DS} (V_{GS} - V_{th}) \tag{8.4}$$

Now considering the constant velocity regime, which takes place at a knee voltage of:

$$V_{DS} \equiv V_K = V_{GS} - V_{th} \tag{8.5}$$

the drain source current in the saturation regime can be formulated as:

$$I_{DSS} = \beta V_0^2 \left(\sqrt{1 + \left(\frac{V_{GS} - V_{th}}{V_0} \right)^2} - 1 \right) \tag{8.6}$$

where $V_0 = E_{crit} L_G$ and E_{crit} is the critical electric field between the constant mobility and the constant velocity regims.

The transconductance in the saturated regime can now be calculated by differentiating the Equation 8.6 with respect to V_{GS}. This results in the small signal transconductance to be written as:

$$g_m = \frac{dI_{DSS}}{dV_{GS}} = \frac{\beta (V_{GS} - V_{th})}{\sqrt{1 + \left(\frac{V_{GS} - V_{th}}{V_0} \right)^2}} \tag{8.7}$$

Furthermore, the gate-source capacitance in this case becomes:

$$C_{GS} = \frac{L_G}{v_{sat}} \frac{\beta V_0 (V_{GS} - V_{th})}{\sqrt{(V_{GS} - V_{th})^2 + V_0^2}} = g_m \frac{L_G}{v_{sat}} \tag{8.8}$$

Finally, for the small signal equivalent circuit, the cutoff frequency used to measure the speed of the device can be approximated by:

$$f_T = \frac{g_m}{2\pi C_{GS}} \tag{8.9}$$

8.2 P-I-P FET

The acronym P-I-P stands for a structure with $p+$ source and drain contact with an intrinsic active channel. The concept of carrier transport in these transistor structures is different from that of a doped channel FET. The one dimensional cross section of such a device is shown in Figure 8.2, where the current flow is defined by the space-charge-limited current.

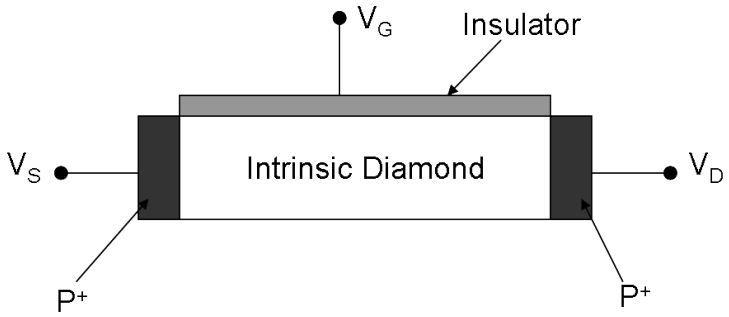


Fig. 8.2: Cross section of a P-I-P transistor device.

In the case of a 1-Dimensional space charge limited current flow, the injected current in the intrinsic diamond region is inversely proportional to the third order of the traveling distance, following the law :

$$J \approx \frac{\mu_h V^2}{L^3} \tag{8.10}$$

However in contrast to Si, the oxygen terminated interface potential in diamond is pinned and cannot be influenced by the gate potential. Thus, an inversion layer cannot be formed and current transport is purely space charge limited. This makes this structure rather critical and short (nm) gate length are needed for high channel current densities.

In reality, and for a normal $2-D$ device shown in Figure 8.3, the output characteristic I_D is a function of V_g) and the analysis in this case depends on the effective gate length and is more complicated due to the non-planar structure. [136]

The holes under the gate area are injected from the source contact into the channel underneath the gate. A gate dielectric separates the gate from the channel and the injected current for the 1-Dimensional case becomes :

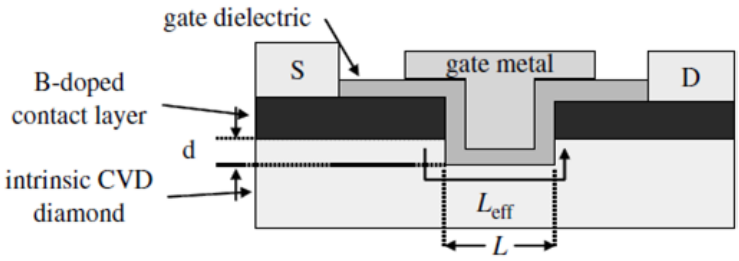


Fig. 8.3: Cross section of a P-I-P transistor device.

$$J \approx \frac{\mu_h V^2}{L_{eff}^3} \tag{8.11}$$

The build-up of an extended drift region for high drain voltages is therefore not straightforward and would need additional lateral channel engineering. The advantage of such a structure is that the carriers travel in intrinsic material with no impurity scattering and are therefore theoretically able to reach very high mobilities like the ones experimentally reported previously ($3800\, cm^2/Vs$).

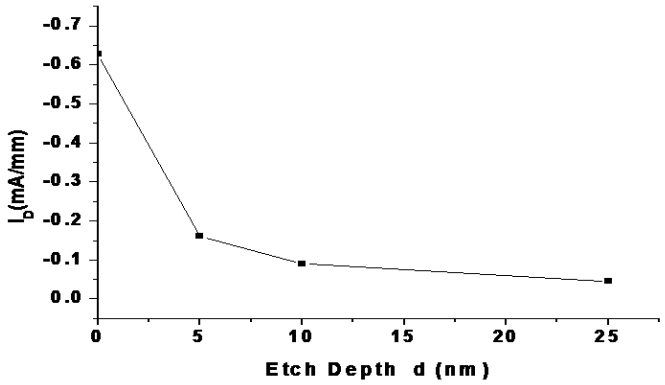


Fig. 8.4: Current drop in $\%$ versus the etching depth d beyond the delta layer thickness, for a gate length of $0.2\,\mu m$.[5]

However, even with short channels the 2D-injection characteristics in planar devices are critical. In case the channel region is etched into a delta layer serving as contact layer, the etching depth, which is basically a recess, has a large influence on the injection characteristics. The recess depth is not only part of the effective channel length, but at the recess corner the field lines change from vertical to horizontal and carrier transport is $2-$dimensional. therefore, the behavior of such a structure needs to be treated numerically. Simulations using the Silvaco platform have shown how critical the etching depth d is in respect to the output current of the device [137].

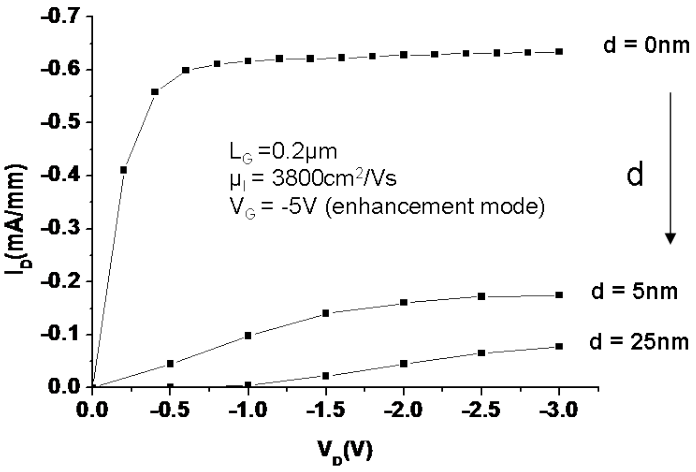


Fig. 8.5: Effect of the over etching depth d on the output characteristic of a simulated P-I-P device.[5]

Figure 8.4 shows a dramatic output current drop of a device with $0.2\,\mu m$ source drain contact separation with respect to the initial current versus etching depth d: only $7\,\%$ of the initial current is left when the over-etching depth of the delta layer becomes $25\,nm$.

Figure 8.5 shows the drop in the output current of a P-I-P transistor in the case of over-etching. The two simulations suggest that the etching process is a very critical step for the fabrication and should be controlled in a nm precise way.

These features of the P-I-P structure indicate that the technology will rely on similar requirements like the ones needed for the delta channel FET concept. What is also required is an etching technique with sub-nm precision and no tail in δ-profile.

8.3 MESFET and MOSFET Structures applied to Diamond

Although the application of diamond as semiconductor features technological difficulties, most device concepts for other semiconductors like Si or compound semiconductors have also been investigated for diamond. There is no extrinsic shallow doping with low thermal activation energy and even among the remaining deep dopants, only boron can serve as active device layer. Another device relevant doping method is the formation of a surface near channel by $H-$termination of the surface. Both of these doping methods have been investigated for FET devices as shown in Figure 8.6.

The left branch in Figure 8.6 illustrates the two common structures for the case of a surface-near $p-$type channel induced by hydrogen termination without extrinsic doping.

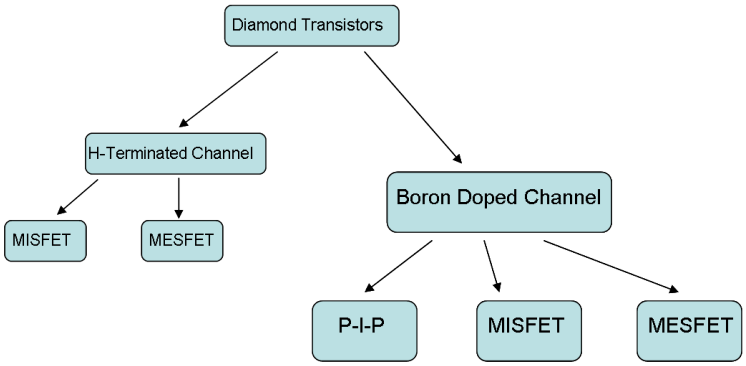


Fig. 8.6: Different concepts of transistors realized so far on diamond. These concepts are limited to unipolar devices, with no hetero-junction p/n FETs.

As already mentioned, the right branch in Figure 8.6 displays the second type based on the concept of a boron (acceptor) delta doping profile, where full activation at room temperature can only be obtained with a high peak concentration above $10^{20}\,cm^{-3}$. This process requires an extremely advanced channel doping technology and fully operational devices had not been realized by the time this project had started. Furthermore, FET structures based on the delta doping profile concept had suffered from incomplete carrier activation, therefore low current levels as will be explained later. To circumvent this problem, the concept of an FET with a channel relying on charge injection from the source contact has also been considered.

The following chapter will describe be the fabrication steps as well as the characteristics of the P-I-P, MISFET and MESFET device concepts.

8.4 δ Channel FET

Theoretical predictions for the high power handling capability of diamond field effect transistor structures have been very high [120, 138, 6]. However, all doping impurities in diamond are deep and thermal activation of free carriers is incomplete at room temperature. To circumvent this problem, two concepts of field-effect transistor devices have emerged. The first relies on a surface-near $p-$type channel induced by hydrogen termination without extrinsic doping [92, 25]. The second follows the concept of a boron (acceptor) delta doping profile, where full activation is obtained by a high peak concentration above $10^{20}\,cm^{-3}$ [126, 125, 139], and which is the subject of this investigation. Up to now microwave performance has only been obtained with the surface-channel FET concept (in MESFET as well as MISFET configurations) on $H-$terminated surface [140, 141]. However, these devices still suffer from severe channel instabilities and degrade at elevated temperature. On the other hand, FET structures based on the delta doping profile concept still suffer from incomplete carrier activation and have therefore suffered from low current levels in the past [125]. Even though a complex recessed gate structure has been used in these FETs, no microwave re-

sults have been available up to now. To obtain full carrier activation at room temperature and full channel current modulation at the same time, the requirements for the delta profile are rather stringent. As already discussed, ideally the delta doping profile should consist of a one monolayer planar doping profile. To implement such a doping profile into an FET structure one needs precise control of the growth and processing parameters, which are in essence the surface preparation, the epitaxy of the active device layers and the etching of the gate recess. Figure 8.7 shows the two most promising device concepts which rely both on the delta doped channel.

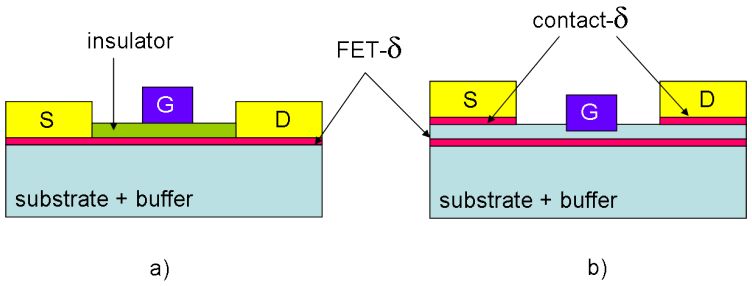


Fig. 8.7: Cross section of the two most promising device concepts relying on the delta doped channel, namely a) MISFET concept and b) MESFET concept

Figure 8.7 (left) shows a basic MISFET device with a gate dielectric layer, which should possess a high dielectric constant (high k dielectric), which could be HfO_2 or Al_2O_3. HfO_2 is a standard high k dielectric in Si technology, Al_2O_3 is often used in GaN based MISFETs. In fact this planar configuration is not attractive without a corresponding recess configuration. The gate recess in such a FET configuration is very crucial and vital. It is needed to provide an effective modulation of the sheet charge density n_S by eliminating the effect of surface charges and related depletion on the device performance. The high surface potential of the oxygen terminated surface is approx. $1.7\,V$, and is the stable surface configuration in diamond. In this case the surface depletion, caused by the surface potential will prevent the use of a large part of the channel sheet charge in the device, limiting the effective channel current density and thus potential power essentially.

Figure 8.7 (right) illustrates the MESFET concept in a recess configuration, using an intrinsic diamond layer as a gate dielectric and another boron delta doped diamond layer as source and drain contact layer. The boron density in the surface layer should be high enough ($\approx 3 \times 10^{13}\,cm^{-3}$) to favorize a tunneling contact to the channel. This highly doped contact layer would theoretically compensate the interface charge on the O-terminated surface, reducing the parasitic resistances between the source and the drain regions and limiting the useful N_S. Again here, a recess under the gate area is just as crucial and important as with the single delta FET structure mentioned above. The separating intrinsic layer between the two delta profiles needs to be thin enough to allow a low resistive (and non-rectifying) tunneling path between the two layers. On the other hand the doping concentration between the two delta layers has to be low enough so that low leakage Schottky contacts can be fab-

ricated on this surface. To realize this structure, therefore also a precise etching technique is needed for the placement of the gate.

For the reduction of parasitic series resistances and current limiters, a second delta layer on top of the channel delta was grown. This top delta layer, called δ_1 is separated from the channel delta layer δ_2 by an intrinsic separation layer of $t_i = 5$ to $10\,nm$ thickness.

Figure 8.8 shows a schematic picture of the doping profile used in a double delta transistor.

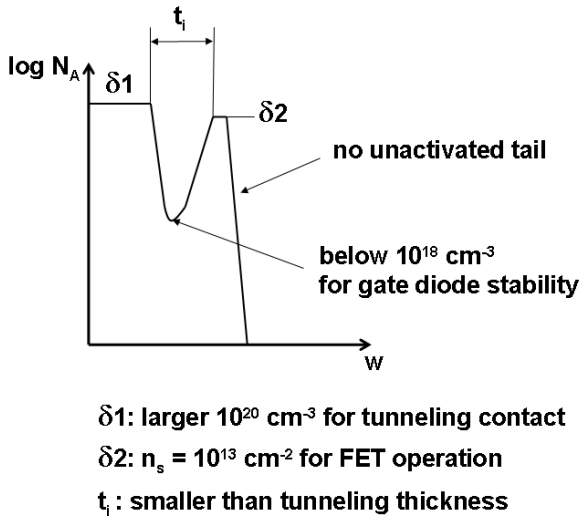


Fig. 8.8: Schematic doping profile for the fabrication of a double delta FET device.[6]

As already discussed, the channel delta layer δ_2 carries the current for device operation. δ_1 is the contact layer. Please refer to Figure 8.7 which shows the difference in device geometry introduced by the double delta profile principle.

8.5 Ion Sensitive FET on Diamond

Due to its chemical inertness and wide potential working range, diamond was recognized as a promising electrode material for various applications, like waste water treatment, electrocatalysis and electrochemical analytics [135, 142, 130]. Diamond is also known as a biocompatible material [143]. Thus, several types of sensor devices on diamond including ion sensitive field effect transistor (ISFET) have been fabricated and tested aiming at biosensing application [144, 145, 146]. However, up to now the fabricated ISFET structures have utilized the $p-$type surface conductivity induced by a hydrogen plasma treatment. Using this simple fabrication method, various ISFET structures have been demonstrated on single crystal [146, 147], poly- [144, 148] and nano-crystalline diamond substrates [145]. The surface potential of the fully $H-$terminated surface does not depend on pH [144, 7]. However the pH sensitivity of the $H-$terminated surface can be observed after a partial

oxidation [146, 148, 7]. After attachment of bio-molecules to the $H-$terminated surface the specific response to biological agents has been detected [145, 149]. However, the $H-$terminated diamond surface is chemically not very stable and can be oxidized in electrolyte solutions under anodic polarization. In acidic solutions the covalent modification of the surface from $H-$termination to $O-$termination has been observed at potentials of about 1.4 to 1.6 vs. $Ag/AgCl$, prior to the onset of the oxygen evolution at the diamond surface [150]. The conversion of the surface termination usually leads to irreversible loss of the $H-$induced conductivity, which can only be restored by an additional $H-$plasma treatment. In the ISFET configuration, the positive surface potentials correspond to the negative biases of the electrolyte gate needed to accumulate the carriers in the $H-$induced surface channel. This bias-induced oxidation limits the gate and drain bias range of the $H-$terminated ISFETs. When the applied bias exceeds the oxidation limit, a fast in-situ degradation of the ISFET devices occurs [111, 151]. In strong acidic and alkaline solutions the surface conductivity of the $H-$terminated diamond may degrade after 6 to 10 cycling [111]. In the case of a polycrystalline surface the degradation effects have been promoted by the charge transfer reaction via grain boundary defects [151]. All these phenomena limit the field of operation, the range of detection for chemical species and the life-time of the ISFET devices with $H-$induced channel. In order to explore the potential of diamond in full, a new ISFET structure is needed, which incorporates a chemically stable channel in contact to electrolyte solutions and a chemically stable surface termination. Here, we propose and describe a new concept of an ISFET on diamond using a boron delta-doped surface channel and oxygen-terminated surface. The surface of boron-doped diamond have been shown as extremely resistant against corrosion in contact with aggressive chemicals [135]. No degradation of the electrode surface has been observed even after a long-time oxidation of organic components like phenole at high anodic potentials [135, 152]. Also, the carbon-oxygen functional groups on the diamond surface have been proved as chemically and thermally very stable [153]. Additional advantage of the $O-$termination is that the $C-O$ functional groups provide an acid-base equilibrium at the interface with electrolyte solutions [7]. So, the surface potential of the $O-$terminated surface diamond depends on pH. In the following sections we describe the fabrication of the first boron-doped ISFET on diamond substrate with $pH-$sensing characteristics. The ISFET structures were fabricated on a single crystal diamond, which may represent the ideal case of an extremely well-ordered surface with no grain boundary defects. For better understanding the surface properties, the ISFET characteristics were compared to those of a boron-doped electrode, also fabricated on a single crystal diamond substrate with the identical doping parameters.

A schematic cross-section of the proposed ISFET is shown in Figure 8.9 $a)$. The structure follows the design of a simple FET with a doped channel in direct contact with electrolytes. The gate length L_G is formed by an epoxy passivation of the source and drain contact areas.

In general, two $RC-$circuits in series can be expected for a semiconductor-electrolyte junction in the absence of any adsorption or charge transfer reactions [153], as was already discussed in chapter 6.1. One $RC-$circuit is related to the depletion (space change) layer in the semiconductor (R_{SC}, C_{SC}), another one being attributed to an electrical double layer at the semiconductor surface (R_{dl}, C_{dl}). At equilibrium, the value of the surface potential

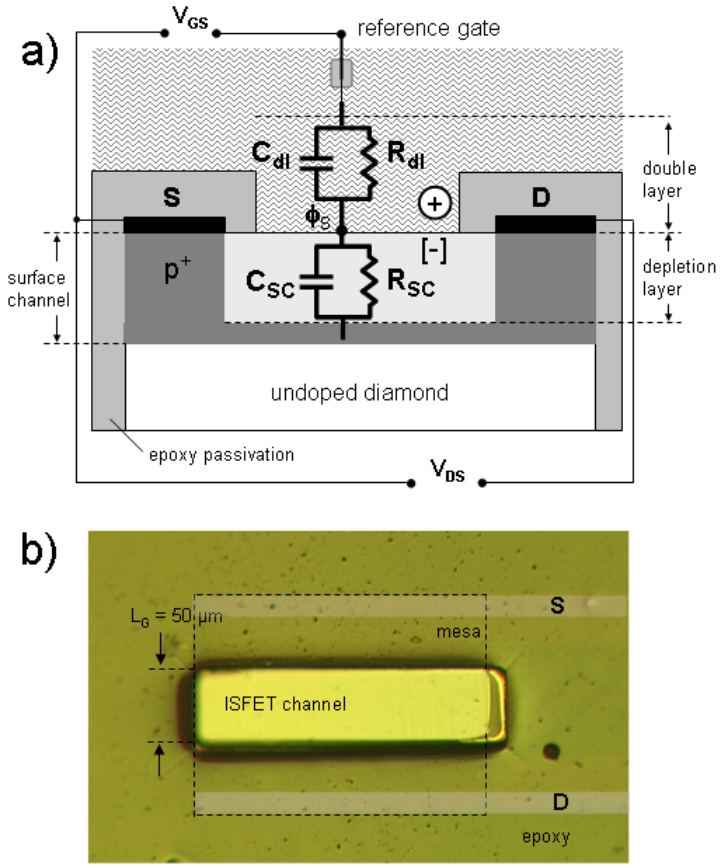


Fig. 8.9: $a)$ Schematic cross section of the ion sensitive FET with boron doped channel including the equivalent circuit of the diamond electrolyte interface, and $b)$ the layout of a single micro ISFET fabricated on single crystal diamond substrate.

Φ_S is given by the charge transfer rate between ions in the electrolyte and the chemically active states at the semiconductor surface. Variation of the surface potential with pH can be measured by the corresponding shift of the pinch-off voltage V_T of the FET channel.

For an ISFET channel in contact with an electrolyte, the applied gate bias is limited by the gate leakage induced by the electrochemical activity at the channel surface. In simple electrolyte solutions these limits are the onset potentials of the hydrogen and oxygen evolutions. The maximum gate bias for carrier accumulation in the ISFET channel is the flat-band potential. For the $B-$doped and $O-$terminated diamond electrodes the flat-band voltage is typically in the positive potential range very close to the onset of the anodic current [7]. This means that the maximum gate bias range ΔV_{Gmax} between the flat-band to the pinched-off conditions of the channel can be taken as equal to the potential window for water stability at the diamond surface. As already mentioned, this potential window is about $3\,V$ for single crystal diamond electrodes [135, 142, 130] . To provide the high sensitivity, the boron concentration in the channel N_A should be equal or above the full activation limit

of the boron acceptors in diamond, which is about $10^{20}\,cm^{-3}$. The doping concentration below this threshold would lead to an increasingly high resistance of the channel due to incomplete ionization of the acceptors. However to pinch the channel off, all boron acceptors need to be depleted. Therefore the transconductance $g_m = \delta I_D/\delta V_{GS}$ of the device with the low boron concentration would be very low. These considerations can be used to calculate the optimum thickness of the $ISFET$ channel d_{opt} , which, for a "'box like"' shape doping profile, can be expressed as:

$$d_{opt} = \sqrt{2\epsilon\Delta V_G^{max}/qN_A} \tag{8.12}$$

where ϵ is the dielectric constant of diamond and q is the elementary change. Taking the maximum gate bias range ΔV_G^{max} equal to $3\,V$ and the doping concentration N_A of $10^{20}\,cm^{-3}$, the value of d_{opt} will be about $2\,nm$. This gives the optimum density of the boron acceptors in the ISFET of about $2 \times 10^{13}\,cm^{-2}$.

Chapter 9

Technology and Fabrication Process

9.1 Technological Steps

The processing toward a transistor device has started with the preparation of a mask design set as shown in Figure 9.1. This mask contained the following structures:

- TLM patterns for R_s (sheet resistance) and ρ_c (specific contact resistance) measurements,
- A 4 point Hall pattern for mobility measurements,
- Diode structures of different sizes for $C - V$ measurements,
- Circular FET structures with various gate lengths,
- FET with Π and T shaped gate layout, suitable for microwave measurements (also with different gate lengths and gate widths)

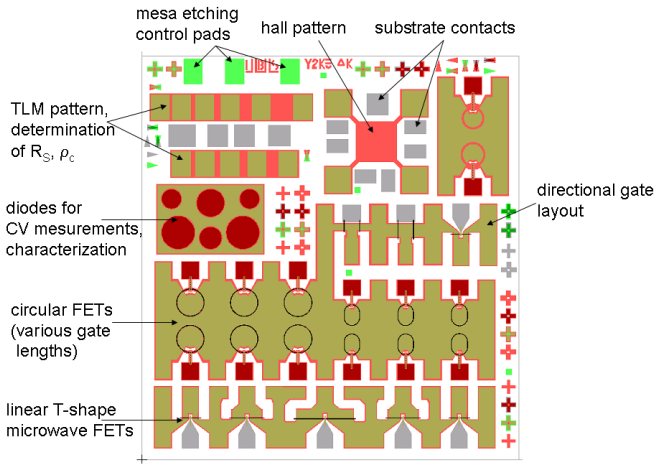


Fig. 9.1: Transistor fabrication mask with circular gates.

The design also contains contact pads for mesa etching control and other substrate contacts (usually Al).

Several microscopic charts in Figure 9.2 illustrate a showcase of circular shaped transistor devices: a circular transistor during its different fabrication stages. Firstly the mesa is etched, followed by the ohmic metalization, then the recess etching under the gate and finally the gate metalization are performed.

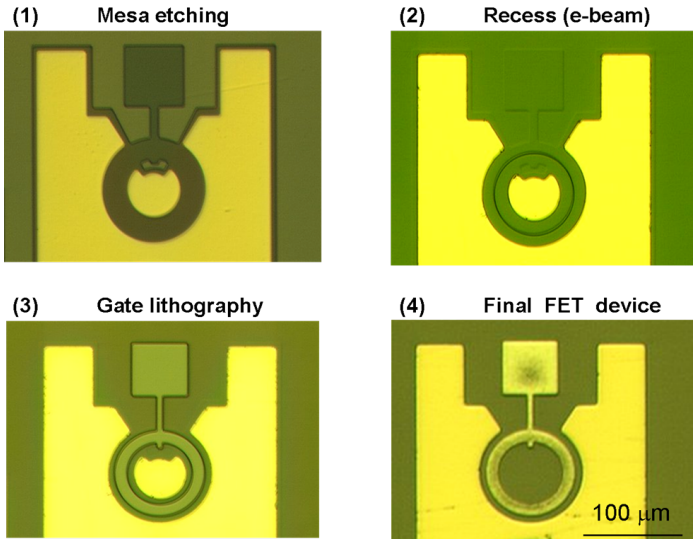


Fig. 9.2: Microscopic images of some circular shaped transistors during different processing stages.

After a short time it became obvious that the surface finish of the delivered substrates was not smooth enough for the electronic application. Even though the surface was smoothened with hydrogen plasma, the polishing lines remained noticeable (see section 7.5). This is the reason why there was a need to redesign the fabrication mask.

The new mask mainly consisted of Π and T shaped transistor geometries, which can be aligned in the direction of the polishing lines, preventing the gate to perpendicularly cross these polishing lines as it was the case with the circular FETs. Moreover, the new mask shown in Figure 9.3 contains few FETs perpendicular to the common gate direction in order to investigate this particular effect of surface polish.

Again, the size of the cell layout ($1.5 \times 1.5\, mm^2$) was determined according to the limitation that 4 identical fields of the same geometry had to fit onto one chip of the normal size ($3.6 \times 3.6\, mm^2$). This allows for some variations in the processing on the different fields, e.g. variation of recess etching as shown in Figure 9.4.

9.1.1 Ohmic contact Technology

Usually, Ohmic contacts to diamond rely on carbide forming metals. However in the case of high doping concentrations, contacts are possible by tunneling. In order to identify the best combination, ohmic contacts were fabricated which were based on stacks with Ti and

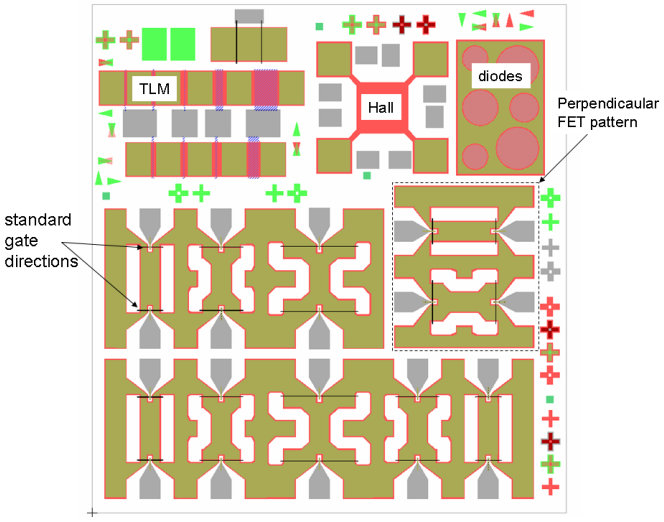


Fig. 9.3: New improved mask with linear gate structures encountering for the surface polishing lines.

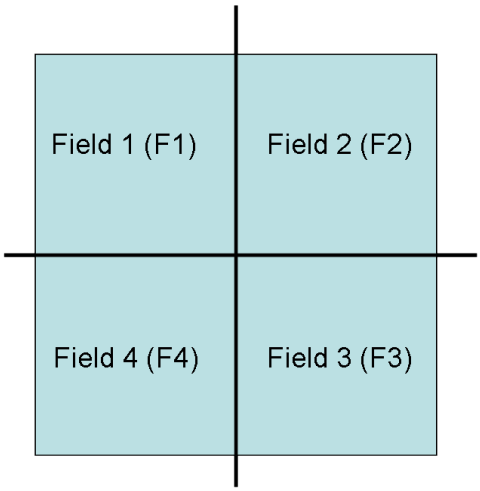


Fig. 9.4: Sample of the normal $3.6 \times 3.6\, mm^2$ size divided into four fields, adding a degree of freedom into the fabrication cycle.

$W : Si$ at the diamond interface and annealed at different temperatures. Furthermore, different sources of aluminum oxide as gate insulator were tested and evaluated, either by evaporation or ion beam sputtering. A third alternative for a lossy gate dielectric was nitrogen doped diamond like mentioned before, which was also included in the test series.

The second fabrication step of the FET is the deposition of the source and drain ohmic contacts as shown in Figure 9.5.

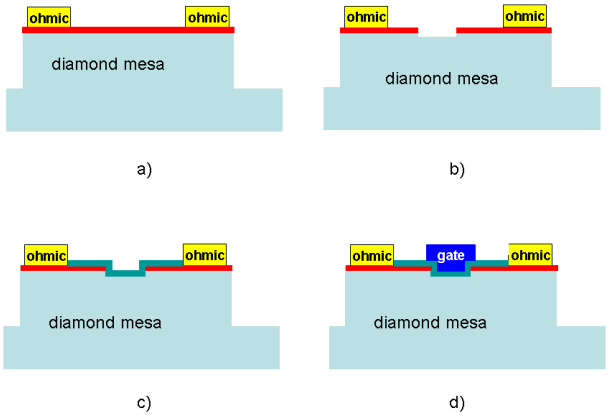


Fig. 9.5: Fabrication step sequence for the example of a P-I-P transistor device.

In the case of the $W : Si$ contact scheme, which had been chosen as the standard, the metalization had been deposited in an Ion Beam Sputter Deposition apparatus (Millatron) in argon atmosphere. For more details about the deposition conditions please see Appendix A. These high temperature ohmic contacts consist of a 4 layer sequence (see Figure 9.6) of:

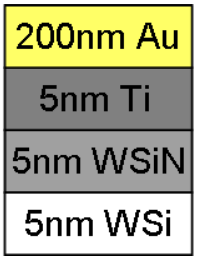


Fig. 9.6: The high temperature metal sequence used in the fabrication of the ohmic contacts.

- 5nm of WSi
- 5nm of WSiN
- 5nm of Ti
- 200nm of Au

The contact material is W:Si. The addition of nitrogen to form $W : Si : N$ serves as stuffed barrier system preventing recrystallization at high temperature ($800°C$) and serves as diffusion barrier to the Ti/Au over layer. Ti is the adhesion promoter to Au.

For more details about the lithography process, please refer also to Appendix A. The whole layer stack is then annealed at $650°C$ in nitrogen atmosphere for 1 minute in a Rapid Ther-

mal Annealing apparatus (RTA). For more information about the RTA annealing process, please refer again to Appendix A.

9.1.2 Gate contact technology

Depending on the gate diode employed for the channel modulation, a delta channel FET can operate either as a MESFET in the case of a Schottky gate, as a MISFET in the case of a MIS gate diode or as a lossy dielectric JFET in the case of a $pn-$ gate diode.

A $pn-$diode between a boron delta doped diamond and gate metal using nitrogen shows less leakage current in reverse direction combined with a higher breakdown voltage, if compared with a normal Schottky diode on nominally intrinsic diamond. These better characteristics are mainly due to the higher built-in potential of the pn-junction with $V_{bi} = 3.5\,V$, as compared with the Schottky contact barrier height on oxygen terminated diamond surfaces of $\Phi_b = 1.7\,V$. This higher potential makes however a deeper recess trench necessary, but allows also higher gate bias in enhancement mode.

9.1.3 Gate recess

The concept of gate recess was developed and used in order to avoid parasitic current limiting effects caused by surface depletion as shown in Figure 9.7. In addition it improves the source and drain channel access resistances, which results in a better carrier modulation in the channel and a higher transconductance g_m . It is obtained by etching the diamond surface, moving the gate contact closer to the delta channel.

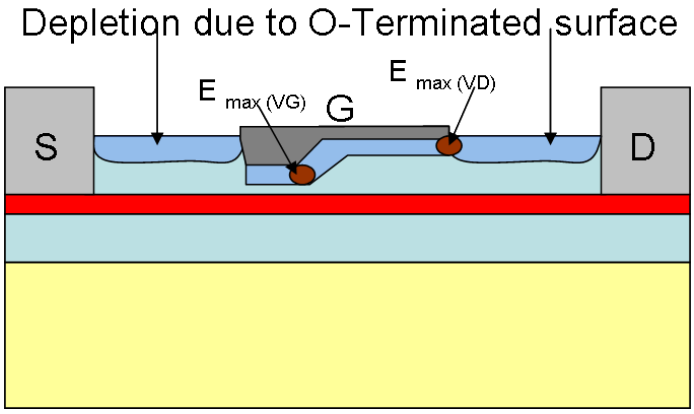


Fig. 9.7: Cross section design of a single delta MESFET with gate recess and field plate.

The gate recess is essential in the design of high power devices. The effect of the gate recess was the subject of many theoretical studies and simulations. For an optimum of the diamond power FET device structure, it has been shown that as much as $75\,W/mm$ power can be expected at a drain current of $2,5\,A/mm$ biased at a drain voltage of $250\,V$, if field plates are used in addition.

9.1.4 Mesa etching

Before starting the etching experiments on transistor structures, the etching process had to be calibrated, because the etching rate depended on the geometry of the structure, in particular the recess width. Therefore, the test assembly hat to be well defined. Figure 9.8 illustrates the etching rate dependence of the standard etching process in a Ar/O_2 plasma on the width of the recess structure. The etch mask was e-beam resist, which is also a carbon material and etched faster than diamond. Etching was performed with a pressure of $110\,mTorr$ and a power of $25\,W$ (on a $6\,inch$ diameter substrate holder). The etch depth was measured using AFM for different pattern widths. It is important to note that the etching rate tends to be faster with increasing width, it even doubles for structures of more than $2\,\mu m$ width.

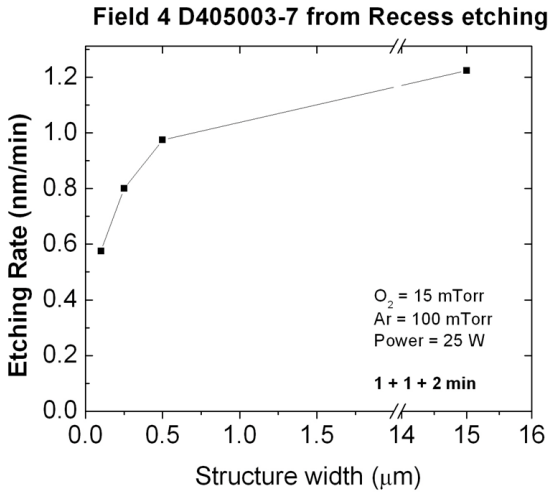


Fig. 9.8: Calibration measurement showing the diamond etching rate as a function of the structure width. RF power is $25\,W$ on a 6 inch electrode.

The mesa etching for electrical device isolation is performed using the same Ar/O_2 plasma dry etch process as described above. The processing parameters were: $1\,\%$ oxygen in the gas phase, a self bias potential of $100\,V$ and a power level of $25\,W$, ensuring a controllable etching rate of around $1\,nm/minute$.

9.1.5 Recess etching and overgrowth

In the next step the channel area underneath the gate has to be etched as shown in Figure 9.5 b. This procedure is equal to etching for mesa formation, using a patterned $e-$beam resist mask. For more details about the used $e-$beam lithography please refer again to Appendix A. In the case shown the device is a P-I-P transistor and the recess etched through the entire profile.

Then follows the the overgrowth of the gate area in the MESFET or and P-I-P device fabrication process. In the case of the P-I-P structure this will avoid the deep trench for the carrier injection path, which is critical in respect to the current level which can be obtained. It will serve as gate dielectric insulation in the case of the single delta profile FET, see Figure 9.5 d.

9.2 Single delta MISFET

The double-delta FET process cycle mentioned in the previous section is a complicated and time consuming procedure. Although the single delta MISFET process is an essentially simpler and faster alternative, it has the drawback of larger series resistances.

For this technology, single boron delta doped layers were capped with an intrinsic layer of $25\,nm$ thickness.

As sketched in Figure 9.9 and Figure 9.10 (cross section of the device), the technology of such a MIS device is as follows:

First, the mesa for electric device isolation was etched employing a dry etch by argon/oxygen plasma with $1\,\%$ oxygen in the gas phase and a self bias potential of $100\,V$, at a power of $25\,W/6''$ drain electrode (standard process in Appendix A), ensuring a controllable etching rate of around $1.0\,nm/minute$. The mesa etching was performed in a succession of etching and measuring steps. By measuring the resistance between the mesas, the exact depth of the channel delta layer could be verified.

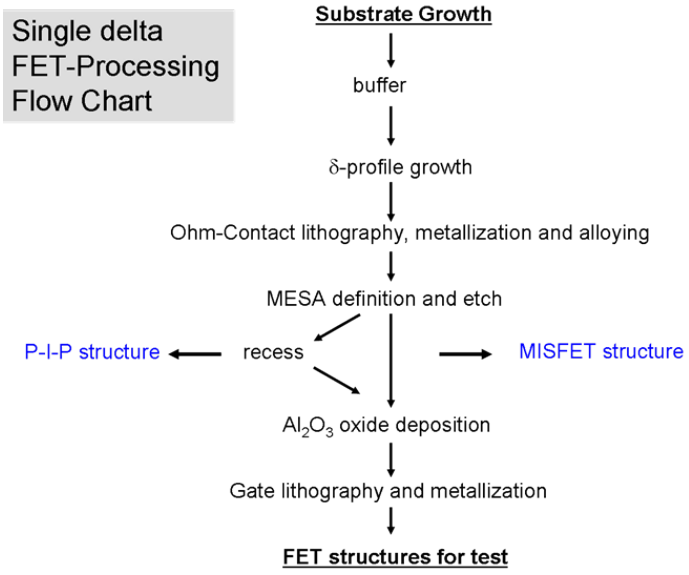


Fig. 9.9: processing flow chart for the single delta FET device.

In the next step, etching through the cap layer was conducted to form the source and drain contact areas on the delta-doped channel. The ohmic contacts were formed by metal deposition using an ion beam sputter deposition system. The deposited contact layers consisted of a stack of 4 different metals starting with $5\,nm$ of $W:Si$, $5\,nm$ of $W:Si:N$, $5\,nm$ of Ti and $250\,nm$ of Au, as already mentioned before.

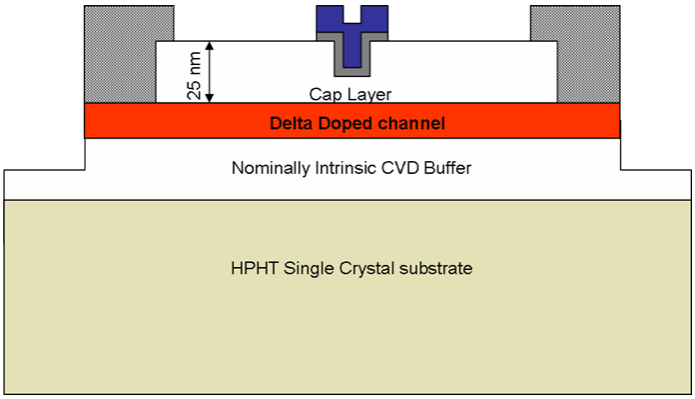


Fig. 9.10: Simplified cross section of the MIS device geometry with single delta layer.

In the following stage, the gate recess was etched using the calibration data on the etching rate from the mesa etching experiments. The open window in the photo resist for the gate recess etching was formed either optically for large gate lengths or by $e-$beam lithography for short gate lengths. Then the gate recess was dry etched with argon/oxygen plasma. As already mentioned earlier, the thickness of the diamond cap layer was $25\,nm$, the depth of the etched gate recess was about $15\,nm$, which results in about $10\,nm$ for the thickness of the intrinsic diamond cap layer remaining above the delta-doped channel.

Several test runs proved that the nominally intrinsic cap layer did not reveal Schottky barrier characteristics, but rather a non-rectifying behavior of the metal gate contact. Therefore, the residual boron level in this cap layer must still have been high, or the thickness of the cap layer was below the tunneling thickness. For this reason an intermediate Al_2O_3 dielectric layer was deposited, although this would degrade the aspect ratio of the structure and reduce the transconductance.

The last fabrication step included the deposition of an aluminum-oxide layer as the gate insulator. Al_2O_3 was sputter deposited in argon atmosphere at room temperature, using an ion beam sputter apparatus. The sputter deposition rate had been about $2\,nm/min$, at a pressure of $4.10^{-4}\,Torr$. The thickness of the aluminum-oxide layer was about $30\,nm$. On top of the layer, the aluminum gate metalization was evaporated through the identical mask. The Al metalization and the aluminum-oxide layer were lifted off in the same lithographic step.

As noted in some of the previous experiments, Al_2O_3 seems to change the surface potential of the oxygen terminated surface (normally assumed as about $1.7\,eV$). This effect had not been expected. Al_2O_3 obviously enlarges the surface depletion with a barrier potential of $3.0\,eV$.

Here, Al_2O_3 was used only below the gate, which should result in stronger channel depletion, thus allowing the device to operate also in the enhancement mode under forward bias. The breakdown field of such an insulating layer of Al_2O_3 was measured and found to be in the range of $6.10^6\, V/cm$ for a thickness of $30\, nm$.

With this structure, initial DC and RF results were obtained and will be presented next in the result chapter.

The boron delta-doped profiles were grown on (HTHP) (100) oriented type Ib single crystal diamond substrates. The selected diamond substrates were characterized by a surface roughness measured by AFM below $1.0\, nm$ (rms) within a $10 \times 10\, \mu m^2$ area. The epitaxial diamond layer stack was grown using microwave plasma CVD (a modified Astex 1500 apparatus). At first, the diamond substrates were polished in a pure hydrogen plasma for $20 - 30$ minutes at $T = 750\,^{\circ}C$, similar to the process described in [11]. This treatment resulted in a typical RMS roughness of less than $0.6\, nm$. A nominally undoped buffer layer was grown in-situ on this prepared surface. The buffer layer was grown at a temperature of $700\,^{\circ}C$ with a methane concentration of $0.3\,\%$ in hydrogen at a pressure of $2.5\, kPa$. The thickness was $250\, nm$. The surface roughness after this growth step was reduced down to $0.3\, nm$. In the next step, the growth was interrupted and the boron delta-doped profile was grown using the pulse doping technique described earlier. This procedure consists of a sequence of gas flow pulses controlled and timed by mass flow controllers and computerized valves. The source of boron was a boron rod inserted into the plasma. The gas concentrations in the chamber were monitored by a quadrupole mass spectrometer. Finally, an intrinsic cap layer (nominally undoped) of $25\, nm$ was grown on top of the delta-doped profile sequence. An AFM image of the final CVD surface after the growth of the delta-profile is shown in Figure 9.11. The surface roughness was about $0.3\, nm$ (RMS) scanned across a $10 \times 10\, \mu m^2$ area. The smoothness of the CVD surface confirmed that no boron clusters had been formed during the growth.

A schematic cross section of the fabricated device structure including the mesa and gate recess is shown in Figure 9.12. The procedure was as follows: In a first step, the mesa for electric device isolation was dry-etched in an argon/oxygen plasma under the conditions already described before. The etching rate was kept low and controllable at around $1.0\, nm/minute$. The mesa etching was carried out in a sequence of etching and measuring steps. When the electrical resistance between the mesas was measured, an electrical resistance profile, equivalent to the depth profile of the channel delta layer was, obtained.

After these steps, source and drain contact areas were defined by lithography and the cap layer was etched to contact the delta-doped channel, with the help of an ion beam deposition system. The deposited contact layers comprised a stack of 4 metalization layers including $5\, nm$ of WSi, $5\, nm$ $WSiN$, $5\, nm$ of Ti and $250\, nm$ of Au on top. They were annealed at $600\,^{\circ}C$ by RTA in nitrogen. In the following stage, the gate recess was etched using the calibration data from the mesa etching experiment. The resist opening for the gate recess etching was formed by $e-$beam lithography. Then the recess was dry-etched with an argon/oxygen plasma with an etch rate of $1.0\, nm/minute$, permitting a very accurate control of the gate recess depth. The thickness of the diamond cap layer of the devices discussed

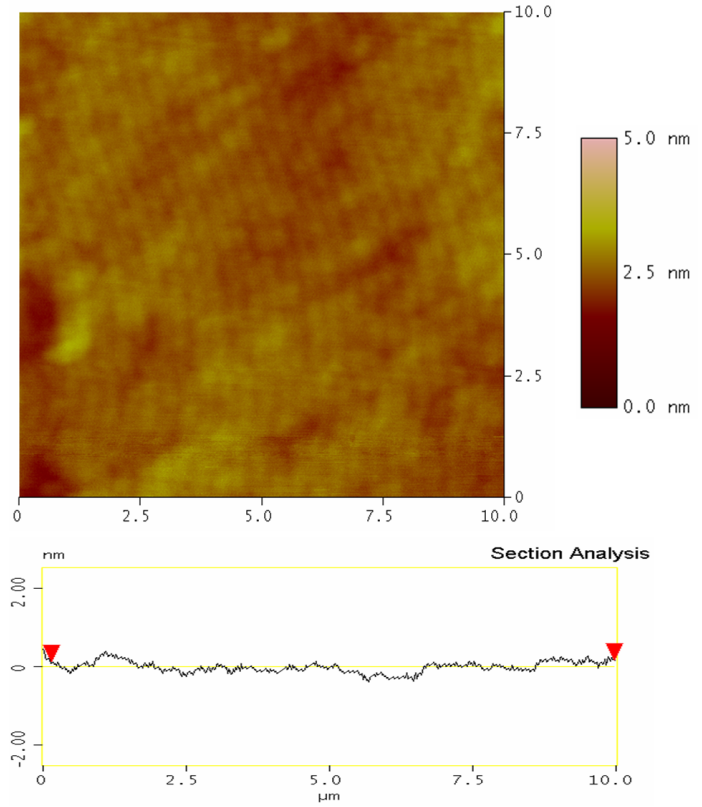


Fig. 9.11: AFM image of the diamond epitaxial layer after the growth of $250\,nm$ of the intrinsic buffer, the boron delta-doped channel and the diamond cap layer of $25\,nm$ thickness. The RMS smoothness value of the surface was $0.2\,nm$ while the peak to peak value was less than $1\,nm$

below was $25\,nm$ and the depth of the etched gate recess was $\approx 15\,nm$. As a result, the thickness of the diamond cap remaining above the delta-doped channel was about $10\,nm$. During the last fabrication step the aluminum oxide gate insulator was deposited, utilizing Al_2O_3 in argon atmosphere at room temperature with an ion beam deposition apparatus. The deposition rate was about $2\,nm/min$ at a pressure of $4.10^{-4}\,Torr$. The thickness of the deposited aluminum-oxide layer amounted to $25\,nm$. On top of this layer, an aluminum gate metalization was evaporated through the same resist mask. The Al metalization and the aluminum-oxide layer were lifted off simultaneously, so that the geometry of the gate dielectric and gate metalization was self-aligned. The overlap with the un-recessed regions was $0.1\,\mu m$.

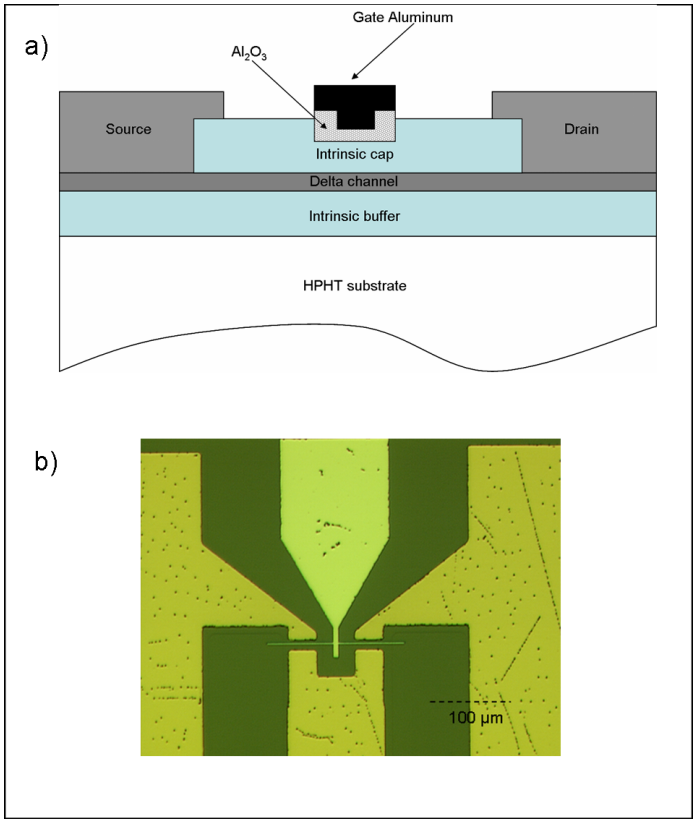


Fig. 9.12: (a) A schematic cross-section of a single MISFET device structure showing the etched mesa, ohmic contacts and the gate recess with $Al-$oxide insulating layer. (b) a micrograph of the device.

9.3 Double delta layer transistors

For the case of Double delta transistor fabrication, current measurements during mesa etching are very important to determine the thickness of the δ_1 layer of the double delta samples. That is why this fabrication cycle had the highest number of differential steps, as shown in Figure C.2. If the top delta layer is not completely etched, there will be no current modulation of the channel and early breakdown.

During all recess etching cycles, $I-V$ measurements are performed. Before and after each etching step, the current on one or several patterns of different widths is measured, and compared to the un-etched case.

In an additional stage the recess depth on the chip was varied by etching each quarter separately as shown earlier in Figure 9.4 in order to increase the chance of reaching the window in recess depth for complete channel modulation. Usually, field 1 is left without recess etching, to have a reference according to the initial current level. Before each etching process, an additional field is covered with photoresist, to protect it from being etched.

All details about the lithography processes, the metal deposition and annealing procedures, the $e-$beam processes, the dry etching and all fabrication steps can be found in Appendix A.

Figure 9.13 displays a typical investigation of a TLM measurement performed on a double delta layer as shown in the cross section insert picture. Typical values for the specific contact resistance are in the range of $\rho_c = 9.5 \times 10^{-5}\ \Omega cm^2$. The sheet resistance is typically around $9\ k\Omega$ per square, which is only marginally higher than the sheet resistance induced from the hydrogen terminated diamond surfaces.

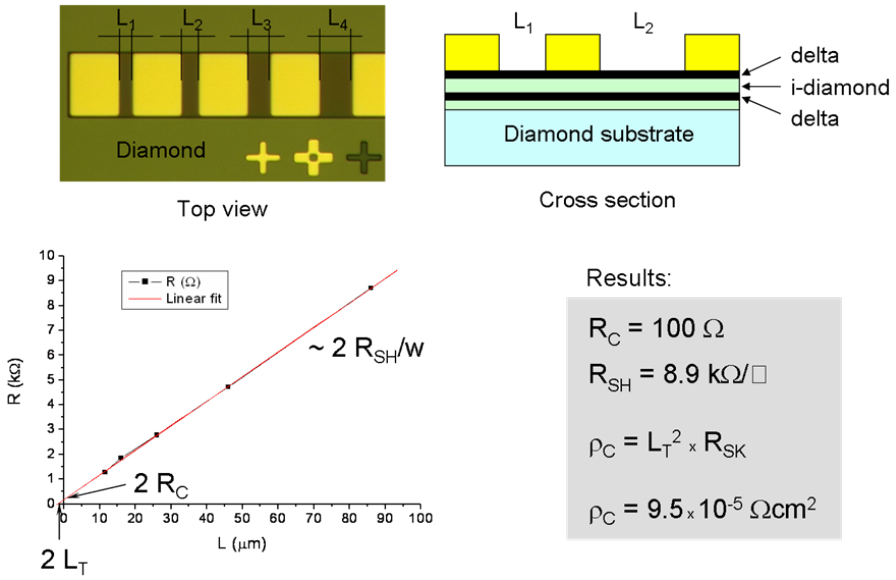


Fig. 9.13: A typical TLM measurement in the recess structure for the evaluation of the sheet resistance and the contact resistance.

9.4 Double delta FETs with dielectric layer prior to metalization

To avoid the interface between the crystalline diamond semiconductor and the amorphous gate dielectric, intrinsic diamond can substitute the gate dielectric oxide layer. A structure without interface state and defects may improve the stability of the breakdown behavior.

In fact, the concept of using the two delta layers, δ_2 as the channel and δ_1 for the contacts requires the etching of two different recess trenches. The inner gate recess itself is necessary in order to remove the conductive layer at the top under the gate region. The channel recess, as shown in Figure 9.14 adjusts the pinch-off voltage of the active channel. The outer recess is needed to avoid any overlap of the gate contact metalization onto the highly doped cap layer, which would cause high coupling capacitances, especially between gate and drain.

Previous experiments have shown that the intrinsic diamond overgrowth of any sample with any kind of metal on its surface results in a rough surface with many defects and a very low

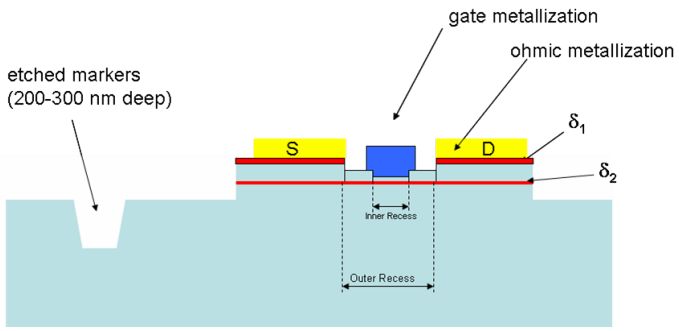


Fig. 9.14: Schematic of a sample's cross section with metal free overgrowth capability.

breakdown voltage. Therefore, the already processed samples need to be overgrown, while avoiding any metal on the surface.

To realize this idea, additional measures had to be introduced. As the standard processing cycles start with ohmic metalization or mesa etching, the metal in this process has to be kept till the last step. But then, there are no alignment keys for the optical and e-beam lithography steps, which is much more critical according to the marker quality. Thus, metal keys were substituted by etched markers.

Some experiments have been made to test the alignment of $e-$beam steps onto etched markers and useful parameters were identified.

The modified processing cycle for the double delta transistor with overgrown gate isolation layer without the presence of metals on the surface appeared finally as follows:

1. Cleaning of the sample;
2. Growth of the buffer layer;
3. Growth of the device layer stack (δ_2, intrinsic spacer layer, δ_1);
4. Etching of the alignment markers of $300\,nm$ depth;
5. Mesa etching aligned to the etched markers;
6. Channel recess etching aligned to the etched markers;
7. Gate recess etching aligned to the etched markers;
8. Intrinsic overgrowth of the sample for the gate dielectric;
9. Gate lithography and gate metalization aligned to the etched markers;
10. Lithography for the ohmic contacts;
11. Etching the overgrown intrinsic layer on ohmic contact areas to obtain better tunneling contacts;
12. Deposition of the ohmic metalization.

In this listing, the steps 9 and $10-12$ could also be exchanged, but this order seems to be more convenient. A high number of $e-$beam steps are incorporated, which are complex and time consuming, especially when the etched markers are used.

Figure 9.15 shows SEM pictures of finished FET structures fabricated with the metal-free alignment procedure and the etched alignment markers. Using the geometrically corrected markers, accurate alignment is possible.

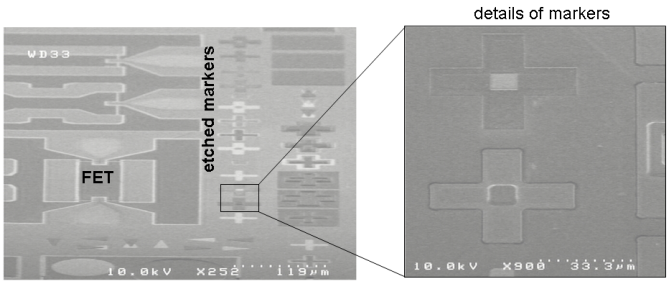


Fig. 9.15: SEM pictures of FETs and etched markers for alignment of all the processing steps.

9.5 ISFET on Single crystal Diamond

One sample, grown as already described, served for the fabrication of the ISFET micro-structures, and the second one was packaged in a Teflon adhesive foil without structuring and used as an electrode. Prior to the channel growth, a $100\,nm$ thick layer of intrinsic diamond was grown on the mechanically polished surfaces in the MWCVD reactor. The surface boron-doped channel was formed with the growth interrupt. No additional low-doped diamond layer was grown on top of the channel. The average surface roughness of the prepared samples was below $1\,nm$ by AFM. After the growth the diamond samples were exposed to a wet chemical treatment in hot $H_2O_2 : H_2SO_4$ $(1:2)$ solution for oxygen termination. The XPS measurement of the oxidized sample revealed the presence of the carbon-oxygen groups on the surface. The O^{1s} to C^{1s} peaks ratio in the XPS spectrum of the oxidised surface was about $1.4\,\%$. The resistance of the grown surface layer was about $6.7\,k\Omega$ /square. The carrier mobility μ_Δ and the sheet charge density n_s in the channel by room temperature were about $10\,cm^2/Vsec$ and $4.10^{13}\,cm^{-2}$ respectively. The temperature dependence of the channel conductivity did not show any activation energy in the temperature range up to $200\,^\circ C$. It proved that the average doping concentration in the channel had been above the full activation limit of $10^{20}\,cm^{-3}$. The ISFET micro-structures were formed by mesa etching through a photoresistive mask. The source and drain ohmic contacts to the surface delta-doped channels were made by a Ti/Au metalization. The open gate areas in the epoxy passivation layer were structures by the lift-off technique. The fabricated structures were tested in $0.1M\ H_2SO_4$ and $0.1M\ KOH$ solution in a three-electrode electro-

chemical cell. The solutions were de-aerated by nitrogen bubbles. The gate potentials were referenced to the potential of the saturated calomel electrode (SCE, $E^0_{SCE} = +242\,mV$ vs. NHE). The cyclic voltametry, and electrochemical impedance measurements with the electrode sample were made using $PARSTAT2273$ potentiostat (Princeton Applied Research). All measurements of the ISFET and the electrode characteristics were performed in a grounded Faraday cage.

Chapter 10

Results

10.1 Double delta transistors

Double delta FETs have been characterized in DC by their $I-V$ characteristics and temperature behavior. Additionally, $s-$parameter measurements have been performed to extract f_T.

Here, the gate metal was deposited on the intrinsic separation layer between the two delta profiles after the first etching cycle, using this intermediate separation layer between the double-delta profiles as gate dielectric. The output characteristics showed weak modulation of the channel current, and early gate breakdown. High gate leakage currents were detected. The drain current levels have been in the range of several $10\,mA/mm$. It was therefore concluded, that the top delta layer was not completely etched through yet.

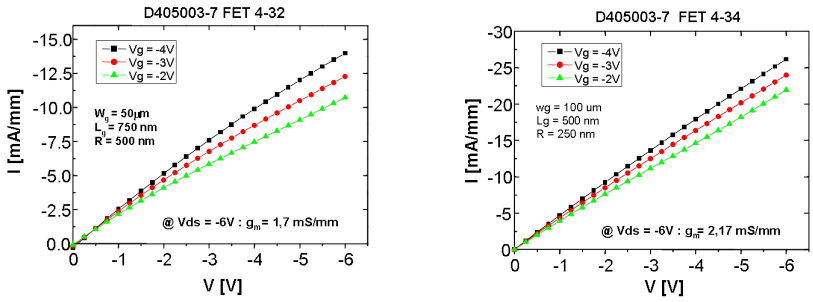


Fig. 10.1: DC characteristic after a further etching cycle for the gate recess was performed.

To improve the characteristics, the Al gate metal was removed and a second etch cycle was initiated. This had indeed improved the modulation of the current. Figure 10.1 shows the result after deposition of the second gate metalization .

The current density is still above $10\,mA/mm$ at R.T. Although saturation could not be reached, the modulation in the linear regime is about $2\,mS/mm$. Pinch off was not yet possible, because of early gate breakdown. Experiments of backside modulation did not give any results because of a missing $pn-$junction in this case of clear CVD substrates without nitrogen doping.

Additional measurements at various temperatures between different Mesa patterns showed no activation of carriers in the buffer layer or substrate. This confirmed, that the substrates were highly insulating.

Based on the DC results, it was decided to perform RF measurements shown in Figure 10.2. Although saturation is not reached, the FETs showed an f_T cut-off frequency of 85 and 110 MHz respectively. The bias levels are also depicted in Figure 10.2

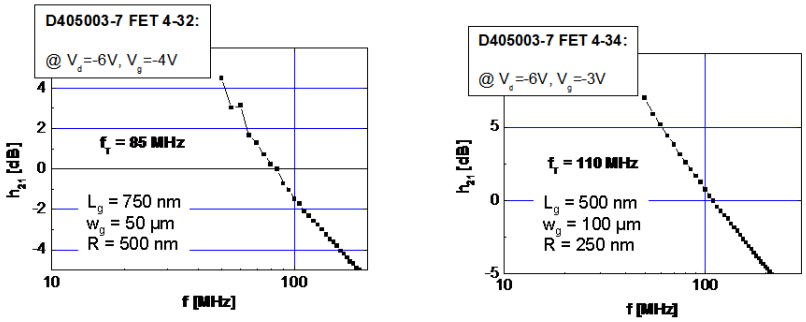


Fig. 10.2: Results of the $S-$ parameter measurement of the double delta transistor along with the extracted f_T and the chosen bias point.(Measured by U. Spitzberg)

10.2 Single delta MISFET

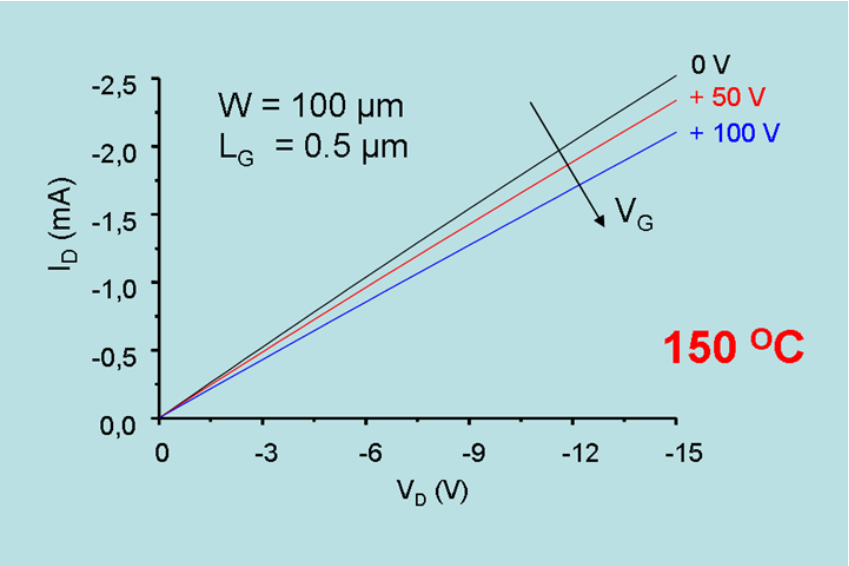


Fig. 10.3: Example of an output characteristic of a single delta channel $MISFET$ showing no saturation behavior with channel current modulation at 150 $°C$.

Many fabrication runs have been successfully completed toward single delta channel transistor devices. A main problem in the beginning was the sharpness of the doping profiles, resulting in a doping tail, which was not yet activated at R.T. but at temperatures higher than $100\,°C$. An example of this problem illustrated with the corresponding output characteristic is shown in Figure 10.3, taken at elevated temperature. Despite of the very high gate voltages which were applied ($100\,V$), the device showed clear modulation behavior, however no saturation. This output characteristic was measured at $150\,°C$ for a gate length device of $500\,nm$ and a gate width of $100\,\mu m$.

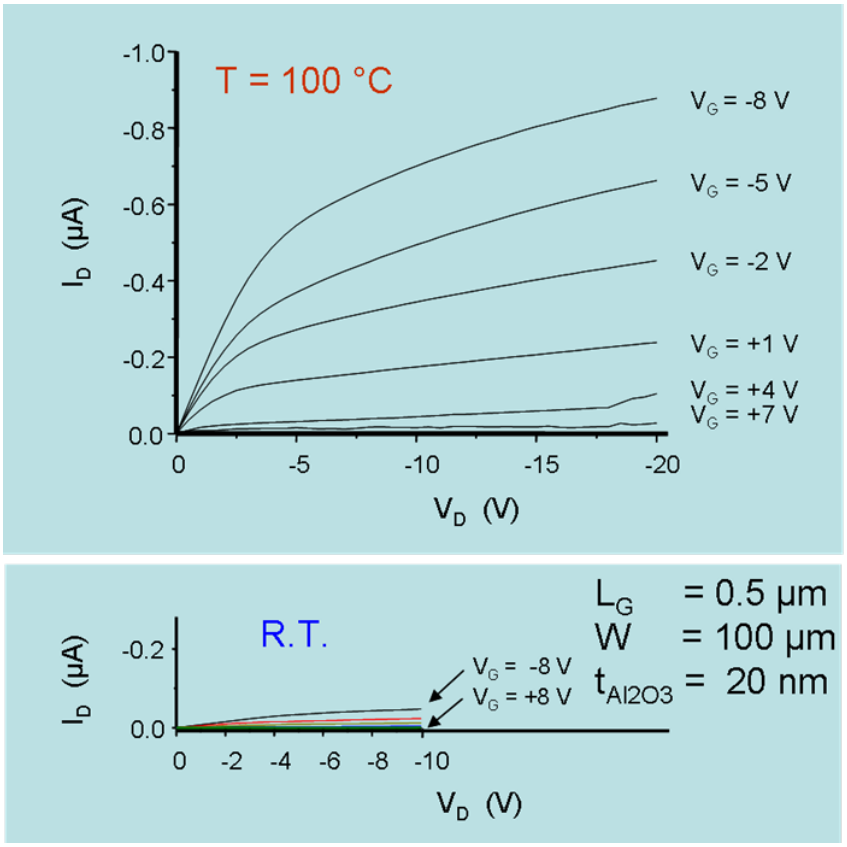


Fig. 10.4: comparison between the output characteristic of a single delta MISFET device at room temperature (bottom) and at $100\,°C$ (top) displayed in the same current and voltage scale.

A single delta MISFET device showed a better saturation than the previous behavior is illustrated in Figure 10.4. Nevertheless, the channel doping profile was also not fully activated at room temperature. The comparison shows that the drain current increased by more than twenty fold, when the temperature increased from R.T. to $100\,°C$. This result can be used to explain the tail activation problem of the doping profile.

In this case, the recess allowed the device to operate in both the enhancement mode (up to $V_g = -8\,V$) as well as in the depletion mode with full pinch off ($V_g = +7\,V$). The gate length of the device was 500 nm and the gate width $100\,\mu m$.

As mentioned in the fabrication section, back etching of the intrinsic layer under the ohmic contact region is usually necessary. In this case, the contact areas were only insufficiently back etched and the behavior of the ohmic contacts was non-linear.

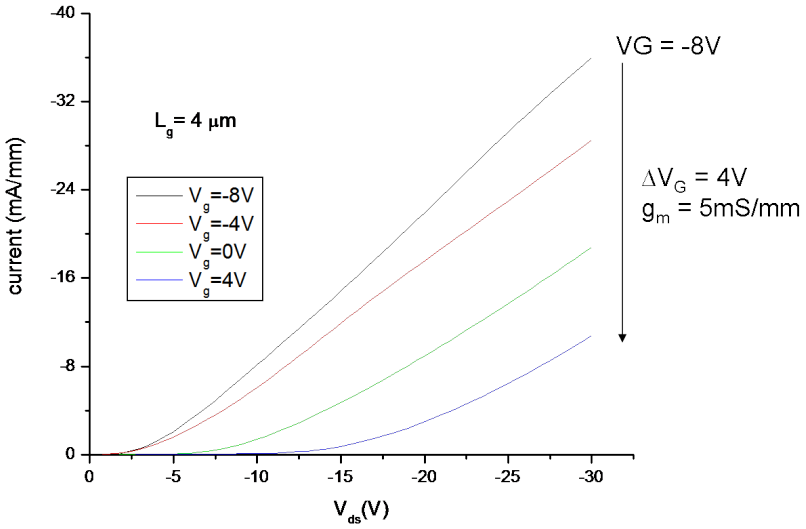


Fig. 10.5: *DC* output characteristic of the simplified MIS single delta transistor.

Figure 10.5 shows the DC output characteristic of the single delta MISFET transistor. In this case the gates are rather large, because optical lithography was used. High current densities in the order of $40\,mA/mm$ could be achieved in this case, however no saturation was reached.

To overcome the problem of the ohmic contacts, an additional transistor fabrication run based on a similar processing routine was started, but this time, further etching of the ohmic contact window was introduced in order to improve the ohmic contact behavior.

Test substrates were used to analyze the carrier profile of the delta-doped layer by capacitance-voltage $C-V$ measurements (in the frame of the abrupt junction approximation) performed using Al Schottky diodes fabricated on layer stacks with only $1\,nm$ cap layer thickness. This thin cap layer enabled measurement part of the doping profile at low bias levels, despite the tunneling leakage associated with such thin barriers. However, the high tunneling leakage current at higher bias levels prevented the realization of FET devices with full channel modulation. The growth parameters of the delta profile were identical to those used in the FET devices. The carrier profile extracted from the $C-V$ measurement in reverse direction ($0\,V < V_{rev} < 2.5\,V$) is shown in Figure 10.6.

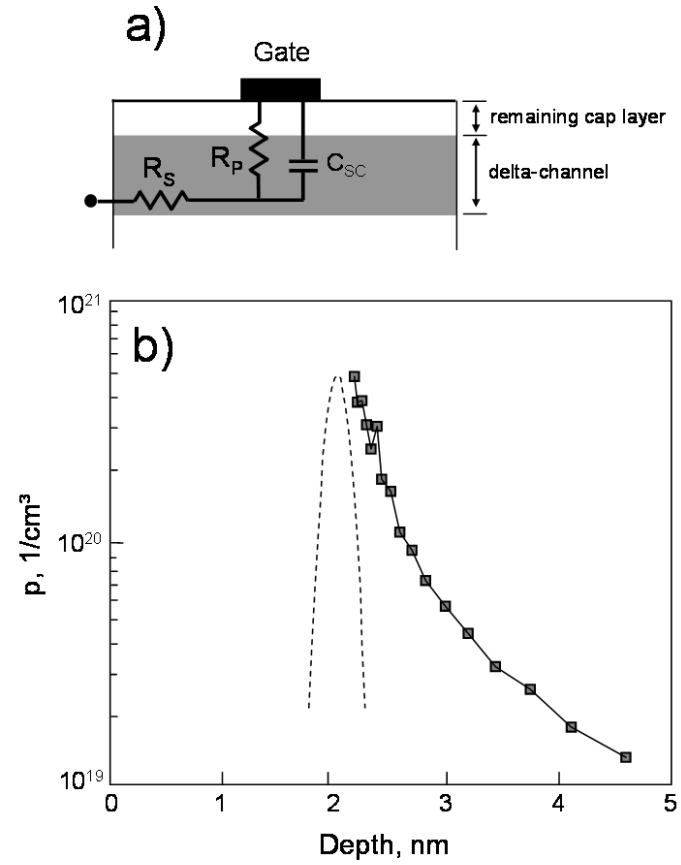


Fig. 10.6: (a) Schematic cross-section of the diode structure and (b) the extracted carrier profile of the boron-doped layer from the $C-V$ measurements at a frequency of $0.5\,MHz$. The solid line shows the theoretical Gaussian profile using the Debye length corresponding to the maximum carrier concentration

The equivalent circuit used to extract the parasitic resistive elements is shown in the insert. The depth of the depletion layer at zero bias is $\approx 2.2\,nm$, with a surface potential barrier of $1.7\,V$ for the oxygen terminated surface. This corresponds to an average doping concentration of this surface-near region of $\approx 2 \times 10^{20}\,cm^{-3}$. The reason for this fact is that this cap layer was grown in-situ in the presence of the boron contamination of the chamber. The boron concentration extracted from the first bias points is $5 \times 10^{20}\,cm^{-3}$, which is close to the peak of the delta profile. The shape of the resolved part of the profile resembles the previously reported profiles of boron doping atoms in layers, grown under nominally identical conditions, measured by elastic recoil detection (ERD). Both measurements suggest that the full activation limit of $10^{20}\,cm^{-3}$ is surpassed in these profiles with a full width at half maximum below $2\,nm$. The modulated sheet charge density of $1.5 \times 10^{13}\,cm^{-2}$ is however only a lower limit for the total delta profile sheet charge density. The carrier pro-

file was compared to the theoretical Gaussian profile calculated for the Debye Length L_D related to a maximum hole concentration p_{max} of $4 \times 10^{20}\, cm^{-3}$ which is $L_D = 0.14\, nm$ (at $300\, K$). The calculated Gaussian profile is depicted by the dotted curve. As the measured profile is still broader than the ideal one carrier flow outside the doping spike cannot be expected yet. Hence, a mobility enhancement of carriers in the $2D-$like channel cannot be expected either. It appears appropriate to estimate a mobility of 20 to $30\, cm^2/Vs$ extracted from combined CV and sheet resistance measurements and Hall measurements of similar samples. This outcome is consistent with previous results as well. Before the recess was etched, the substrates with $25\, nm$ cap layer were used to determine the sheet resistance R_S and the contact resistance R_C by TLM measurements (see Figure 10.7). The value of R_S was about $20.7\, k/square$ at room temperature. Considering a value of the carrier mobility of $20\, cm^2/V sec$, the sheet charge density in the entire layer stack is estimated to $1.5 \times 10^{13}\, cm^{-2}$, which represents the same order of the test wafers without cap. The contact resistance R_C was about $15.6\, \Omega mm$ and the corresponding transfer length L_T $1.1\, \mu m$, yielding a specific contact resistance ρ_C of $1.7 \times 10^{-4}\, cm^{-2}$ inside the recess area.

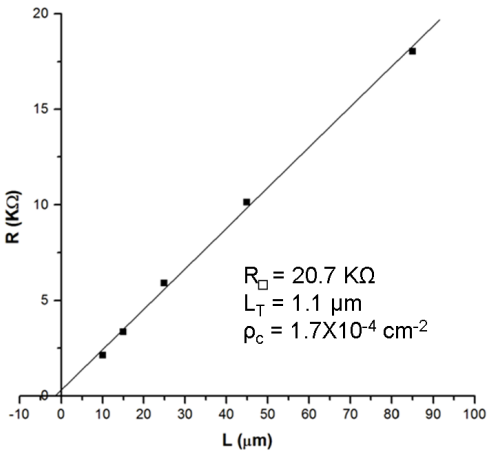


Fig. 10.7: TLM measurement of the channel sheet resistance and the ohmic contact resistances of the boron delta-doped channel with the etched ohmic contacts.

A measurement of the temperature dependence of the channel conductivity confirmed the high peak concentration of boron acceptors in the delta doped profile. The Arrhenius plot of the conductivity between the two ohmic contacts at $10\, V$ (with separation $L = 100\, \mu m$) is shown in Figure 10.8. At this voltage no deviation from the linear characteristics could be observed. The activation energy extracted is $25\, meV$.

Figure 10.9 illustrates the DC output characteristics of a MISFET device with a gate length of $L_G = 0.8\, \mu m$ and a gate width of $25\, \mu m$. Here the ohmic contacts are still slightly nonlinear, because of the difficulty to contact a $1\, nm$ doping profile without residual tunnel barrier after etching of the undoped cap layer. The device operates both in the enhancement

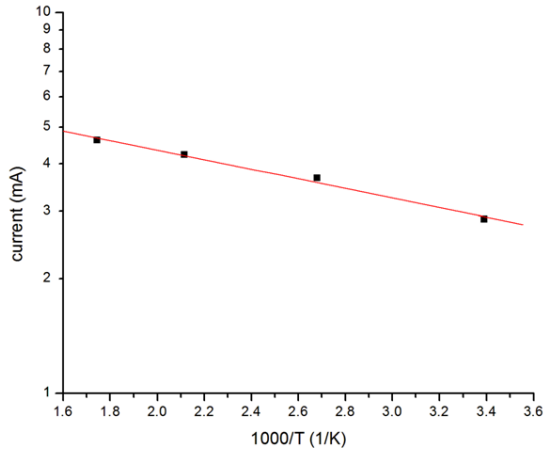


Fig. 10.8: Arrhenius plot of the conductivity of the boron delta-doped profile.

mode (at negative gate bias) and in the depletion mode (at positive gate bias). The maximum drain current is $\approx 30\,mA/mm$ at $V_{gs} = -4\,V$. The channel is pinched-off at $V_{gs} = +5.0\,V$ at small drain bias, neglecting a shunt resistance through the buffer layer with a residual resistance of $\approx R_{SD} = 3\,k\Omega mm$, which is most likely caused by residual boron doping in the buffer layer. Charge injection into the buffer layer at higher drain bias starts to shift the pinch-off voltage to higher values. Thus, the buffer layer properties still limit the maximum drain bias capability.

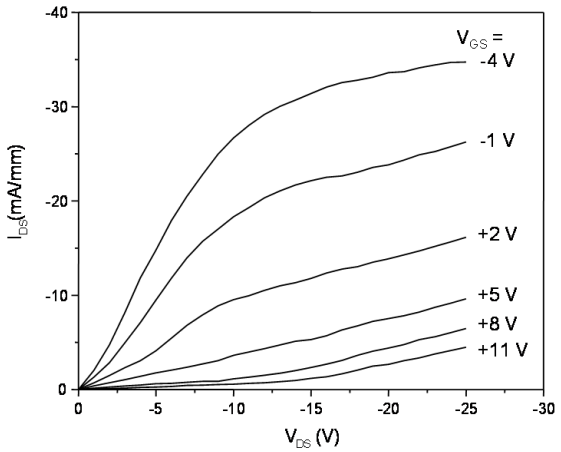


Fig. 10.9: DC output characteristics of a single MISFET structure with the gate length of $0.8\,\mu m$. The measurements are at room temperature

The FET output characteristics were fitted by a MOSFET model with gradual channel approximation, which allows for the series resistances of the source and drain areas R_S and R_D, and also the parasitic shunt resistance R_{SD} between source and drain. The schematic cross section of the FET structure and the DC equivalent circuit are shown in Figure 10.10. Figure 10.10 b depicts the transfer characteristics at $V_{DS} = -15\,V$. The experimental data points have been fitted by the solid line using $R_S = R_D = 110\,\Omega mm$, and $R_{DS} = 3\,k\Omega mm$. The dashed line represents the intrinsic transfer characteristic. The intrinsic FET fitting parameters were: $\mu_p = 20\,cm^2/Vs$, $t_{cap} = 10\,nm$ ($\epsilon = 5.5$) and $t_{Al_2O_3} = 25\,nm$ ($\epsilon = 10$). For the intrinsic gate bias at equilibrium ($V_{GSint} = 0\,V$), corresponding to a built-in Schottky barrier height of $1.7\,V$ (oxygen terminated surface), the sheet charge density for the depletion mode range was calculated to $n_{so} = 0.64 \times 10^{13}\,cm^{-2}$. At the extrinsic forward bias of $-4\,V$, the intrinsic gate bias is $V_{GSint} \approx -1.8\,V$ (in the saturation region). Therefore the Schottky barrier induced channel depletion will be widely removed and the total sheet charge density is now estimated to $0.87 \times 10^{13}\,cm^{-2}$. This means, an additional charge density $0.23 \times 10^{13}\,cm^{-2}$ could be modulated in enhancement mode, which would not have been possible without the recess configuration. This value of total modulated sheet charge density is still less than the total sheet charge density obtained from the sheet resistance measurements before recess etching (which was $1.5 \times 10^{13}\,cm^{-2}$). The difference of $0.6 \times 10^{13}\,cm^{-2}$ may then be used to calculate the average active carrier density in the nominally undoped cap layer, which results in a value of $p = 4 \times 10^{18}\,cm^{-3}$. This value is well in agreement with residual boron doping levels seen in the growth chamber even after an extensive growth interrupt.

First small signal RF characteristics for an FET structure with a gate length of $4\,\mu m$ (different substrate) were obtained. The fabrication routine and epitaxial growth parameters were identical to the device discussed above. The source and drain contacts showed non-ideal ohmic characteristics, emphasizing again the high precision needed in the contact etching step. The calculated RF current gain (H_{21}) and the maximum power gain (MAG) characteristics for the frequency range between $0.1\,GHz$ and $10\,GHz$, are plotted in Figure 10.11. A fact that needs to be taken into account in the extrapolation of the cut-off frequencies, is that the role-off of the gain plots at high frequency is less than the expected $20\,dB/dec$ because of the parasitic elements of the structure. The extrapolation as indicated, results in cut-off frequencies f_T and f_{max} of approximately $1\,GHz$ and $3\,GHz$ respectively. An extraction of the intrinsic values was not possible, due to the nonlinear behavior of the parasitic series resistances.

Until recently it had been impossible to realize a fully operational FET device structure in diamond based on delta doped profiles at room temperature. In this study such a structure has been developed for the first time, which enables both full channel modulation with complete pinch-off and full room temperature carrier activation. The key has been the development of a delta doping growth technique with sub$-nm$ precision and a gate recess technology, again with sub$-nm$ etch control. Although there is only a small number of functional devices yet, first RF data have been obtained and cut-off frequencies in the lower $GHz-$range could be extracted. Despite a gate recess, the devices have still been influenced by parasitic series resistances and a gate dielectric of Al_2O_3 had to be inserted to control the

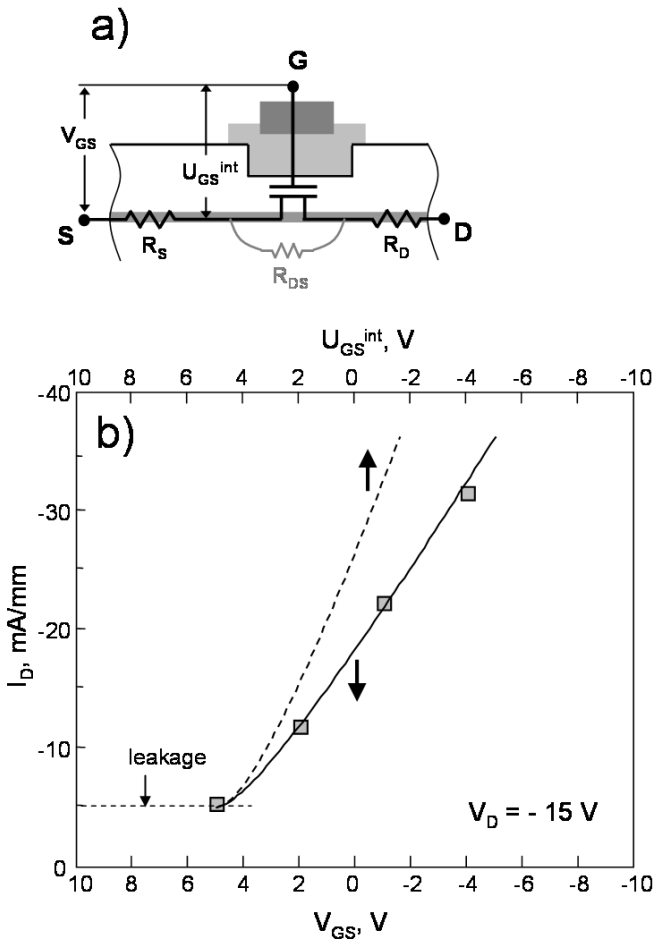


Fig. 10.10: (a) The schematic cross-section of a MISFET and the equivalent circuit showing the parasitic elements (b) transfer characteristics of the device in Figure 10.9 at V_{DS} of $-15\,V$. The corresponding fitting curves for the extrinsic V_{GS} and intrinsic U_{GSint} gate biases are shown by the solid curves.

gate leakage. The mode of operation had been in depletion as well as enhancement, with the enhancement mode being only possible due to the recess configuration. Nevertheless, current levels still remained low due to the low channel carrier mobility. These findings suggest, that the delta doping technology still needs further refinement to obtain acceptor doping profiles, which are essentially steeper than the corresponding Debye tail to take advantage of a $2D-$channel mobility enhancement, while the ultimate goal is a monolayer planar doping.

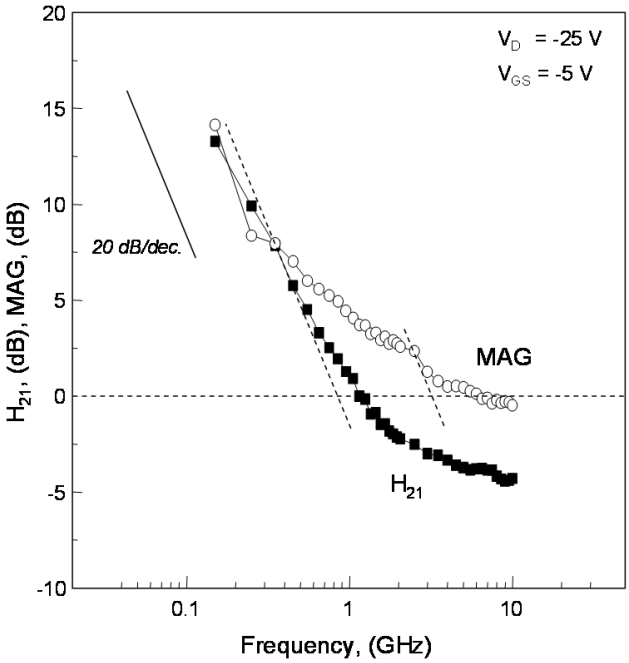


Fig. 10.11: Small signal characteristics of a MISFET device with the gate length $L_g = 4\,\mu m$. The bias point of the RF measurements was the drain bias of $-25\,V$ and the gate bias of $-5\,V$ (Measured by U. Spitzberg and N. Alomary.)

10.3 Single Crystal ISFET results

The output and the transfer characteristics of an ISFET structure in the electrolyte solutions (already discussed in Chapter 8.5) are shown in Figure 10.12. Due to the high n_s and low mobility in the channel, no saturation regime and no pinch off of the FET output characteristics was observed. The maximum gate bias in the enhancement mode and the grain voltage were limited by the onset of $H-$ or $O-$evolution (Figure 10.12 b)). The transfer characteristics showed that the device channel can be modulated by the gate potential and by changing the pH value of the solution. Increase of pH resulted in lower depletion of the surface channel. The shift of the pinch-off voltage ΔV_T between $pH = 1$ and $pH = 13$ was about $0.6\,V$, which corresponds to the variation of about $50\,mV/pH$. Similar pH dependency has been observed for the flat-band potential of $O-$terminated diamond electrodes. Thus, projected variation of the pinch-off voltage with pH was close to the expected Nernstian dependency of $59\,mV/pH$ [7]. This shows that the equilibrium at the $O-$terminated surface is due to the change transfer between the ions in the electrolyte and carbon-oxygen surface groups.

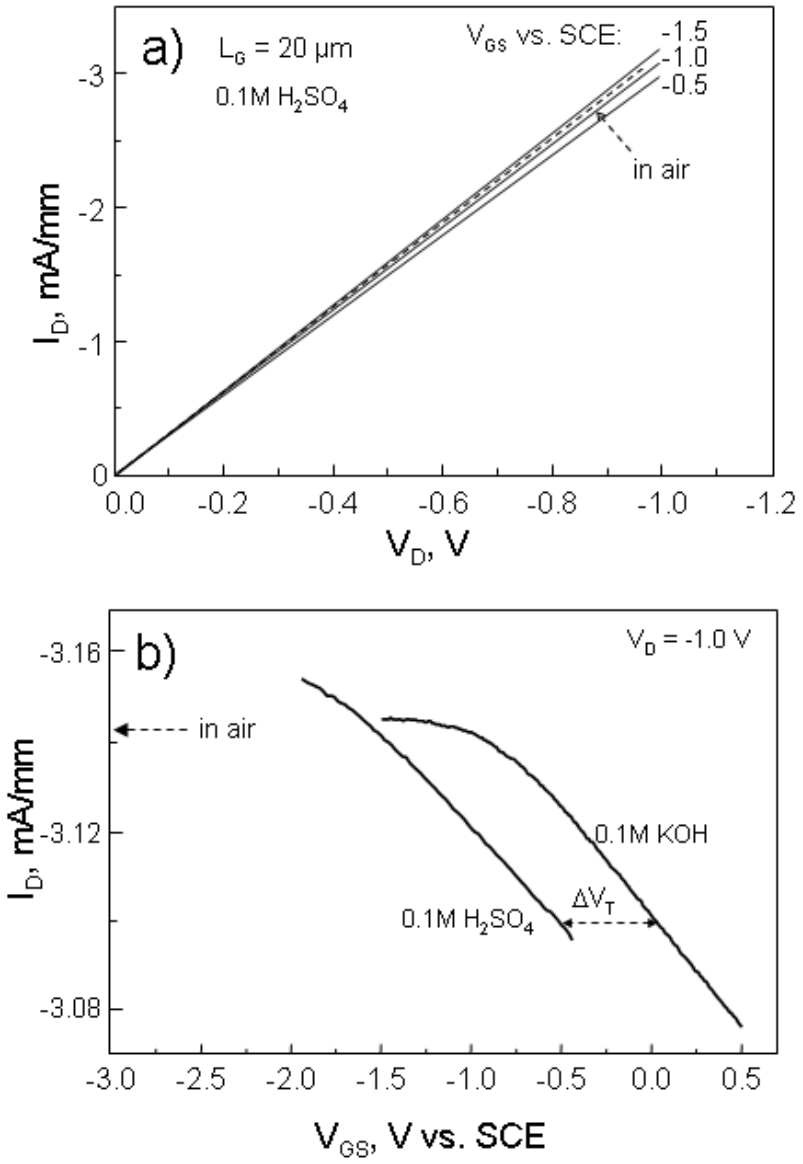


Fig. 10.12: a) The output and b) the transfer characteristics of a micro-$ISFET$ with boron-doped channel and a gate length of $20\,\mu m$. The dashed arrow shows the conductivity in air. [7]

The device characteristics were reproducible and did not degrade after repeated cycling in $0.1M\ H_2SO_4$ and $0.1M\ KOH$ solutions (Figure 10.13). The characteristics also did not degrade after keeping the structure in $0.1M\ KOH$ solution for about $20\,min$. Although the estimated charge density in the ISFET channel was about two times higher than the optimum value (see the discussion above), only one percent of the drain current could be modulated

by changing the gate bias ΔV_G up to $1.5\,V$. To Identify a possible reason for this discrepancy, the ISFET characteristics were compared to those of the diamond electrode with the identical boron-doped surface layer (Figure 10.14). The cyclic voltametry in $0.1M\ H_2SO_4$ solution demonstrated a very wide potential range with negligible electrochemical activity between the $H-$and $O-$evolutions (Figure 10.14 a)). In the $\mu A-$current range the potential window was about $3\,V$. The wide potential window is typical for high-quality diamond electrodes (see chapter 6.1) with a low density of surface defects.

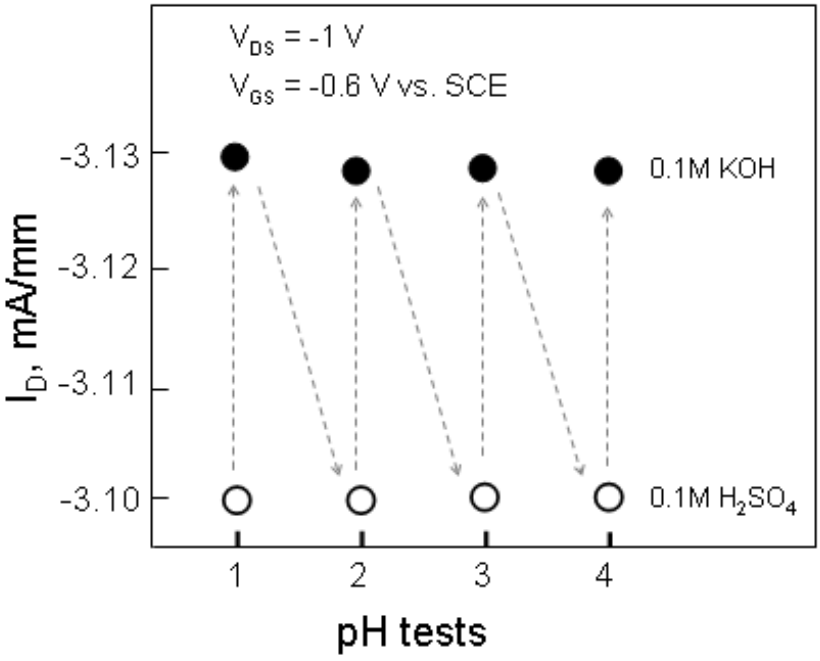


Fig. 10.13: Sequence of pH tests with the ISFET structure in $pH = 1$ and $pH = 13$ electrolytes. the fabrication process and passivation is according to section 8.5

The impedance characteristics of the electrode were recorded in the frequency range from $0.1\,Hz$ to $100\,kHz$. Within the potential window the impedance of the diamond-electrolyte interface could be fitted by a simple RC parallel circuit (Figure 10.14 insert). The value of the parallel resistance R_P varied between 10 to 30 $M\Omega cm^2$, which is typical for a high-quality diamond surface showing no electrochemical activity. The Mott Schottky plot of the parallel capacitance C_p could be fitted by a depletion layer capacitance with a constant doping concentration except for positive potentials close to the onset of the $O-$evolution.

At positive potentials, a small reaction peak was detected close to the onset of the anodic current. The peak was reproducible and did not disappear after many voltammetry scans. A corresponding spike was also seen in the capacitance plot (Figure 10.14 b)). The fitting of the Mott-Schottky plot yielded the projected flat-band potential VFB of about $+8.8\,V$ vs. SCE in $0.1MH_2SO_4$ solution as shown by the arrow in (Figure 10.14 b)). However the origin of this adsorption peak is not clear yet.

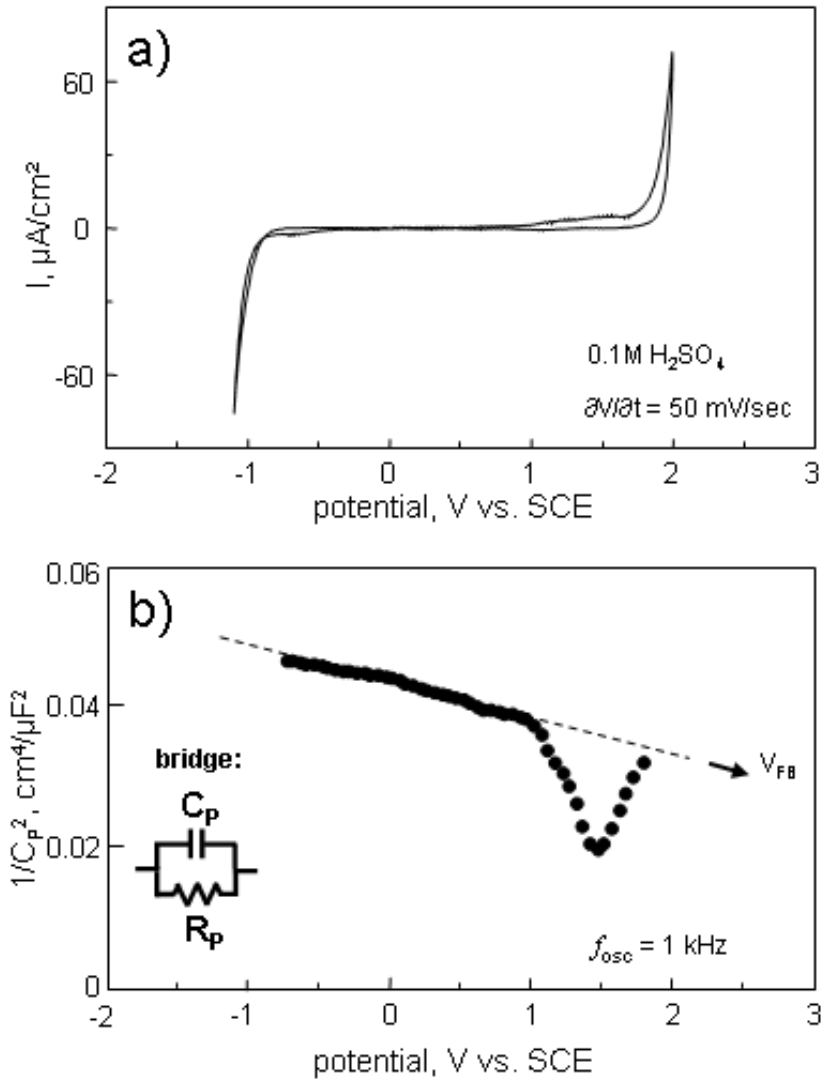


Fig. 10.14: $a)$ Cyclic voltammetry and $b)$ capacitance voltage plot of diamond electrode with the boron delta doped channel in $0.1\,M H_2SO_4$ solution. The voltammogram was recorded after several complete cycles in the electrolyte. The arrow in $b)$ indicates the projected flat band potential V_{FB} of $8.8\,V$.

10.4 P-I-P Transistor Results

The fabrication process for P-I-P devices shown in Figure 10.15 was completed on several samples and DC output characteristics, small signal measurements and $C-V$ measurements were performed. Furthermore, elements of a simple equivalent circuit model of the FET were fitted by using the measured $S-$parameters.

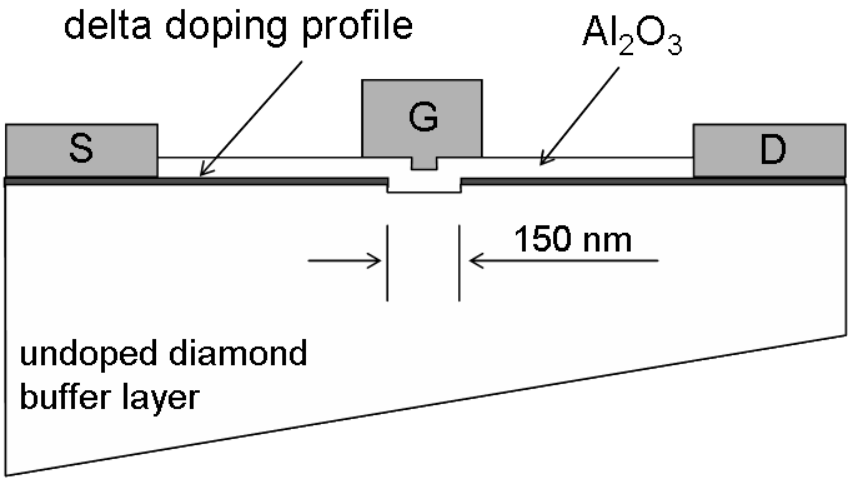


Fig. 10.15: Cross section of a P-I-P transistor device, already discussed in chapter 9.4, with $150\,nm$ channel length. Thickness $Al_2O_3 = 20\,nm$ and recess depth is $5\,nm$

P-I-P transistors were fabricated with a very short channel length of $150\,nm$. The corresponding DC output characteristic is shown in Figure 10.16.

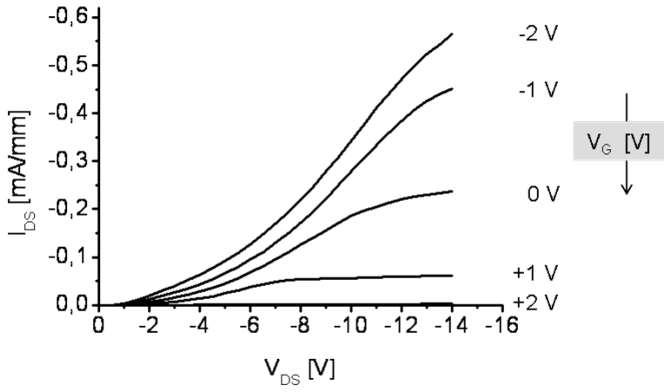


Fig. 10.16: DC characteristics of the P-I-P transistor with the delta layers.

In this case, a maximum current density of $0.6\,mA/mm$ was measured with a maximum transconductance of $0.3\,mS/mm$. The pinch off voltage was $2\,V$ and the gate modulation was possible in both enhancement (negative gate bias) as well as depletion mode (positive gate bias).

To identify the origin of the measured channel current, the output characteristic was plotted in the semi-logarithmic scale and the slope was determined to be 2.0 (Figure 10.17). This super linear characteristic points toward two possible mechanisms. It could be either a space

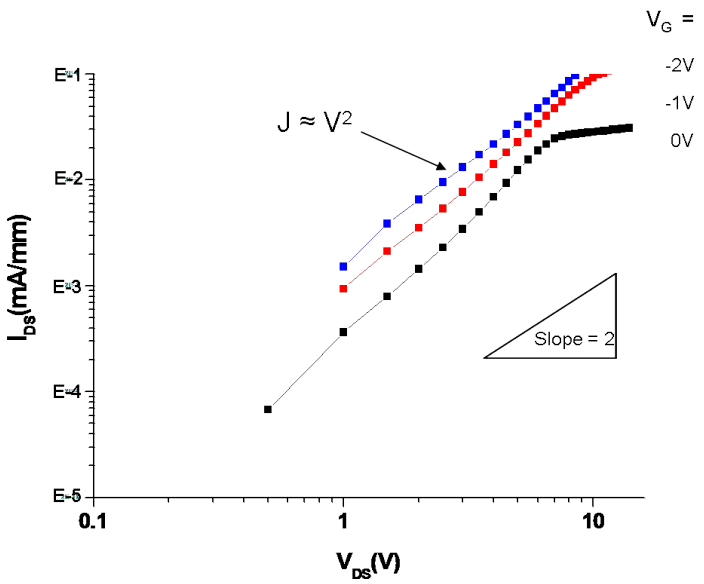


Fig. 10.17: Slope of 2 in a semi-logarithmic scale of the $P-I-P$ output characteristic proving that the measured current might be indeed an injection current.

charge limited current flow as expected, or it could also be an injection characteristic of the source contact and still doping related current flow in the channel.

RF measurements were performed in the frequency range from $50\,MHz$ to $2\,GHz$ to evaluate the cut-off frequencies. As shown in Figure 10.18, a value of $f_T = 70\,MHz$ was extracted at the bias point as indicated. Higher gate voltage resulted in slightly lower f_T values.

A first order MESFET model was used to extract the intrinsic lumped element for small signal device parameters. As can be seen from Figure 10.19, a gate drain feed back circuit had to be introduced for reasonable fitting, which is consistent with the absence of any saturation.

For the gate-source capacitance C_{gs}, a value of about $90\,fF$ for a $50 \times 0.3\,\mu m^2$ was extracted. This value is in agreement with the total estimated gate insulator capacitance of $120\,fF$. The feed back elements were fitted to be $C_{fb} = 41.2\,fF$ and $R_{fb} = 1770\,\Omega$.

Thus, the measured RF results seem to be in qualitative agreement with the device parameters. The channel current is indeed located underneath the gate area and can be modulated by the gate field. It is therefore unlikely that the output current is a parasitic injection phenomenon from a parasitic high field region.

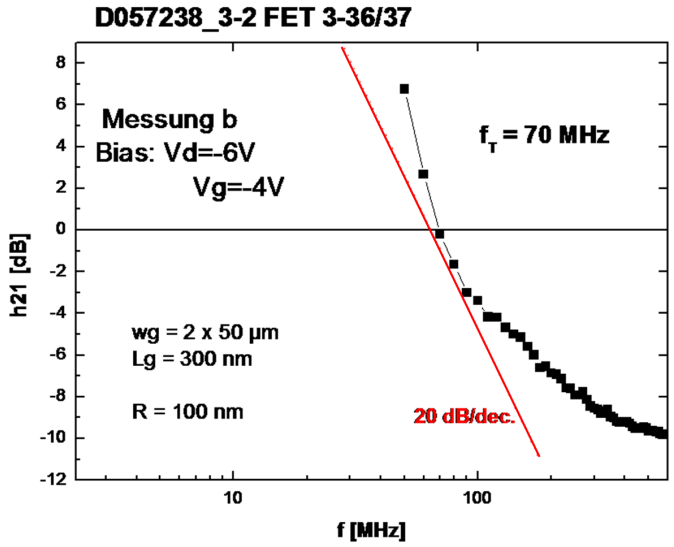


Fig. 10.18: RF measurement of a P-I-P transistor showing an f_T of 70 MHz. (Measured by U. Spitzberg and A. Kaiser)

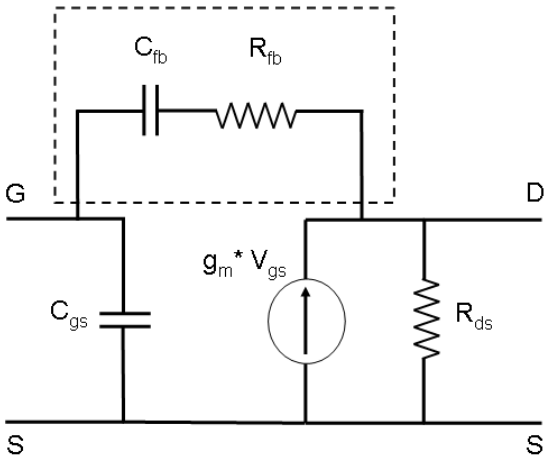


Fig. 10.19: Extracted equivalent circuit from the measured S parameters.

Chapter 11

Conclusion and outlook

In this work, a special growth technique for "Delta Doped Layers" was developed and analyzed in details. The accuracy as well as the reproducibility of this growth technique have been demonstrated.

These delta layers were afterward characterized using many different methods. The electrical measurement showed that these layers have a sheet resistance in the range of $5 - 9\,K\Omega/square$, with full activation of the boron at room temperature, which makes them very convenient to be used as FET channels. They also show a very low surface roughness, with smoothness values in the range of $0.3\,nm$ (RMS).

The carrier profile was also analyzed using capacitance-voltage measurements, with metal contacts as well as in the liquid, and the carrier profiles showed a maximum concentration in the range of $1 \times 10^{20}\,cm^{-3}$ to $6 \times 10^{20}\,cm^{-3}$, which results in a sheet carrier concentration of $1 - 3 \times 10^{13}\,cm^{-2}$. These results also agree with the physical/chemical analysis methods (SIMS, ERD), which showed profiles in the same range.

Using these delta layers either as a channel or as a contact layer, we were able to design P-I-P FET, single delta FET and double delta FET structures. These three designs have also been fabricated and tested, as a proof of concept experiment.

Such FET structures, using a boron delta doped channel, which is fully activated at R.T. has been realized in this project for the first time, which enables both full channel modulation with complete pinch-off and full room temperature carrier activation. Also, first RF data have been obtained and cut-off frequencies in the lower $GHz-$range could be extracted. Despite a gate recess, the devices have still been plagued by parasitic series resistances and a gate dielectric of Al_2O_3 had to be inserted to control the gate leakage. The mode of operation had been in depletion as well as enhancement, with the enhancement mode being only possible due to the recess configuration. Nevertheless, current levels had still been low due to the low channel carrier mobility. Especially this last point indicates that the delta doping technology needs still further refinement to obtain acceptor doping profiles, which are essentially steeper than the corresponding Debye tail to take advantage of a $2D-$channel mobility enhancement, the ultimate goal being monolayer planar doping.

Appendix A

ISFET on NCD using Delta Doping

A.1 Nano Crystalline HFCVD diamond films on 4 inch Silicon wafers

Hot Filament CVD (HFCVD) is one of the two most common techniques for diamond growth, the other one being plasma CVD. The HFCVD technique is based on the heating of metal filaments up to $2000^\circ - 2200^\circ\, C$ in order to break molecular hydrogen and carbon compounds and to form C_yH_x free radicals. These free radicals move toward the substrate by a temperature gradient. On the substrate surface, both diamond (sp^3) and graphite (sp^2) bonds are formed. The graphite bonds are however etched by atomic hydrogen allowing diamond growth on the substrate surface.

The basic structure of a HFCVD reactor includes a set of filaments, the number depending on the size of the substrate, which face the substrate at a distance in a range of $0.5 - 2\, cm$. The material for the filaments must satisfy the following requirements:

- It must be resistant up to $2200^\circ - 2300^\circ\, C$
- Must not react with atomic hydrogen
- Must have a low evaporation coefficient

The two most used materials are Tungsten and Tantalum. Tantalum has a lower evaporation coefficient and is easier to manipulate compared to Tungsten, however the latter is cheaper. The substrate might be heated directly by the filaments or by a separate heating element and reaches usually a temperature in a range of $600^\circ - 900^\circ\, C$. For diamond growth the gas phase has to include a carbon compound like hydrocarbons or alcohol and hydrogen. The most common carbon compound is methane. In some case hydrogen is almost completely replaced by Argon in order to change the growth conditions and the properties of the resulting diamond film. The most used gases for $n-$type and $p-$type doping are N_2, NH_3, B_2H_6, $B(OCH_3)_3$.

The advantages of HFCVD over plasma CVD are the low prices of the system, the easiness and the low prices of large area scaling and a lower etching power (which consent to grow on devices). On the other hand the drawbacks are the contamination from the filament material, lower reproducibility, lower free radical concentration and lower growth rate.

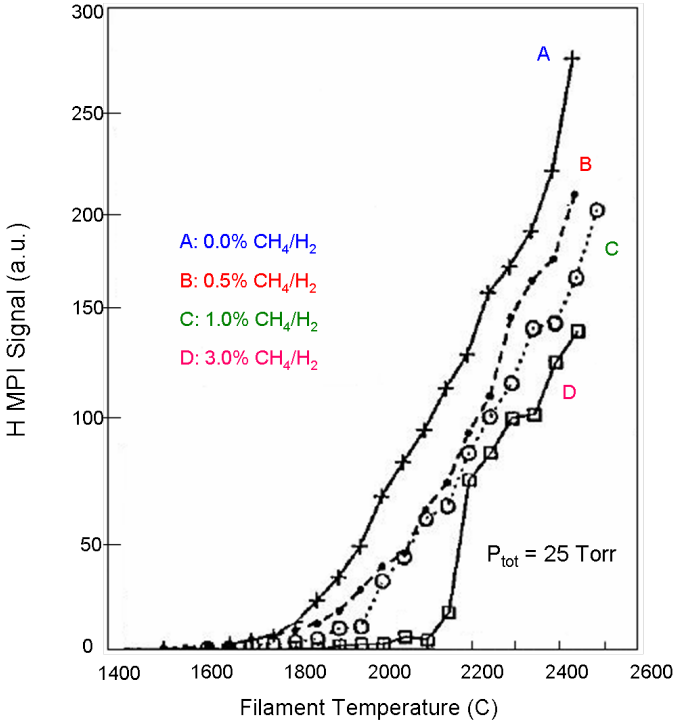


Fig. A.1: H concentration in Hot Filament CVD.After [8].

Diamond growth on foreign substrates requires a nucleation pretreatment which leads to the formation of a carbide like for instance SiC or TiC. The nucleation can be achieved mainly in two ways, with diamond powder or with Bias Enhanced Nucleation (BEN). Diamond powder, with different sizes, is usually diluted in liquid (Isopropanol, Aceton, Methanol...). The sample to be nucleated is then immersed in this solution and an ultrasonic bath is performed for a period of $10\,min$ to $2\,hours$. The advantages of diamond powder nucleation are the more relaxed requirements for the sample which can have any shape and can be either insulating or conductive. Unlike with diamond powder, BEN nucleation can be performed only on the sample surface facing the filaments and requires a conductive substrate. BEN nucleation works with the application of a negative voltage to the substrate in order to accelerate the positive ions produced by the hot filaments. At high temperature, the substrate acts also as source of electrons which are accelerated toward the filaments and enhance the gas ionization. Commonly BEN nucleation in HFCVD includes also a positive Bias electrode placed behind the filaments. The Bias electrode accelerates electrons emitted by the filaments and increases therefore the ion concentration.

The properties of the grown diamond films are determined by the following parameters: filament temperature $1900° - 2200° C$, substrate temperature $(600° - 900° C)$, CVD growth chamber pressure $(0.5 - 5\,kPa)$, filaments-substrate distance $(2 - 3\,mm$ to some $cm)$ and methane/hydrogen ratio $(0.1\,\% - 3\,\%)$.

The grain size of polycrystalline diamond depends on the renucleation process, where the birth of new diamond grains hampers the enlarging of the previous grains avoiding therefore the growth of big diamond crystallites. Renucleation is affected mainly by the methane / hydrogen ratio and by the substrate temperature. As shown in Figure A.1, the atomic hydrogen concentration depends heavily on the methane concentration, due to the fact that higher methane concentration produces more free radicals which can recombine with atomic hydrogen reducing therefore its concentration. The lower atomic hydrogen concentration leads to a lower graphite etching rate and thus to higher diamond renucleation. Large grain sizes in the order of micrometers (polycrystalline diamond) are usually obtained with very low methane concentrations $(0.2\,\% - 0.3\,\%)$, whereas small grain size in the order of tens or hundreds of nanometers (nanocrystalline diamond) are obtained with high methane concentrations $(2\,\% - 3\,\%)$.

A.2 $ISFET$ on Nanocrystalline Diamond

The boron delta doped diamond ISFET fabricated on single crystal diamond proved to be a suitable device for electrochemical applications. Nevertheless it still presents some drawbacks to be solved. First of all the lack of large area substrates for single crystal diamond growth, which limits the fabrication of extended devices like MEAs (multiple electrodes array). Secondly the high surface charge density and the high channel current limit the current modulation and the sensitivity of the device.

On the other hand polycrystalline diamond has already proved to be a suitable material for electrodes in heavy duty treatments and waste water electrolysis. However the lack of delta doping growth techniques prevents the use of such material for FET devices.

Here, we described a new growth technique for delta profiling on polycrystalline diamond using the Plasma CVD process developed for single crystal diamond delta doping. The process parameters have been optimized to the new type of material. Especially the methane pulse time has been increased due to the fact that the growth of polycrystalline diamond resulted to be slower than the growth of single crystal diamond. Moreover the delta doping growth step has been preceded and followed by a pure hydrogen plasma process in order to clean the surface and to remove sp^2 bonds, which would degrade the electrochemical properties of the material.

A.2.1 Delta doped Nanodiamond

The growth process includes two steps. Firstly, a silicon wafer is nucleated with BEN and a thick intrinsic nanodiamond buffer is grown to avoid contacts between the silicon and the electrolyte solution. These processes are performed in a Hot Filament CVD on a 4 inches silicon wafer. The thickness of the intrinsic nanodiamond buffer is in the range of $3-5\,\mu m$. The silicon wafer coated with intrinsic nanodiamond is then cut in $5 \times 10\,mm$ pieces for the boron delta doped nanodiamond growth.

A.2.2 Nanodiamond ISFET fabrication

Before the ISFET fabrication starts, the diamond surface is oxidized by a $2-$steps treatment, oxygen plasma for 2 minutes and wet chemical oxidation in chromium sulphuric acid for 10 minutes. The ISFET fabrication consisted of 3 steps:

- Firstly the MESA etching by RIE (Reactive Ion Etching) in oxygen plasma
- Secondly the metal contacts deposition
- Finally the device encapsulation in PTFE (Teflon)

Figure A.2 shows the complete ISFET ready to be tested.

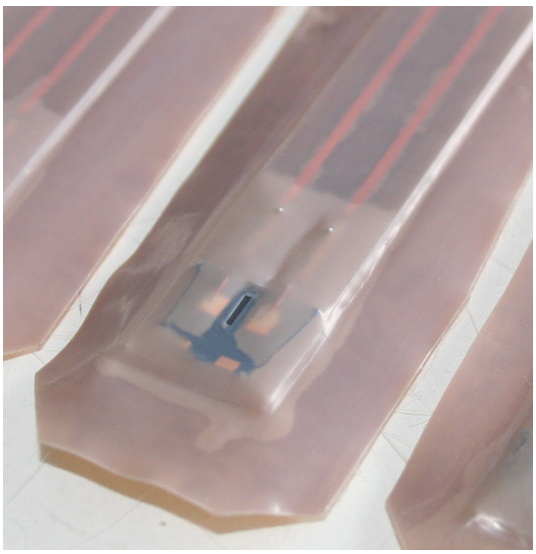


Fig. A.2: Photograph of fabricated ISFET

Figure A.3 shows the cross section sketch of the nanodiamond ISFET with the experimental setup for the electrochemical testing. The diamond surface is in direct contact with the electrolyte, which allows the device to work in both amperometric and potentiometric regimes.

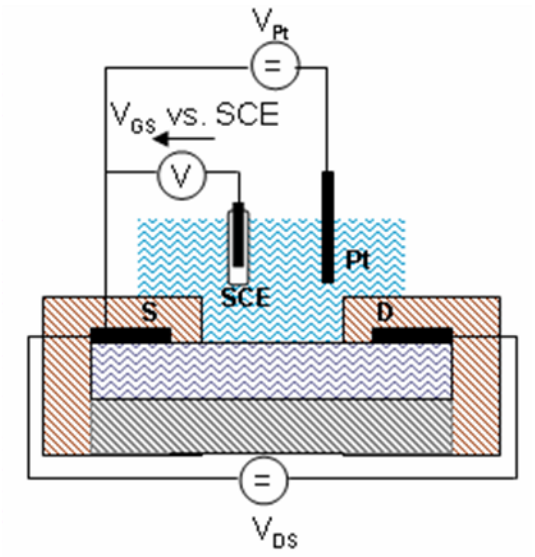


Fig. A.3: Cross section Sketch of the ISFET

A.3 Nano Crystalline ISFET Results

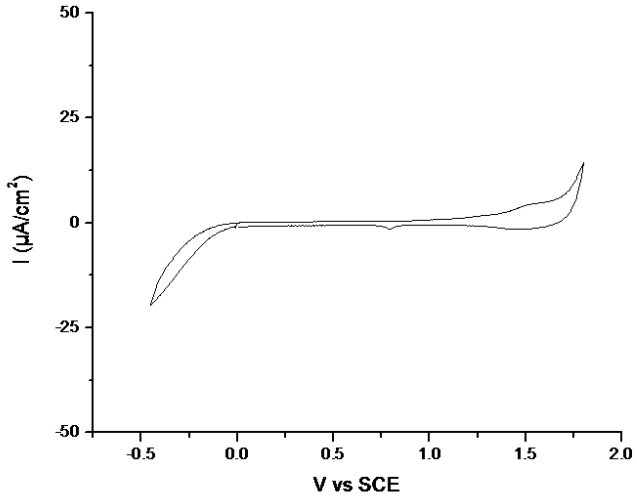


Fig. A.4: Cyclic voltammetry of the $ISFET01221$

Sample 01221-4 is fabricated as described in the previous section. The channel length is $\approx 2\,mm$, the channel width $\approx 2\,mm$ and the gate length $300\,\mu m$. Figure A.4 shows the cyclic voltammetry of the diamond channel surface; a comparison with the cyclic voltammetry of the delta doped single crystal diamond reveals a narrower window and a higher background current. These effects are due to the presence of grain boundaries at the diamond surface. The grain boundaries are formed by various carbon bonds and act as defects that degrade the diamond potential window.

Figure A.5 shows the output characteristic of this ISFET device. The drain-source current modulation is clearly observable. Figure A.6 shows the transfer characteristic of the nanodiamond ISFET, where the linear response of drain-source current versus the gate voltage is clearly noticeable. The overlapping lines represent different measurements performed over time. As one can see, the device proves to be very stable.

In Figure A.7 are shown measurement cycles from pH 1 to pH 13 at a fixed V_{DS}, again the current results to be stable. The pH sensitivity of the nanodiamond ISFET device resulted to be lower than the theoretical limit of $59\,mV/pH$. This fact is due mainly on two factors.

Firstly in ISFET configuration the voltage applied to the diamond surface is not constant along the whole channel but drops from source to drain; this means that the potential between the gate electrode and the diamond surface is not constant on the channel. Secondly, the pH sensitivity can be affected by the presence on the surface of various carbon phases which may have a different response in electrolyte solution.

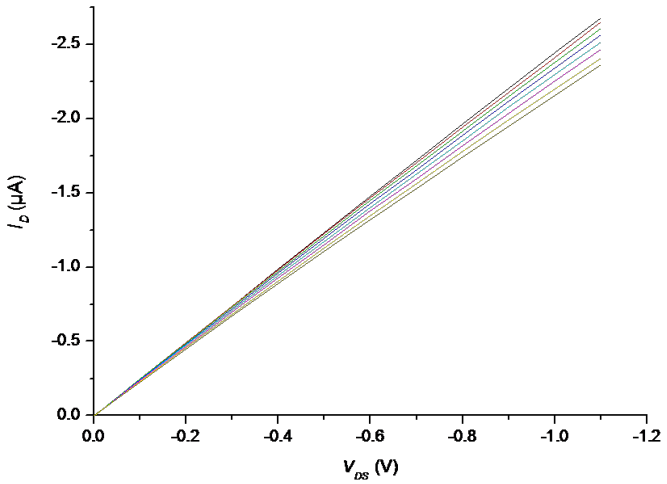


Fig. A.5: Output characteristic of $ISFET01221$

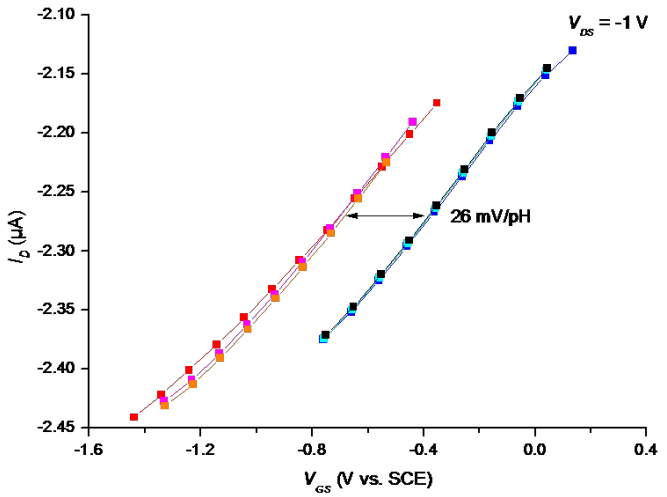


Fig. A.6: Transfer characteristic of $ISFET01221$ with multiple measurements for reproducibility purposes.

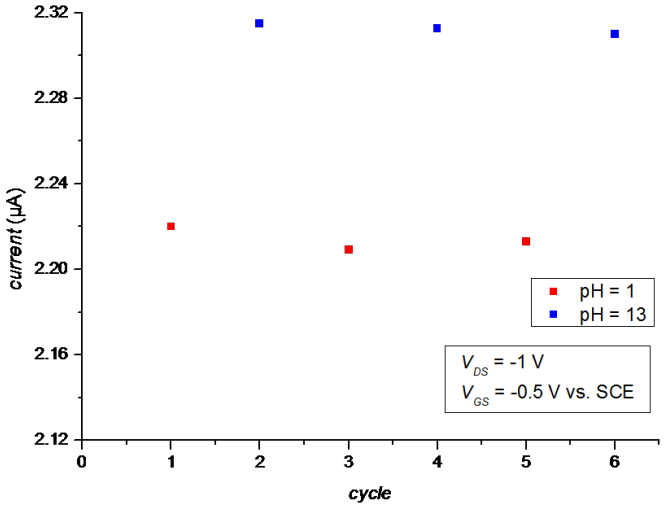


Fig. A.7: Stability over cycles of $ISFET01221$

A.4 Conclusion for the ISFET

A new $ISFET$ structure is fabricated using a boron delta doped nanodiamond channel and oxygen termination. Due to the high sheet charge density the saturation regime is not reached, but the device worked in the linear regime showing a current modulation in the range of $10 - 15\,\%$ with a variation of the gate voltage within the potential window. The device proved to be stable over time and after strong anodic treatments.
(The content of the Appendix A was written with the cooperation of Mr. Michele Dipalo and Dr. Klemens Janischowsky [154, 39], Institute of Electron Devices and Circuits, Ulm University)

Appendix B

Transmission Electron Microscopy Study

B.0.1 Sample Preparation

It is extremely difficult to prepare TEM samples and preserve the surface at the same time, since diamond is a very hard material. The method of choice in this case is a Focused Ion Beam (FIB) technique. This Appendix B was written with the cooperation of Dr. Andrey Chuvilin, Central Facility of Electron Microscopy, Electron Microscopy Group of Materials Science, Ulm University.

The FIB sample preparation included the following steps:

1. Gold deposition for surface conductivity and protection
2. $E-$beam deposition of Pt in the FIB chamber for surface protection at the location of future lamellae
3. $Ga-$ion beam deposition of Pt for surface protection, target thickness of Pt is $\approx 0.2 - 0.5\,\mu m$
4. Cutting of trenches both sides of the future lamellae, the thickness of the lamellae at this step is $\approx\ 2\,\mu m$

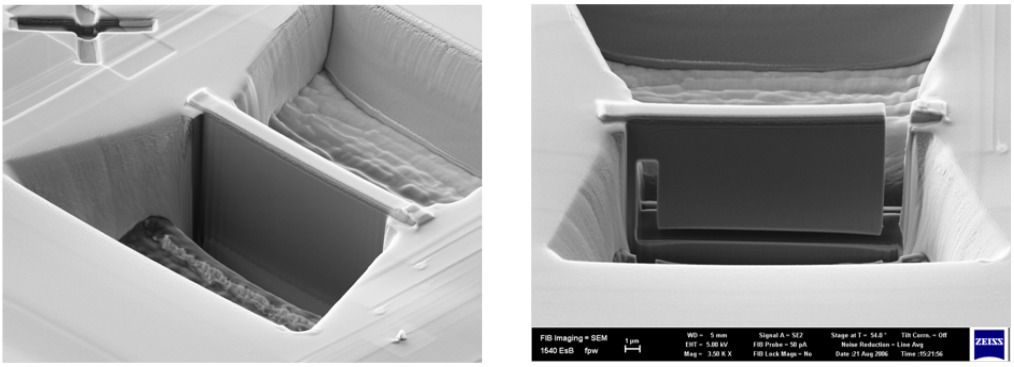


Fig. B.1: Sample after steps 4 and 5

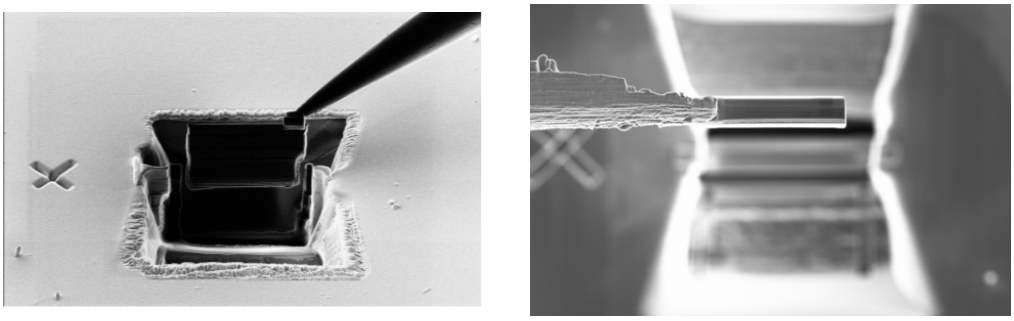


Fig. B.2: Lamellae at step 7 (side view and top view)

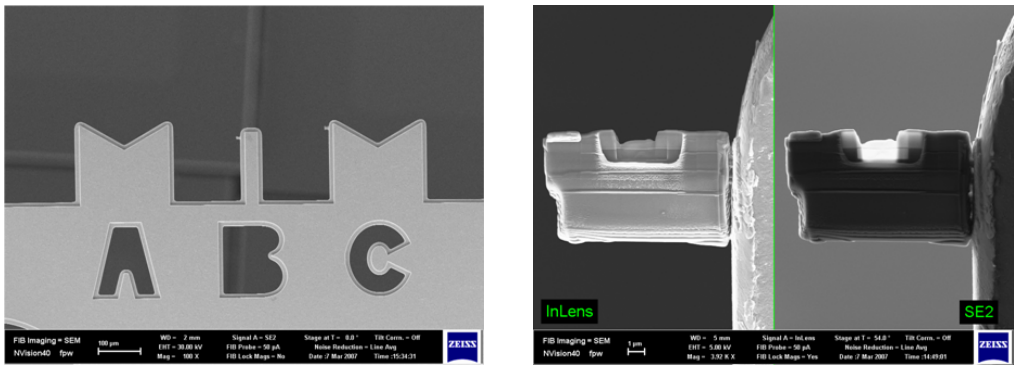


Fig. B.3: Two lamellae attached to the grid (left), view of lamellae after step 9 in secondary and back scattered electrons.

5. Undercutting of the lamellae from the sides and from the bottom
6. Advancing micro manipulator to the lamellae and binding it with Pt deposition
7. Cutting the lamellae off and lifting it with micro manipulator
8. Binding the lamellae to the special grid with Pt deposition and cutting off the micro manipulator
9. Final thinning and polishing the lamellae, target thickness is $100 - 200\,nm$.

In addition to the FIB preparation, further thinning of the samples was attempted (optimum thickness for $EFTEM$ and $HRTEM$ is below $50\,nm$) and amorphous layers that had been produced during ion cutting were removed. Conventional (not focused) ion beam milling with Ar was applied at the variety of accelerating voltages from $4\,KV$ to $0.5\,KV$, as well as a low energy Ar/O plasma.

B.0.2 TEM Study

This TEM Study section was written under the supervision of Prof. Dr. Ute Kaiser and Dr. Andrey Chuvilin, Central Facility of Electron Microscopy, Electron Microscopy Group of

Materials Science, Ulm University. The samples were investigated with four TEM methods: Conventional TEM ($CTEM$), High Resolution TEM ($HRTEM$), Scanning TEM ($STEM$) and Energy Filtered TEM ($EFTEM$). Electron Energy Loss Spectroscopy ($EELS$) was applied as well.

$CTEM$ gives information about the morphology of the sample and imperfections of the structure.

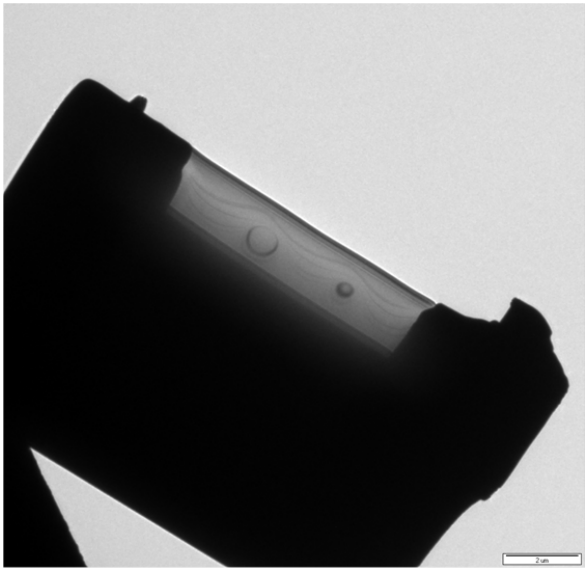


Fig. B.4: Lamellae made for CTEM.(Graph taken by Dr. Andrey Chuvilin)

$HRTEM$ directly resolves the atomic structure and can thus be used, for example, to analyze locally inter-plane distances. Unfortunately, for the case of the samples under investigation, an expected variation of inter-plane distances due to boron doping is below the detection limit. So $HRTEM$ images currently serve for illustration only.

$STEM$ utilizes a contrast, which is strongly dependent on the atomic number ($Z-$contrast, dependence is as $Z^{1.6}$). Thus, composition variations in the sample can be visualized. Nevertheless it is highly improbable that this method can detect the thinly spread boron concentration.

$EFTEM$, which is particularly adapted for light elements, defines detection limits by noise (acquisition time, amorphous layer) and by sample thickness (the thinner the better). Detection of $1\,\%$ impurity would be already a challenging task.

$EELS$ allows detection of particular elements by their signature (absorption edge) in loss spectra.

Figure B.4 shows TEM lamellae as seen in $CTEM$. Dark regions correspond to thick parts, brights to vacuum, the region of interest is the semitransparent window in the middle. Wavy and circular contrast on the lamellae reflects the bending of the sample, probably because of amorphization of the surface during ion milling.

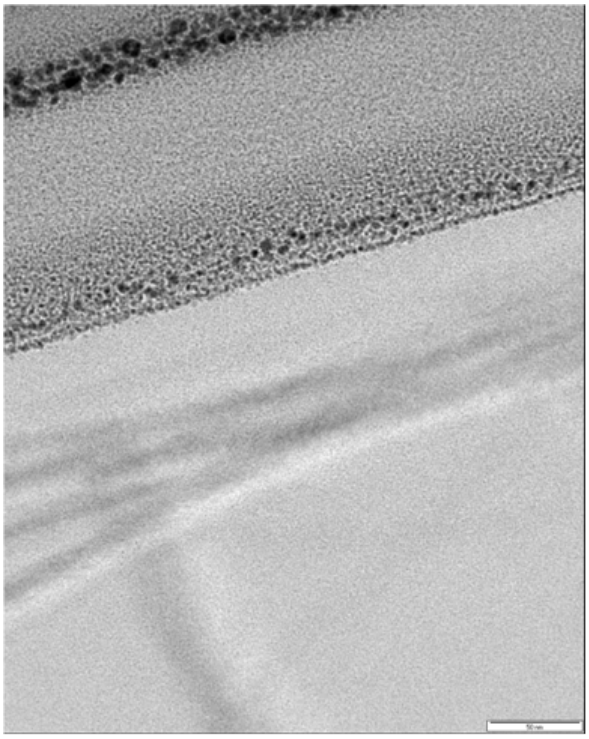


Fig. B.5: Near surface region.(Graph taken by Dr. Andrey Chuvilin)

Figure B.5 shows the surface region of the sample. The spotty contrast over the surface is a protection multilayer consisting of Au, C and Pt. The subsurface structure is preserved by sample preparation, though there is no particular contrast visible, which could be attributed to $B-$doped layers. Bright-dark contours on the crystal are due to diffraction contrast.

Figure B.6 shows the effect of Ar ion milling on the sample. Normally, a treatment with low voltage ion beam removes the surface amorphous layer and significantly improves the sample quality. In the case of diamond sample, it caused a migration of amorphous material over the surface and its coalescence in the form of islands.

Figure B.7 represents the same sample as is seen by $STEM$. The bright horizontal line near the top of the image depicts the surface. This bright line corresponds to the dark damaged surface region visible in $CTEM$. The amount of brightness in $STEM$ illustrates that in addition to the damage there is an accumulation with heavy elements, most probably Ga, which penetrated through the poor protection layer and which was implanted during FIB sample preparation. Moreover, there is a weak horizontal line at the depth $\approx 150\,nm$ below the surface, which relates to some interface boundary enriched by elements heavier than carbon.

Figure B.8 shows an $EELS$ spectra obtained from the narrow region near the surface. The strong carbon edge demonstrates the near-edge structure specific for diamond. There are no signs of a $B-$edge, which may have two reasons: Either, the low concentration of B, com-

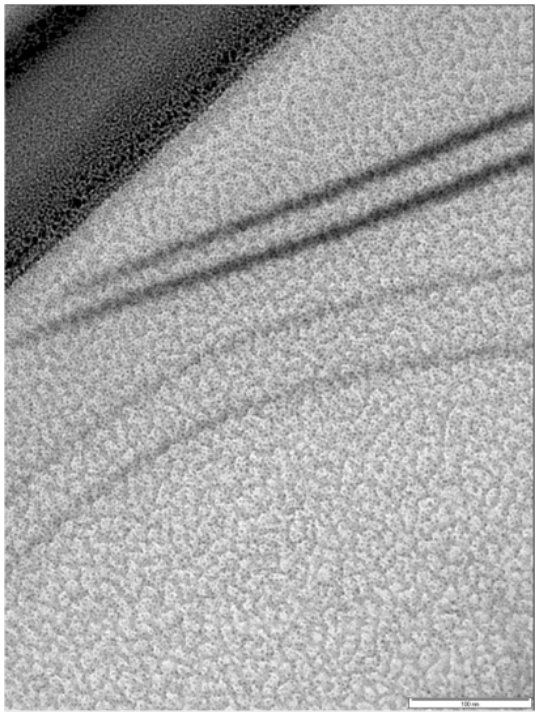


Fig. B.6: The same sample after Ar ion "cleaning". (Graph taken by Dr. Andrey Chuvilin)

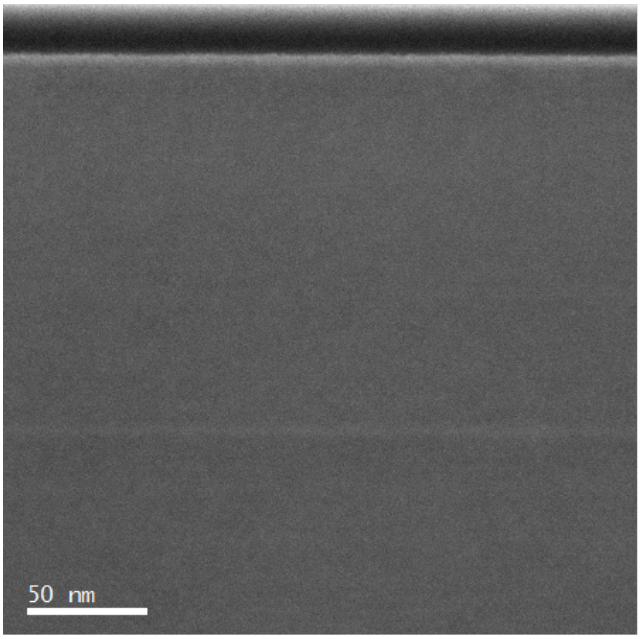


Fig. B.7: Near surface region in $STEM$. (Graph taken by Dr. Andrey Chuvilin)

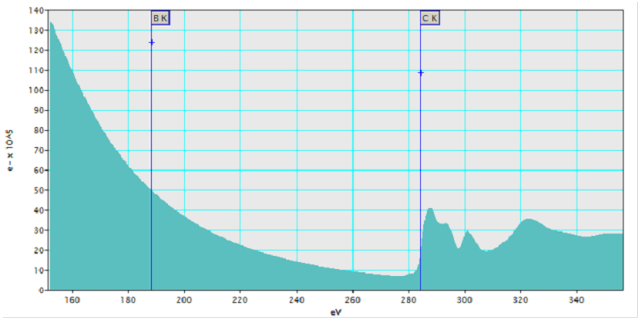


Fig. B.8: $EELS$ spectrum of the subsurface region.(spectrum analyzed by Dr. Andrey Chuvilin)

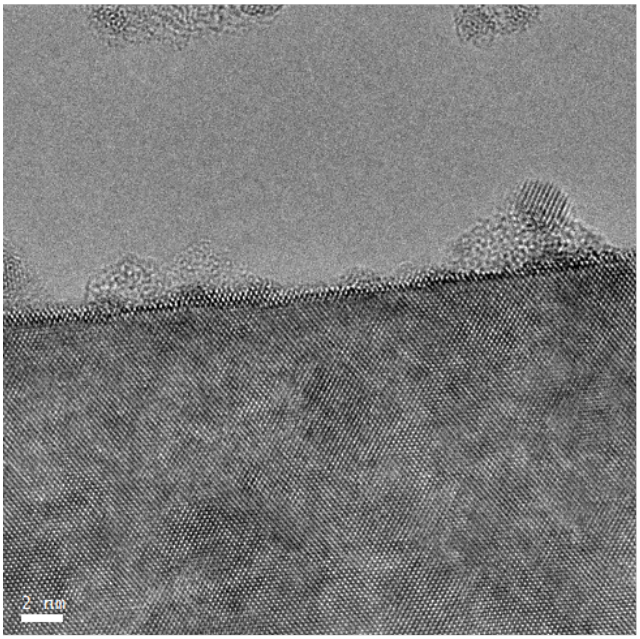


Fig. B.9: High resolution image of the surface.(Graph taken by Dr. Andrey Chuvilin)

bined with a relatively large sample thickness ($\approx 230\,nm$) renders the $EELS$ resolution insufficient for dopant detection; or the surface region was damaged during preparation and thus the thin doped layer was destroyed.

The surface of two other samples was protected by sequential deposition of multiple layers. As the high resolution image of the near surface region in Figure B.9 shows, no damage can be found on the atomic level. The protection layer was detached for some tens of nm from the surface (seen a bit at the top of the picture) during transportation.

But there is still no Boron-edge in the $EELS$ spectrum as seen from Figure B.10. A B elemental map obtained by $EFTEM$ shows no indication for any layered structure either, as seen from Figure B.11. So that any signal can be considered as noise.

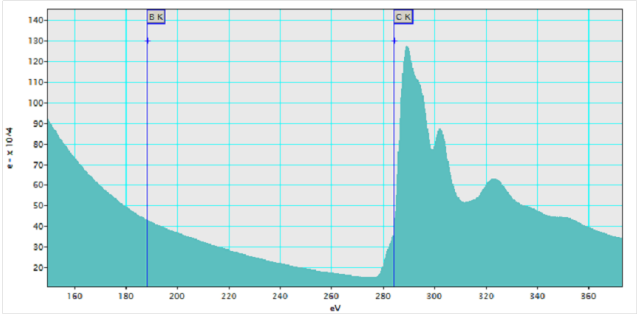


Fig. B.10: EELS spectrum of the subsurface region.(Graph taken by Dr. Andrey Chuvilin)

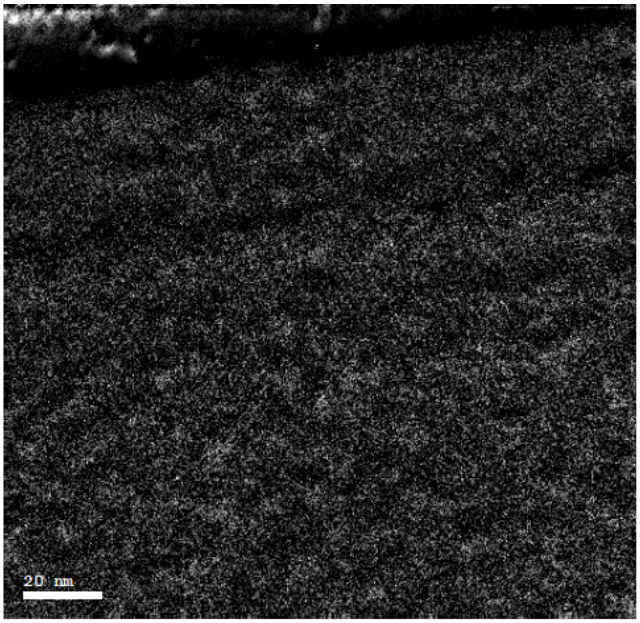


Fig. B.11: B $EELS$ map of near surface region. Bright spots in the up-left corner correspond to the protection layer.(Graph taken by Dr. Andrey Chuvilin)

In conclusion, it can be stated that the classical approach of elemental mapping and trace elements detection did not generate any significant results for the case of a B delta doped profile. Presumably, the concentration of B is too low and the signal is hidden in the noise floor. The most significant sources of noise are the thickness of the sample and amorphous layer produced by FIB sample preparation, while the preparation of diamond is of course difficult. This study seems to be a crucial example for the TEM mapping of B in diamond (i.e. there are strong reasons to continue TEM investigations). In order to clarify the physical limits of TEM for such a material system, additional methodological studies should be prepared. The directions of such investigations have been suggested to be:

- Evaluate theoretically the expected level of the EELS signal and estimate the experimental routes to achieve a noise level lower than the signal amplitude;
- Develop a sample preparation method to produce thin and amorphous free diamond samples

Appendix C

Technological Processes

In this Appendix, all the technological processes which were used in the FET fabrication will be described in details, namely:

- Samples Cleaning Process
- Growth Parameters
- Dry Etching Process
- Optical Lithography Process
- E-Beam Lithography Process
- Oxygen Termination of the diamond surface
- Rapid Thermal Annealing of the Ohmic contacts

C.1 Samples Cleaning Process

Tab. C.1: Procedure for samples cleaning before any other technological step.

Bath tub with Solution	Time (min)	Temperature ($^{\circ}C$)
HF (40%)	2	$R.T.$
H_2O_2 + $2H_2SO_4$	10	75
H_2O_2 + NH_4OH + $5H_2O$	10	75
H_2O_2 + HCL + $5H_2O$	10	75

C.2 Growth Parameters

Tab. C.2: Growth procedure for MPCVD samples used in the fabrication of surface channel $FETs$

Step	H_2 flow (sccm)	CH_4 flow (sccm)	Pressure (Torr)	Temperature ($^\circ C$)	Power (W)	Time (min)
Pretreatment	200	-	30	650	700	5
Diamond growth	200	1.5	30	650	700	15
H-termination	200	-	30	650	700	10
Cooling	200	-	30	R.T.	0	40

C.3 Dry Etching Process

Tab. C.3: Plasma Dry Etching Process used for MESA etching as well as for recess etching.

Ar flow	O_2 flow	Bias Voltage	RF Power	Pressure	Etching Rate
$17.6\,SCCM$	$1.76\,SCCM$	$80\,V$	$25\,W$	$110\,mTorr$	$1\,nm/min$

C.4 Optical Lithography Process

Tab. C.4: Optical lithography process for MESA etching.

Photoresist	Spinning	Backing	Illumination	Development
$AZ5214E$	60 sec at 6000 RPM	90 sec at 100 $^\circ C$	7 sec at 21 W	$AZ726MIF$ for 35 sec

Tab. C.5: Optical lithography process for Lift off process of the ohmic contacts.

	Spinning	Backing	Illumination	Development
$LOR7B$ lower Photoresist	60 sec at 6000 RPM	5 min at 180 $^\circ C$	–	–
$AZ5214E$ upper Photoresist	60 sec at 6000 RPM	90 sec at 100 $^\circ C$	7 sec at 21 W	$AZ726MIF$ for 35 sec

C.5 E-Beam Lithography Process

Tab. C.6: E-Beam lithography process for recess etching.

Photoresist	Spinning	Backing
$PMMA950K$ pure	60 sec at 4000 RPM	5 min at 180 $^\circ C$

Tab. C.7: E-Beam lithography process for gate lift off.

Photoresist	Spinning	Backing
$PMMA/MA33\,\%$ lower E-Beam resist	60 sec at 3000 RPM	5 min at 180 $^\circ C$
$PMMA950K2:1$ upper E-Beam resist	60 sec at 6000 RPM	5 min at 180 $^\circ C$

C.6 Oxygen Termination of the diamond surface

Tab. C.8: Oxygen Plasma Termination of the diamond surface, μ etch machine.

Power	O_2 flux	Pressure	Time
$100\,Watt$	$6\,SCCM$	$100\,mTorr$	$3\,min$

Tab. C.9: Wet chemical Oxygen Termination of the diamond surface.

Bath Tub of	Temperature	Time
$1\,H_2O_2 + 2\,H_2SO_4$	$75\,^\circ C$	$20\,min$

C.7 Rapid Thermal Annealing of the Ohmic contacts

Tab. C.10: Rapid Thermal Annealing of the Ohmic contacts.

Atmosphere of	Temperature	Time
Nitrogen	$650\,^\circ C$	$1\,min$

C.8 Mobility Measurement

A Hall structure on the chip helped measuring mobilities. The chip was embedded into a PCB holder and the structure was successfully bonded to it. Therefore, the high temperature ohmic contacts which are normally used, must have a very good adhesion with the highly boron delta doped layer.
Figure C.1 illustrates an equal measurement setup with the chip in an etched tub and the PCB carrier with its bonded gold wire connections. In this case, a magnetic field is applied perpendicular to the plane of the sample.
Typical mobilities measured, were in the range of $20-30\,cm^2/Vs$ at a total carrier concentration of more than $9.10^{19}\,cm^{-3}$. Since this is still below ideal values, as simulated with Silvaco tool, it is clear that a mobility enhancement has indeed not yet been achieved.

Figure C.2 shows the overall processing sequence with all possible iterations.

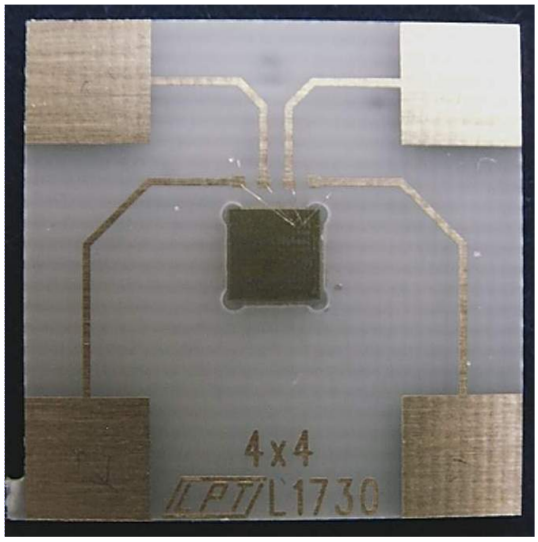


Fig. C.1: PCB design suitable for the mobility measurement using the Hall and Van der Pauw technique.

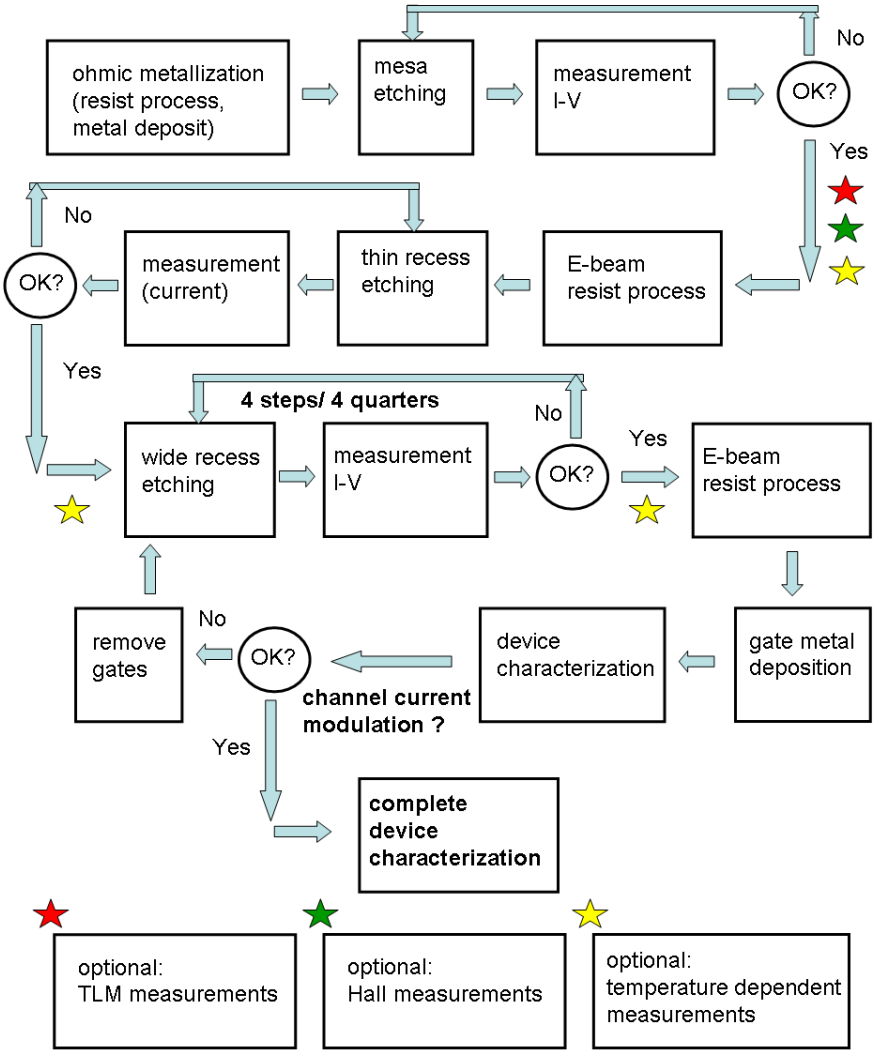


Fig. C.2: A complete fabrication cycle of a double delta FET device.

Appendix D

List of Symbols

a	Lattice Constant	9
AFM	Atomic Force Microscopy	2
α	Growth speed ration between [100] and [111] orientations	22
BFM	Baliga figure of merit	11
BH_x	Radicals containing Borong and Hydrogen	26
β	Growth speed ration between [100] and [110] orientations	22
CVD	Chemical Vapor Deposition	5
C_0	Gate Channel Capacitance	58
C_P	Specific heat capacity	12
C_{gs}	Gate source capacitance	35
C_{SC}	Space charge Capacitance	35
C_{dl}	double layer Capacitance	35
χ	Electron Affinity of the semiconductor	30
d_i	thickness of the layer between gate and channel	58
ERD	Elastic Recoil Detection	2
$E6$	Element Six Ltd.	1
E_{BR}	Breakdown electric field	12
E_G	Band gap energy	12
E_C	Conduction band	26
E_V	Valence band	26
E_F	Fermi Level	32
E_A	Activation Energy	32
E_{crit}	Critical field between const. mobility and const. velocity	58
ϵ_r	Relative dielectric constant	12
ϵ_d	Diamond dielectric constant	12
fcc	face-centered cubic	10
f_T	Cut-off Frequency	1
f_{max}	Maximum Available Frequency	1
g_m	transconductance	73
g_d	Degeneracy of the conduction band	27
γ	Growth speed ration between [100] and [113] orientations	22
$HFCVD$	Hot Filament CVD	16

$HPHT$	High Pressure High Temperature	5
$ISFET$	Ion Sensitive Field Effect Transistor	5
I_{DS}	MESFET current in the linear regime	58
I_{DSS}	MESFET current in the saturation regime	58
J	Current density	59
JFM	Johnson figure of merit	11
KFM	Keyes figure of merit	11
L/a	Aspect ration of channel length to channel depth	57
L_G	Gate Length	85
L_D	Debye length	33
L_T	Transfer Length	44
L_{eff}	Effective current path length	59
λ	Thermal conductivity	12
$MESFET$	Metal Semiconductor Field Effect Transistor	2
$MEMS$	Microelectromechanical systems	6
$MISFET$	Metal Intrinsic Semiconductor Field Effect Transistor	2
$MMIC$	Monolithic Microwave Integrated Circuits	22
$MOSFET$	Metal Oxide Field Effect Transistor	3
$MWPCVD$	Microwave Plasma CVD	16
m_{hh}	Mass of heavy holes	10
m_{lh}	Mass of light holes	11
m_{le}	Electron's longitudinal mass	11
m_{te}	Electron's transversal mass	11
μ_n	Mobility for Electrons	12
μ_p	Mobility for holes	12
N_D	Donor concentration	27
N_A	Acceptor concentration	26
n_s	Channel sheet charge density	27
Φ_B	Schottky barrier height	30
Φ_M	Metal Work Function	30
q	Elementary charge	33
$R.T.$	Room Temperature	12
R_{dl}	double layer Resistance	35
R_{SC}	Space charge Resistance	35
R_S	Sheet Resistance	44
RMS	Root mean square Roughness	34
ρ_C	specific contact resistance	44
$SCCM$	Standard Cubic Cm per Minute	41
$SIMS$	Secondary Ion Mass Spectroscopy	2
STM	Scanning Tunneling Microscopy	2
σ	standard deviation	37
TEM	Transmission Electron Microscopy	2
TMB	Trimethylborade	26

t_i	Intrinsic separation layer thickness between 2 delta layers	64
$UNCD$	Ultra Nano Crystalline Diamond	28
$VEvs.SCE$	Potential bw sample and Pt electrode Vs. reference electrode	36
v_{sat}	Carrier's saturation velocity	12
V_{th}	Threshold voltage	58
V_{DS}	Drain source voltage	58
V_{GS}	Gate Source Voltage	58
v_k	Knee voltage	58
W_d	Depletion width under the gate	58
W_G	Gate Width	85
Z_i	Imaginary part of impedance	66
Z	Impedance	66

Appendix E

Bibliography

[1] J. R. Chelikowsky and S. D. Louie, "First-principles linear combination of atomic orbitals method for the cohesive and structural properties of solids: Application to diamond," *Phys. Rev.*, vol. 28, p. 3470, 1984.

[2] K. Nassau, "Synthesis of bulk diamond: History and present status," in *Diamond films and coatings* (R. F. Davis, ed.), p. 31, Noyes Publications, 1993.

[3] Sumicrystal, "General catalogue - synthetic single crystal diamond," *Sumitomo Electric Industries*, 1989.

[4] K. Tsugawa, K. Kitatani, H. Noda, A. Hokazono, K. Hirose, M. Tajima, and H. Kawarada, "High performance diamond surface channel field effect transistors and their operation mechanism," *Diamond Relat. Mater.*, vol. 8, p. 927, 1999.

[5] R. S. Balmer, I. Friel, S. M. Woollard, C. J. H. Wort, G. A. Scarsbrook, S. E. Coe, H. El-Hajj, A. Kaiser, A. Denisenko, E. Kohn, and J. Isberg, "Unlocking diamond's potential as an electronic material," *Phil. Trans. R. Soc.*, vol. 366, pp. 251–265, 2008.

[6] A. Denisenko and E. Kohn, "Diamond power devices. concepts and limits," *Diamond Relat. Mater.*, vol. 14, p. 491, 2005.

[7] T. Rao, D. Tryk, K. Hashimoto, and A. Fujishima *J. Electrochem. Soc.*, vol. 146, p. 680, 1999.

[8] F. G. Celii and J. E. Butler, "Hydrogen atom detection in the filament assisted diamond deposition environment," *Appl. Phys. Lett.*, vol. 54, p. 1031, 1989.

[9] J. E. Field, "The properties of diamond," *Academic Press, London*, 1979.

[10] M. Yoder, "Diamond properties and applications," in *Diamond films and coatings* (R. F. Davis, ed.), p. 11, Noyes Publications, 1993.

[11] A. A. Altuhov, V. H. Lichtenstein, A. V. Shustrov, I. A. Mironenko, N. S. Chekalin, and S. N. Yakunin, "Natural diamonds of IIa type in spectrometry of heavy MeV ions," *Diamond Relat. Mater.*, vol. 13, p. 718, 2004.

[12] B. Marczewska, T. Nowak, P. Olko, W. Gajewski, Y. Palyanov, I. Kupriyanov, and M. P. Waligorski, "Synthetic diamonds as active detectors of ionizing radiation," *Diamond Relat. Mater.*, vol. 13, p. 918, 2004.

[13] E. Kohn, M. Adamschik, P. Schmid, S. Ertl, and A. Flöter, "Diamond electromechanical micro devices: technology and performance," *Diamond Relat. Mater.*, vol. 10, p. 1684, 2001.

[14] S. Ertl, M. Adamschik, P. Schmid, P. Gluche, A. Flöter, and E. Kohn, "Surface micromachined diamond microswitch," *Diamond Relat. Mater.*, vol. 9, p. 970, 2000.

[15] J. Kusterer, F. Hernandez, S. Haroon, P. Schmid, A. Munding, R. Müller, and E. Kohn, "Bi-stable micro actuator based on stress engineered nano-diamond," *Diamond Relat. Mater.*, vol. 15, p. 773, 2006.

[16] R. Muller, P. Schmid, A. Munding, R. Gronmaier, and E. Kohn, "Elements for surface microfluidics in diamond," *Diamond Relat. Mater.*, vol. 13, p. 780, 2004.

[17] R. Müller, R. Gronmaier, K. Janischowsky, J. Kusterer, and E. Kohn, "An all-diamond inkjet realized in sacrificial layer technology," *Diamond Relat. Mater.*, vol. 14, p. 504, 2005.

[18] M. Adamschik, M. Hinz, C. Maier, P. Schmid, H. Seliger, E. . Hofer, and E. Kohn, "Diamond micro system for bio-chemistry," *Diamond Relat. Mater.*, vol. 10, p. 722, 2001.

[19] R. Müller, M. Adamschik, D. Steidl, E. Kohn, S. Thamasett, S. Stiller, H. Hanke, and V. Hombach, "Application of CVD diamond for catheter ablation in the heart," *Diamond Relat. Mater.*, vol. 13, p. 1080, 2004.

[20] T. S. Huang, Y. Tzeng, Y. K. Liu, Y. C. Chen, K. R. Walker, R. Guntupalli, and C. Liu, "Immobilization of antibodies and bacterial binding on nanodiamond and carbon nanotubes for biosensor applications," *Diamond Relat. Mater.*, vol. 13, p. 1098, 2004.

[21] A. T. Collins, "Breakdown field and saturated carrier velocity in diamond," in *Properties and growth of diamond* (G. Davies, ed.), p. 228, INSPEC, 1994.

[22] J. Isberg, J. Hammersberg, E. Johansson, T. Wikström, D. J. Twitchen, A. Whitehead, S. Coe, and G. Scarsbrook, "High carrier mobility in single crystal plasma deposited diamond," *Science*, vol. 297, p. 1670, 2002.

[23] R. F. Davis, J. W. Palmour, and J. A. Edmond, "A review of the status of diamond and silicon carbide devices for high power, temperature, and frequency applications," *Int. El. Dev. Meeting*, p. 785, 1990.

[24] M. Adamschik, J. Kusterer, P. Schmid, K. Schad, D. Grobe, A. Flöter, and E. Kohn, "Diamond microwave micro relay," *Diamond Relat. Mater.*, vol. 11, p. 672, 2002.

[25] M. Kubovic, A. Aleksov, M. Schreck, T. Bauer, B. Stritzker, and E. Kohn, "Field effect transistor fabricated on hydrogen terminated diamond grown on $SrTiO_3$ substrate and iridium buffer layer," *Diamond Relat. Mater.*, vol. 12, p. 403, 2003.

[26] R. Berman, "Density, lattice constant and expansion coefficient of diamond," in *Properties and growth of diamond* (G. Davies, ed.), p. 23, INSPEC, 1994.

[27] A. K. Ramdas, "Vibrational band structure of diamond," in *Properties and growth of diamond* (G. Davies, ed.), p. 13, INSPEC, 1994.

[28] "Lexicon der chemie," Lexikographisches institut Meunchen, 1987.

[29] R. Sauer, N. Teofilov, and K. Thonke, "Exciton condensation in diamond," *Diamond Relat. Mater.*, vol. 13, p. 691, 2004.

[30] F. Nava, C. Canali, C. Jacoboni, and L. Reggiani, "Electron effective masses and lattice scattering in natural diamond," *Solid State Comm.*, vol. 33, p. 475, 1980.

[31] E. O. Johnson, "Physical limitations on freqeuncy and power parameters of transistors," *RCA Rev.*, vol. 26, p. 163, 1963.

[32] R. W. Keyes, "Figure of merit for high speed switches," *IEEE Proc.*, vol. 60, p. 225, 1972.

[33] F. P. Bundy et al., "Man made diamond," *Nature*, vol. 176, p. 51, 1995.

[34] S. T. Lee, Z. Lin, and X. Jiang, "CVD diamond films: nucleation and growth," *Mater. Scien. Engineer.*, vol. 25, p. 123, 1999.

[35] W. G. Eversole, "Synthesis of diamond," 1962.

[36] V. Spitsyn, L. L. Bouilov, and B. V. Deryagin, "Vapor growth of diamond on diamond and other surfaces," *Journal of Crystal Growth*, vol. 52, p. 219, 1981.

[37] B. V. Deryagin et al., "Synthesis of diamond on non diamond substrates," *Dokl. Akad. Nauk SSSR*, vol. 231, p. 333, 1976.

[38] P. W. May, "Diamond thin films: a 21^{st} century material," *Phil. Trans. R. Soc. Lond. A*, vol. 358, p. 473, 2000.

[39] K. Janishowsky, M. Stammler, and L. Ley, "High quality textured growth of oriented diamond thin films on Si (100) in a hot filament CVD system," *Diamond and Rel. Mat.*, vol. 8, p. 179, 1999.

[40] M. Kamo et al., "Diamond synthesis from gas phase microwave plasma," *J. Cryst. Growth*, vol. 62, p. 642, 1983.

[41] I. Tröster et al., "Electrochemical advanced oxidation process for water treatment using diachem electrodes," *Diamond and Rel. Mat.*, vol. 11, p. 640, 2002.

[42] M. Füner, C. Wild, and P. Koidl, "Novel microwave plasma reactor for diamond synthesis," *Appl. Phys. Lett.*, vol. 72, p. 1149, 1998.

[43] M. Kasu, M. Kubovic, A. Aleksov, N. Teofilov, Y. Taniyasu, R. Sauer, E. Kohn, T. Makimoto, and N. Kobayashi, "Influence of epitaxy on the surface conduction of diamond film," *Diamond Relat. Mater.*, vol. 13, p. 226, 2004.

[44] T. R. Anthony, "Methastable synthesis of diamond," *Vacuum*, vol. 41, p. 1356, 1990.

[45] S. J. Harris, A. M. Weiner, and T. A. Perry, "Measurement of stable species present during filament assisted diamond growth," *Appl. Phys. Lett.*, vol. 53, p. 1605, 1988.

[46] P. K. Bachmann, "Towards a general concept of diamond chemical vapor deposition," *Diamond and Rel. Mat.*, vol. 1, p. 1, 1991.

[47] V. Ralchenko et al., "Quality of diamond wafers grown by microwave plasma CVD: Effect of gas flow rate," *Diamond and Rel. Mat.*, vol. 8, p. 189, 1999.

[48] M. Kunze, "Optimierung pulsdotierter diamantschichten," *Diplomarbeit, Uni-Ulm*, Sept. 1997.

[49] H. Okushi, "High quality homoepitaxial CVD diamond for electronic devices," *Diamond and related materials*, vol. 10, p. 281, 2001.

[50] S. T. Lee and Y. Lifshitz, "The road to diamond wafers," *Nature*, vol. 424, p. 500, 2003.

[51] M. Schreck, F. Hörmann, H. Roll, J. K. Lindner, and B. Stritzker, "Diamond nucleation on iridium buffer layers and subsequent textured growth: A route for the realization of single-crystal diamond films," *Appl. Phys. Lett.*, vol. 78, p. 192, 2001.

[52] M. Schreck, A. Schury, F. Hörmann, H. Roll, and B. Stritzker, "Mosaicity reduction during growth of heteroepitaxial diamond films on iridium buffer layers: Experimental results and numerical simulations," *J. Appl. Phys.*, vol. 91, p. 676, 2002.

[53] S. Gsell, M. Schreck, G. Benstetter, E. Lodermeier, and B. Stritzker, "Combined AFM - SEM study of the diamond nucleation layer on Ir (001)," *Diamond Relat. Mater.*, vol. 16, p. 665, 2007.

[54] A. Sawabe, H. Fukuda, T. Suzuki, Y. Ikuhara, and T. Suzuki, "Interface between CVD diamond and iridium films," *Surf. Science*, vol. 467, p. L845, 2000.

[55] M. Tachiki, T. Fujisakia, N. Taniyamab, M. Kudob, and H. Kawarada, "Heteroepitaxial diamond thin film growth on Ir(001) / MgO(001) substrate by antenna-edge plasma assisted chemical vapor deposition," *J. Crystal Growth*, vol. 237-239, p. 1277, 2002.

[56] C. Bednarski, Z. Dai, A. P. Li, and B. Golding, "Studies of heteroepitaxial growth of diamond," *Diamond Relat. Mater.*, vol. 12, p. 241, 2003.

[57] K. Kusakabe, A. Sobana, K. I. Sotowa, T. Imato, and T. Tsubota, "Electrical properties of boron-doped diamond films synthesized by MPCVD on an iridium substrate," *Diamond Relat. Mater.*, vol. 12, p. 1396, 2003.

[58] C. H. Lee, J. Qi, S. T. Lee, and L. S. Hung, "Epitaxial diamond on a Si / CaF / Ir substrate," *Diamond Relat. Mater.*, vol. 12, p. 1335, 2003.

[59] J. F. Custers, "Unusual photoluminescence of a diamond," *Physica*, vol. 18, p. 489, 1952.

[60] M. N. Gamo et al., "Sulfur doped homoepitaxial (001) diamond with $n-$type semiconductive properties," *Diamond and Rel. Mat.*, vol. 9, p. 941, 2000.

[61] R. Job et al., "Electrical properties of lithium implanted layers on synthetic diamond," *Diamond and Rel. Mat.*, vol. 5, p. 757, 1996.

[62] R. Kalish, "Doping diamond by ion-implantation," in *Thin film diamond I* (C. E. Nebel and J. Ristein, eds.), vol. 76, p. 145, Elsevier, 2003.

[63] J. F. Prins, "Bipolar transistor action in ion implanted diamond," *Appl. Phys. Lett.*, vol. 41, p. 950, 1982.

[64] R. Kalish et al., "Nitrogen doping of diamond by ion implantation," *Diamond and Rel. Mat.*, vol. 6, p. 516, 1997.

[65] A. Ogasawara et al., "Optical and electrical investigation of boron doped homoepitaxial diamond," *Diamond and Rel. Mat.*, vol. 6, p. 835, 1997.

[66] E. Oesterschulze et al., "Diamond cantilevers with integrated tip for nanomachining," *Diamond and Rel. Mat.*, vol. 11, p. 667, 2002.

[67] T. H. Borst and O. Weis, "Electrical characterization of homoepitaxial diamond films doped with B, P, Li and Na during crystal growth," *Diamond Relat. Mater.*, vol. 4, p. 948, 1995.

[68] M. Kunze, A. Vescan, G. Dollinger, A. Bergmaier, and E. Kohn, "δ-doping in diamond," *Carbon*, vol. 37, p. 787, 1999.

[69] T. Saito et al., "Semiconductive properties of homoepitaxial diamond films doped using trimethylboron," *Diamond 1998 Conference*, 1998.

[70] R. Kalish, "The search for donors in diamond," *Diamond Relat. Mater.*, vol. 10, p. 1749, 2001.

[71] D. Saada, J. Adler, and R. Kalish, "Sulfur: A potential donor in diamond," *Appl. Phys. Lett.*, vol. 77, p. 878, 2000.

[72] K. Nakazawa, M. Tachiki, H. Kawarada, A. Kawamura, K. Horiuchi, and T. Ishikura, "Cathodoluminescence and hall-effect measurements in sulfur doped chemical vapor deposited diamond," *Appl. Phys. Lett.*, vol. 82, p. 2074, 2003.

[73] S. Bhattacharyya, O. Auciello, J. Birrell, J. A. Carlisle, L. A. Curtiss, A. N. Goyette, D. M. Gruen, A. R. Krauss, J. Schlueter, A. Sumant, and P. Zapol, "Synthesis and characterization of highly conducting nitrogen doped ultrananocrystalline diamond films," *Appl. Phys. Lett.*, vol. 79, p. 1441, 2001.

[74] J. A. Carlisle and O. Auciello, "Ultrananocrystalline diamond: Properties and applications in biomedical devices," *Electrochem. Soc. Interface*, p. 28, 2003.

[75] T. Zimmermann, M. Kubovic, A. Denisenko, K. Janischowsky, O. A. Williams, D. M. Gruen, and E. Kohn, "Ultra nano crystalline / single crystal diamond heterostructure diode," *Diamond Relat. Mater.*, vol. 14, p. 416, 2005.

[76] R. Samlenski et al., "Characterisation and lattice location of nitrogen and boron in homoepitaxial CVD diamond," *Diamond and Rel. Mat.*, vol. 5, p. 947, 1996.

[77] A. T. Collins, "Diamond electronic devices: a critical appraisal," *Semiconductor Science and Technology*, vol. 4, p. 605, 1989.

[78] A. Aleksov, A. Denisenko, and E. Kohn, "First epitaxial pnp bipolar transistor on diamond with deep nitrogen donor," *Electronics Lett.*, vol. 35, p. 1777, 1999.

[79] V. Baranauskas, B. B. Li, A. Peterlevitz, M. C. Tosin, and S. F. Durrant, "Nitrogen doped diamond films," *J. Appl. Phys.*, vol. 85, p. 7455, 1999.

[80] C. F. Shih, K. S. Liu, and I. N. Lin, "Effect of nitrogen doping on the electron field emission properties of chemical vapor deposited diamond films," *Diamond Relat. Mater.*, vol. 9, p. 1591, 2000.

[81] N. Jiang, A. Hatta, and T. Ito, "Nitrogen doping effects on electrical properties of diamond films," *Jpn. J. Appl. Phys.*, vol. 37, p. L1175, 1998.

[82] J. Ristein, M. Riedel, F. Maier, B. F. Mantel, M. Stammler, and L. Ley, "Surface conductivity of diamond as a function of nitrogen doping," *Phys. Stat. Sol. (a)*, vol. 186, p. 249, 2001.

[83] P. Zapol, M. Sternberg, L. A. Curtiss, T. Frauenheim, and D. M. Gruen, "Tight binding molecular dynamics simulation of impurities in ultrananocrystalline diamond grain boundaries," *Phys. Rev. B*, vol. 65, p. 045403, 2001.

[84] J. Birrell, J. A. Carlisle, O. Auciello, D. M. Gruen, and J. M. Gibson, "Morphology and electronic structure in nitrogen doped ultrananocrystalline diamond," *J. Appl. Phys.*, vol. 81, p. 2235, 2002.

[85] V. I. Polyakov, A. I. Rukovishnikov, N. M. Rossukanyi, V. G. Pereverzev, S. M. Pimenov, J. A. Carlisle, D. M. Gruen, and E. N. Loubnin, "Charge based deep level transient spectroscopy of undoped and nitrogen doped ultrananocrystalline diamond films," *Diamond Relat. Mater.*, vol. 12, p. 1776, 2003.

[86] E. Kohn, A. Denisenko, M. Kubovic, T. Zimmermann, O. A. Williams, and D. M. Gruen, "A new diamond based heterostructure diode," *Semicond. Sci. Technol.*, vol. 21, p. L32, 2006.

[87] H. Kato, S. Yamasaki, and H. Okushi, "n-type conductivity of phosphorus-doped homoepitaxial single crystal diamond on (001) substrate," *Diamond Relat. Mater.*, vol. 14, p. 2007, 2005.

[88] S. Koizumi, M. Kamo, Y. Sato, H. Ozaki, and T. Inuzuka, "Growth and characterization of phosphorous doped 111 homoepitaxial diamond thin films," *Appl. Phys. Lett.*, vol. 71, p. 1065, 1997.

[89] S. Koizumi, "Growth and characterization of phosphorus doped n-type diamond thin films," *Phys. Stat. Sol. (a)*, vol. 172, p. 71, 1999.

[90] T. Teraji, S. Koizumi, and H. Kanda, "Ohmic contacts for phosphorus-doped n-type diamond," *Phys. Stat. Sol. (a)*, vol. 181, p. 129, 2000.

[91] H. Kato, H. Watanabe, S. Yamasaki, and H. Okushi, "N-type doping on (001)-oriented diamond," *Diamond Relat. Mater.*, vol. 15, p. 548, 2006.

[92] H. Kawarada, "Hydrogen terminated surfaces and interfaces," *Surf. Sci. Repts*, vol. 26, p. 205, 1996.

[93] K. Hayashi, S. Yamanaka, H. Watanabe, T. Sekiguchi, H. Okushi, and K. Kajimura, "Investigation of the effect of hydrogen on electrical and optical properties in chemical vapor deposited on homoepitaxial diamond films," *J. Appl. Phys.*, vol. 81, p. 744, 1997.

[94] C. E. Nebel et al., "Low temperature properties of the $p-$type surface conductivity of diamond," *Diamond and Rel. Mat.*, vol. 11, p. 351, 2002.

[95] J. Ristein et al., "Diamond surface conductivity experiments and photoelectron spectroscopy," *Diamond and Rel. Mat.*, vol. 10, p. 416, 2001.

[96] Y. Yun, H. Tanaka, A. Itoh, T. Maki, and T. Kobayashi, "Electrical properties of Al/(Ba_xCa_{1-x})F_2/i-diamond metal-insulator-semiconductor structures," *Jpn. J. Appl. Phys.*, vol. 38, p. 2626, 1999.

[97] M. Aoki and H. Kawarada, "Electric properties of metal/diamond interfaces utilizing hydrogen-terminated surfaces of homoepitaxial diamonds," *Jpn. J. Appl. Phys.*, vol. 33, p. L708, 1994.

[98] S. M. Sze, "Physics of semiconductor devices," pp. (John Wiley & Sons, 1981).

[99] A. Hokazono, T. Ishikura, K. Nakamura, S. Yamashita, and H. Kawarada, "Enhancement / depletion MESFETs of diamond and their logic circuits," *Diamond Relat. Mater.*, vol. 6, p. 339, 1997.

[100] M. Kubovic, M. Kasu, I. Kallfass, M. Neuburger, A. Aleksov, G. Koley, M. Spencer, and E. Kohn, "Microwave performance evaluation of diamond surface channel FETs," *Diamond. Relat. Mater.*, vol. 13, p. 802, 2004.

[101] M. Itoh and H. Kawarada, "Fabrication and characterization of metal semiconductor field effect transistor utilizing diamond surface conductive layer," *Jpn. J. Appl. Phys.*, vol. 34, p. 4677, 1995.

[102] K. Tsugawa, A. Hokazono, H. Noda, K. Kitatani, K. Morita, and H. Kawarada, "MESFETs and MOSFETs on hydrogen-terminated diamond surfaces," *Mater. Science Forum*, vol. 264-268, p. 977, 1998.

[103] M. Kubovic, A. Aleksov, A. Denisenko, and E. Kohn, "Advances in diamond surface channel FET technology with focus on large signal properties," *IEEE Lester Eastman Conference (Newark, DE),*, p. 90, August 2002.

[104] A. Aleksov, M. Kubovic, M. Kasu, P. Schmid, D. Grobe, S. Ertl, M. Schreck, B. Stritzker, and E. Kohn, "Diamond based electronics for RF applications," *Diamond. Relat. Mater.*, vol. 13, p. 233, 2004.

[105] M. Kasu, M. Kubovic, A. Aleksov, I. Kallfass, H. Schumacher, E. Kohn, and N. Kobayashi, "Microwave performance of diamond MESFET," *OYO BUTURI*, vol. 73, p. 363, 2004.

[106] M. Kasu, K. Ueda, H. Ye, Y. Yamauchi, S. Sasaki, and T. Makimoto, "High RF output power for H-terminated diamond FETs," *Diamond Relat. Mater.*, vol. 15, p. 783, 2006.

[107] K. Kitatani, H. Umezawa, K. Tsugawa, K. Ueyama, T. Ishikura, S. Yamashita, and H. Kawarada, "MOSFETs on polished surfaces of polycrystalline diamond," *Diamond Relat. Mater.*, vol. 8, p. 1831, 1999.

[108] A. Hokazono, K. Tsugawa, H. Umezana, K. Kitatani, and H. Kawarada, "Surface p-channel metal-oxide-semiconductor field effect transistors fabricated on hydrogen terminated (001) surfaces of diamond," *Solid State Electron.*, vol. 43, p. 1465, 1999.

[109] H. Ishizaka, M. Tachiki, K. Song, U. H, and H. Kawarada, "Cryogenic operation of surface channel diamond field effect transistors," *Diamond Relat. Mater.*, vol. 12, p. 1800, 2003.

[110] K. Harama, S. Miyamoto, H. Matsudaira, H. Umezawa, and H. Kawarada, "Fabrication of t -shaped gate diamond metal-insulator-semiconductor field-effect transistors," *Jpn. J. Appl. Phys.*, vol. 45, p. 5681, 2006.

[111] R. Müller, A. Denisenko, M. Adamschik, and E. Kohn, "Effect of surface quality on the ion sensitivity of H-terminated surface channel devices on diamond," *Diamond Relat. Mater.*, vol. 11, p. 651, 2002.

[112] H. Kawarada et al., "Electrolyte solution gate FETs using diamond surface for biocompatible ion sensors," *Phys. Stat. Sol. (a)*, vol. 185, p. 79, 2001.

[113] K. Song, M. Degawa, Y. Nakamura, H. Kanazawa, H. Umezawa, and H. Kawarada, "Surface modified diamond field effect transistors for enzyme immobilized biosensors," *Jpn. J. Appl. Phys.*, vol. 43, p. L817, 2004.

[114] C. E. Nebel, C. Sauerer, F. Ertl, M. Stutzmann, C. Graef, P. Bergonzo, O. A. Williams, and R. Jackman, "Hydrogen-induced transport properties of holes in diamond surface layers," *Appl. Phys. Lett.*, vol. 79, p. 4541, 2001.

[115] F. Maier, M. Riedel, B. Mantel, J. Ristein, and L. Ley, "Origin of surface conductivity in diamond," *Phys. Rev. Lett.*, vol. 85, p. 3472, 2000.

[116] D. Takeuchi, S.Yamanaka, and H. Okushi, "Schottky junction properties of the high conductivity layer of diamond," *Diamond Relat. Mater.*, vol. 11, p. 355, 2002.

[117] A. T. Collins, "$p-$type conductivity of diamond," in *Properties and growth of diamond* (G. Davies, ed.), p. 273, INSPEC, 1994.

[118] A. Vescan, "Herstellung und charakterisierung elektronischer bauelemente auf bordotierten homoepitaktischen diamantschichten," University of Ulm, 1998.

[119] S. Yamanaka, D. Takeuchi, H. Watanabe, H. Okushi, and K. Kajimura, "Low compensated boron doped homoepitaxial diamond films using trimethylboron," *Phys. Stat. Sol. (a)*, vol. 174, p. 59, 1999.

[120] L. Pan and D. Kania, "Diamond: Electronic properties and applications," p. 472, Kluwer Acad. Publ., Boston, 1995.

[121] A. Collins p. 257, Material Sci. and Enginner, 1992.

[122] H. Shiomi, Y. Nishibayashi, N. Toda, and S. Shikata *IEEE Electron Dev. Lett.*, vol. 16, p. 36, 1995.

[123] K. H. Shim and J. T. Lim *Electronic Letters*, vol. 32, p. 1419, 1996.

[124] Y. Ando, T. Ariki, and T. Kobayashi *Jpn. J. Appl. Phys.*, vol. 34, p. 3987, 1995.

[125] A. Aleksov, A. Vescan, M. Kunze, P. Gluche, W. Ebert, E. Kohn, A. Bergmaier, and G. Dollinger, "Diamond junction FETs based on δ-doped channels," *Diamond Relat. Mater.*, vol. 8, p. 941, 1999.

[126] T. Kobayashi, T. Ariki, M. Iwabuchi, T. Maki, S. Shikama, and S. Suzuki, "Analytical studies on multiple delta doping in diamond thin films for efficient hole excitation and conductivity enhancement," *J. Appl. Phys.*, vol. 76, p. 1977, 1994.

[127] M. Schwitters, M. P. Dixon, A. Tajani, D. J. Twitchen, S. E. Coe, H. El-Hajj, M. Kubovic, M. Neuburger, A. Kaiser, and E. Kohn, "Diamond MESFETs: Synthesis and integration," *European Radar Conference (Paris, France),*, p. 17, October 2005.

[128] G. Dollinger, A. Bergmaier, L. Goergens, P. Neumaier, W. Vandervorst, and S. Jakschik *Nucl. Instr. And Meth.*, vol. 219, p. 333, 2004.

[129] J. van Lagemaat, D. Vanmaekelbergh, and J. Kelly *J. Electroanal. Chem.*, vol. 475, p. 139, 1999.

[130] Y. Pleskov, "The electrochemistry of diamond," in *Advances in Electrochemical Science and Engineering* (R. Alkire and D. Kolb, eds.), p. 366, J. Wiley, 1999.

[131] J. Wilson et al. in *J. Electron Spectroscopy*, vol. 121, p. 183, 2001.

[132] D. Becker and K. Juittinger *J. Appl. Electrochem*, vol. 33, p. 959, 2003.

[133] J. Angus, H. Martin, U. Landau, Y. Evstefeeva, B. Miller, and N. Vinokur *New Diamond Frontier Carbon Technol.*, vol. 9, p. 175, 1999.

[134] A. Denisenko, G. Jamornmarn, H. El-Hajj, and E. Kohn, "ph sensor on o-terminated diamond using boron-doped channel," *Diamond Relat. Mater.*, vol. 16, p. 905, 2007.

[135] C. Nebel and J. Ristein, "Thin film diamond," in *Semiconductors and Semimetals Series* (R. Willardson and R. Weber, eds.), vol. 77, p. 396, Elsevier Acad. Press, 2004.

[136] A. Denisenko, "Private conversation,"

[137] A. Denisenko et al., "Riva del garda (italy)," *Diamond 2004*, vol. paper 10.1, 2004.

[138] R. Trew, J. Yan, and P. Mock *Proc IEEE*, vol. 79, p. 598, 1991.

[139] A. Aleksov, M. Kubovic, N. Kaeb, U. Spitzberg, A. Bergmaier, G. Dollinger, T. Bauer, M. Schreck, B. Stritzker, and E. Kohn, "Diamond field effect transistors, concepts and challenges," *Diamond Relat. Mater.*, vol. 12, p. 391, 2003.

[140] H. Taniuchi, H. Umezawa, T. Arima, M. Tachiki, and H.Kawarada *IEEE Electon Dev. Lett.*, vol. 22, p. 390, 2001.

[141] M. Kasu, K. Ueda, H. Ye, Y. Yamauchi, S. Sasaki, and T. Makimoto, "$2\,w/mm$ output power density at $1\,ghz$ for diamond FETs," *Electron. Lett.*, vol. 41, p. 1249, 2005.

[142] A. Fujushima, Y. Einaga, T. Rao, and D. Tryk, "Diamond electrochemistry," p. 586, Elsevier Publ., 2005.

[143] L. Thomson, F. Law, N. Rushton, and J. Franks *Biomaterials*, vol. 12, p. 37, 1991.

[144] H. Kawarada, Y. Araki, T. Sakai, T. Ogawa, and H. Umezawa, "Electrolyte solution gate FETs using diamond surface for biocompatible ion sensors," *Phys. Stat. Sol. (a)*, vol. 185, p. 79, 2001.

[145] W. Yang and R. Hamers *Appl. Phys. Lett.*, vol. 85, p. 3626, 2004.

[146] B. Rezek, H. Watanabe, D. Shin, T. Yamamoto, and C. Nebel *Diam. Rel. Mat.*, vol. 15, p. 1007, 2006.

[147] A. Denisenko, A. Aleksov, and E. Kohn, "ph sensing by surface doped diamond and effect of the diamond surface termination," *Diamond Relat. Mater.*, vol. 10, p. 667, 2001.

[148] J. Garrido, A. Haertl, S. Kuch, M. Stutzmann, O. Williams, and R. Jackmann *Appl. Phys. Lett.*, vol. 86, p. 73504, 2005.

[149] B. Nichols, J. Butler, J. Russels, and R. Hamers *J. Phys. Chem.*, vol. 109, p. 20938, 2005.

[150] T. Kondo, K. Honda, D. Tryk, and A. Fujishima *J. Electrochem. Soc.*, vol. 152, p. E18, 2005.

[151] R. Müller, A. Denisenko, and E. Kohn, "Effect of surface quality on ion sensitivity of H-terminated diamond," *Diamond Relat. Mater.*, vol. 12, p. 554, 2003.

[152] J. Iniesta, P. A. Michaud, M. Panizza, G. Cerisola, A. Aldaz, and C. Comninellis *Electrochim. Act.*, vol. 46, p. 3573, 2001.

[153] R. Thomas, R. Rudder, and R. Markunas *J. Vac. Sci. Technol.*, vol. 10, p. 2451, 1992.

[154] K. Janischowsky, W. Ebert, and E. Kohn, "Bias enhanced nucleation of diamond on silicon (100) in a HFCVD system," *Diamond and Rel. Mat.*, vol. 12, p. 336, 2003.